Title

Quantitative Prostate Diffusion MRI and Multi-Dimensional Diffusion-Relaxation Correlation MRI for Characterization of Prostate Cancer

Author

Zhang, Zhaohuan

Publication Date

2023

Peer reviewed|Thesis/dissertation

UNIVERSITY OF CALIFORNIA

Los Angeles

Quantitative Prostate Diffusion MRI and Multi-Dimensional Diffusion-Relaxation Correlation MRI for Characterization of Prostate Cancer

A dissertation submitted in partial satisfaction of the

requirements for the degree Doctor of Philosophy

in Bioengineering

by

Zhaohuan Zhang

2023

ABSTRACT OF THE DISSERTATION

Quantitative Prostate Diffusion MRI and Multi-Dimensional Diffusion-Relaxation Correlation MRI for Characterization of Prostate Cancer

by

Zhaohuan Zhang

Doctor of Philosophy in Bioengineering

University of California, Los Angeles, 2023

Professor Holden H. Wu, Chair

Prostate Cancer (PCa) remains the second most common cause of cancer-related death in men in the U.S. Multi-parametric (mp) MRI is playing an increasingly important role for the localization, detection, and risk stratification of PCa. However, prostate mp-MRI still misses PCa in up to 45% of men and faces challenges in distinguishing clinically significant PCa from indolent PCa. Therefore, MRI technology must be improved to enhance diagnostic performance for PCa.

This thesis aimed to improve prostate MRI by addressing two challenges. First, the diffusion-weighted imaging (DWI) component of mp-MRI often suffers from artifacts such as distortion and low signal-to-noise ratio (SNR), which can lead to low diagnostic image quality. Second, prostate microstructure features are key determinants for histopathological assessment of cancer aggressiveness; however, current MRI techniques have limitations in capturing this information.

To address the first challenge, in Aim 1, we translated and evaluated an eddy current-nulled convex optimized diffusion encoding (ENCODE) based prostate DWI technique that achieves short echo time (TE) to maintain SNR while reducing prostate geometric distortion from eddy currents and susceptibility effects. Further, in Aim 2, we developed a combined TE-minimized ENCODE diffusion encoding acquisition with a random matrix theory-based denoising reconstruction technique to improve the SNR and robustness of high-resolution (in-plane: 1.0x1.0 mm^2) prostate DWI and apparent diffusion coefficient mapping.

To address the second challenge, in Aim 3, we performed a first proof-of-concept ex vivo evaluation and validation of the diffusion-relaxation correlation spectrum imaging (DR-CSI) technique at 3T for quantifying microscopic tissue compartments (epithelium, stroma, and lumen) in PCa using whole-mount digital histopathology as the reference standard. Further, in Aim 4, we explored and evaluated sequential backward selection analysis for the acceleration of DR-CSI through subsampling of the diffusion-relaxation contrast encoding space while maintaining the accuracy of prostate microstructure mapping in PCa.

The dissertation of Zhaohuan Zhang is approved.

Steven S. Raman

Benjamin M. Ellingson

Corey W. Arnold

Kyung-Hyun Sung

Holden H. Wu, Committee Chair

University of California, Los Angeles

2023

For dad and mom

TABLE OF CONTENTS

LIST OF ABBREVIATIONS

2D/3D - two/three dimensional

ANOVA - Analysis Of Variance

CoV - Coefficient of Variation

DWI - Diffusion Weighted Imaging

DR-CSI - Diffusion-Relaxation Correlation Spectrum Imaging

EPI - Echo-Planar Imaging

FOV - Field Of View

GRAPPA - GeneRalized Autocalibrating Partial Parallel Acquisition

mm - millimeter

MRI - Magnetic Resonance Imaging

ms - millisecond

MSE - Mean Squared Error

MP-PCA - Marchenko-Pastur Distribution Principal Component Analysis

PE - Phase Encoding

PI - Parallel Imaging

ROI - Region Of Interest

RMT - Random Matrix Theory

s - second

SD - Standard Deviation

SNR - Signal-to-Noise Ratio

SBS – Sequential Backward Selection

SPAIR – Spectral Attenuated Inversion Recovery

T - Tesla

T2w - T_2-weighted

TE - Echo Time

TPS – Thin Plate Spline

TR - Repetition Time

TSE - Turbo Spin Echo

LIST OF FIGURES

LIST OF TABLES

ACKNOLEDGEMENTS

I would like to first express my gratitude to my Ph.D. advisor Dr Holden H. Wu for providing mentorship, guidance, feedback, and encouragement throughout my PhD. journey. I am especially lucky to be able to observe and learn from Dr Holden H. Wu directly about the process of scientific reasoning, problem solving and having perseverance to push through failure. The scientific spirit that I gained from PhD training is one of the most valuable treasures of my life. I would also like to thank all members of my committee: Dr Kyung-Hyun Sung, Dr Steven Raman, Dr Benjamin Ellingson and Dr Corey Arnold, who provided suggestions and insightful criticism to improve my works.

I would like to especially thank Fadil Ali, Heather Wilbur, Haozhou Zhu, Shu-Fu Shih, Haoxin (Elvis) Zhang, Yuanqi Liao, Xinzhou Li, Qing Dai, Chang Gao, Haoxin Zheng, Zixuan Zhao, Andres Saucedo, Nyasha Maforo, Elif Aygun, Tyler E. Cork, Da Wang, Xinran Zhong, Yongqiang Tan, Siyun Liu and Leo Montale etc. for the friendships and companionships throughout my graduate school career.

I also would like to thank my mentors including: Alan Priester, Eric Aliotta, Kevin Moulin, Da Wang, Zhe Wang and Suba Srinivasan, and my collaborators including: Sohrab Afshari Mirak, Sepideh Shakeri, Niloofar Sheshebor, Nashla Barroso, Tammy L Foore, Reevia J Mccollins, Angela L Clark etc. for assisting and landing me helps over my scientific adventurers. I would also like to thank the peer scientist I be-friended with during international conference: Gregory Lemberskiy for providing valuable insights into Prostate MRI and science in general.

Lastly, I would like to especially thank Dr Daniel B. Ennis for guiding me into the wonderland of MRI science, I also want to thank Dr Michael McNitt-Gray, Dr Bernie H.K. Huang and Dr Jianguo Zhang for guiding me into the beautiful world of Medical Imaging and Medical Physics.

Chapter 3 is a version of: Zhang Z, Moulin KF, Aliotta E, Shakeri S, Afshari Mirak S, Hosseiny M, Raman S, Ennis DB, Wu HH. Prostate Diffusion MRI with Minimal Echo Time using Eddy Current Nulled Convex Optimized Diffusion Encoding. ***J Magn Reson Imaging*** 2020; 51(5):1526-1539. This work is reproduced with minor changes.

Chapter 4 is a version of: Zhang Z, Shih S-F, Raman S, Sung K, Wu HH. High-Resolution Prostate Diffusion MRI Using Eddy Current-Nulled Convex Optimized Diffusion Encoding with Random Matrix Theory-Based Denoising. ***Magn Reson Mater Phy*** 2023. (*Under Review*). This work is reproduced with minor changes.

Chapter 5 is a version of: Zhang Z, Wu HH, Priester A, Magyar C, Afshari Mirak S, Shakeri S, Mohammadian Bajgiran A, Hosseiny M, Azadikhah A, Sung K, Reiter RE, Sisk AE, Raman S, Enzmann DR. Prostate Microstructure in Prostate Cancer using 3T MRI with Diffusion-Relaxation Correlation Spectrum Imaging: Validation with Whole-Mount Digital Histopathology. ***Radiology*** 2020; 296(2):348-355. This work is reproduced with minor changes.

Chapter 6 is a version of: Zhang Z, Afshari Mirak S, Mohammadian Bajgiran A, Hosseiny M, Azadikhah A, Priester A, Sung K, Reiter RE, Sisk AE, Raman S, Enzmann DR, Wu HH. Sequential Backward Selection Analysis to Accelerate Prostate Microstructure Mapping Using Diffusion-Relaxation Correlation Spectrum Imaging. (*In Preparation for Submission*)

VITA

Education:

- Bioengineering, University of California Los Angeles, Los Angeles, CA, USA, 2016 – 2023
- B.S., Physics and Astronomy, Shanghai Jiao Tong University, Shanghai, PRC, 2012 – 2016

Distinctions:

- MR of Cancer Study Group Top 5 Trainee Research Prize, *International Society for Magnetic Resonance in Medicine (ISMRM)*, 2021
- Featured research article in *Radiology* with Editorial, 2020
- Summa Cum Laude Award, *ISMRM*, 2020
- Magna Cum Laude Awards (x2), *ISMRM*, 2021
- Johnson Comprehensive Cancer Center Fellowship Award, *UCLA*, 2021
- Graduate Division Fellowship, *UCLA*, 2016-2017

Journal Publications and Manuscripts:

1. **Zhang Z**, Wu HH, Priester A, Magyar C, Afshari Mirak S, Shakeri S, Mohammadian Bajgiran A, Hosseiny M, Azadikhah A, Sung K, Reiter RE, Sisk AE, Raman S, Enzmann DR. Prostate Microstructure in Prostate Cancer using 3T MRI with Diffusion-Relaxation Correlation Spectrum Imaging: Validation with Whole-Mount Digital Histopathology. ***Radiology*** 2020; 296(2):348-355.
2. **Zhang Z**, Moulin KF, Aliotta E, Shakeri S, Afshari Mirak S, Hosseiny M, Raman S, Ennis DB, Wu HH. Prostate Diffusion MRI with Minimal Echo Time using Eddy Current Nulled Convex Optimized Diffusion Encoding. ***J Magn Reson Imaging*** 2020; 51(5):1526-1539.

3. **Zhang Z**, Shih Shu-Fu, Raman S, Sung K, Wu HH. High-Resolution Prostate Diffusion MRI Using Eddy Current Nulled Convex Optimized Diffusion Encoding with Random Matrix Theory-based Denoising. ***Magn Reson Mater Phy*** 2023. (*Under Review*)
4. **Zhang Z**, Afshari Mirak S, Mohammadian Bajgiran A, Hosseiny M, Azadikhah A, Priester A, Sung K, Reiter RE, Sisk AE, Raman S, Enzmann DR, Wu HH. Sequential Backward Selection Analysis to Accelerate Prostate Microstructure Mapping Using Diffusion-Relaxation Correlation Spectrum Imaging. *In preparation; to be submitted to* ***J Magn Reson Imaging***.
5. Shih S-F*, **Zhang Z***, Tasdelen B, Yagiz E, Zhong X, Cui S, Nayak KS, Wu HH. K-space Low Rankness Enables Addictive Noise Removal Using Random Matrix Theory (KLEANRR): An application to Fat and R2* Quantification at 0.55T. (*co-first authors) *In preparation; to be submitted to* ***Magn Reson Med***.
6. Wu HH, Priester A, Khoshnoodi P, **Zhang Z**, Shakeri S, Afshari Mirak S, Asvadi NH, Ahuja P, Sung K, Natarajan S, Sisk A, Reiter R, Raman S, Enzmann D. A System Using Patient-Specific 3D-Printed Molds to Spatially Align In Vivo MRI with Ex Vivo MRI and Whole-Mount Histopathology for Prostate Cancer Research. ***J Magn Reson Imaging*** 2019; 49(1):270-279.
7. Priester A, Wu H, Khoshnoodi P, Schneider D, **Zhang Z**, Asvadi N, Sisk A, Raman S, Reiter R, Grundfest W, Marks LS, Natarajan S. Registration Accuracy of Patient-Specific 3D Printed Prostate Molds for Correlating Pathology with Magnetic Resonance Imaging**.** ***IEEE Transactions on Biomedical Engineering*** 2019; 66(1):14- 22.
8. Aliotta E, Moulin K, **Zhang Z**, Ennis DB. Simultaneous Measurement of T2 and Apparent Diffusion Coefficient (T2+ADC) in the Heart with Motion-Compensated Spin Echo Diffusion-Weighted Imaging. ***Magn Reson Med*** 2017; 79: 654-662.

Chapter 1 **Introduction**

1.1 **Thesis Motivation**

Prostate cancer (PCa) is the most prevalent noncutaneous cancer diagnosed in men and the second leading cause of cancer-related death in men in the United States [1]. Multiparametric magnetic resonance imaging (mp-MRI) of the prostate, including T_2-weighted (T2W) MRI, diffusion-weighted MRI (DWI) and apparent diffusion coefficient (ADC) maps, and dynamic contrast-enhanced MRI (DCE-MRI), is an important tool for the detection and characterization of PCa [2]. DWI is an especially important component of prostate mp-MRI that has high sensitivity for the detection and localization of PCa [3]. The DWI-derived ADC maps were shown to correlate with aggressiveness of PCa [4] and can predict histological tumor volumes [3].

The standard encoding schemes for prostate DWI are monopolar spin echo (MONO) and twice-refocused bipolar spin echo (BIPOLAR) [5,6]. MONO has a relatively short echo time (TE), but is susceptible to eddy current-induced directionally dependent distortion artifacts. BIPOLAR uses a modified gradient design and a second refocusing pulse to mitigate eddy current fields that are produced by each gradient lobe at the end of diffusion encoding, but at a cost of substantially increased TE (and lower signal-to-noise ratio [SNR]) compared to MONO [6]. In general, both a short TE and reduced eddy current-induced distortion artifacts are desired to maintain sufficient SNR (or improve acquisition speed) and minimize overall image distortion in prostate DWI [7,8]. However, current encoding schemes (MONO or BIPOLAR) cannot achieve these two desired features at the same time. Therefore, optimization of the diffusion encoding scheme to meet both needs is desired for prostate DWI.

Furthermore, improving the spatial resolution of prostate DWI may improve its performance for PCa diagnosis, with finer depiction of prostate tissues compared to standard clinical prostate DWI protocols, which typically use single-shot echo planar imaging (EPI) readouts and have in-plane resolution limited to 1.6×1.6 – 2×2 mm^2 [9-12]. High-resolution prostate DWI (e.g. in-plane resolution $\leq$1.0×1.0 mm^2) can also enable ADC mapping with less partial volume averaging effects [13,10], which may improve the delineation of PCa when the tumor is intermixed substantially with adjacent normal tissue and smaller imaging voxels are desired for better tumor differentiation [13]. However, it is technically challenging to achieve high-resolution prostate DWI while maintaining SNR [14]. First, the temporal footprint of the diffusion encoding gradients and the associated substantial TE increase for higher-resolution DWI protocols using longer EPI readout durations using conventional BIPOLAR and MONO diffusion encoding methods results in additional T_2 decay that reduces SNR [14]. Second, the SNR also decreases in proportion to the reduction of voxel size [14], and now it is more common clinically to use a phased-array body coil instead of an endorectal coil for prostate MRI. Since for standard prostate DWI at moderate resolution (e.g. 1.6×1.6 - 2×2 mm^2), signal averaging (e.g. 6-10) is already a common strategy to address the intrinsically low SNR [8], further increasing the number of averages for higher spatial resolution may lead to prolonged exam durations. Therefore, there are unmet needs to improve the SNR of prostate DWI to enable higher spatial resolution and finer depiction of prostate tissue through development of advanced DWI acquisition and reconstruction methodologies.

In addition to the limitations in prostate DWI image quality such as geometric distortion, limited SNR, and low spatial resolution, the microstructural heterogeneity of prostate tissue including PCa constituted another challenge for quantitative modeling and interpretation of

prostate MRI signals, including DWI, to reliably characterize PCa and predict disease aggressiveness [15].

For example, at the microscopic scale, prostate tissue comprises different mixtures of epithelial cells (~10 micron), stromal cells (~10 micron), ductal lumen space (50~100 microns), and microvasculature (~10microns) depending on anatomical zonal locations and tissue types (e.g. benign prostatic hyperplasia [BPH], PCa and normal) [16]. It is well known that early disease changes occur at the microscopic scale, and the gold standard for PCa diagnosis is histopathology analysis [17]. The pathologist assigns a Gleason Score to indicate the aggressiveness of PCa based on its microarchitecture and microanatomy appearance under the microscope [17]. Because clinical MRI scanner hardware can only acquire images with mm-level spatial resolution, with voxel sizes far too large to directly visualize these microscopic histological features of PCa, the standard prostate DWI technique has intrinsic difficulty to characterize these critical histopathological features of PCa for reliable prediction of PCa aggressiveness [15]. Thus, histopathological evaluation remains the reference standard and invasive biopsies are still necessary during the entire course of PCa screening, surveillance, and treatment [18].

Therefore, developing advanced multi-component MRI signal models to resolve contributions from sub-voxel microscopic tissue compartments is a promising direction to improve the ability of prostate MRI to characterize prostate microstructure and cancer [15]. In the past decade, several multi-component signal models, based on either multi-component modeling of diffusion MRI or T_2 MRI signals have been proposed for prostate microstructural MRI [19-22], and these prostate microstructural MRI techniques demonstrated promising results suggesting improved separation of clinically significant PCa (csPCa), often defined as Gleason Score >3+3 [17], and indolent PCa compared to the standard ADC models that assumed a single tissue compartment in the prostate,

in research settings [23]. However, current prostate multicomponent MRI signal models still face challenges. First, there exist some degree of overlap in compartmental diffusivity or T_2 relaxation time (e.g. between epithelium, stroma and lumen) that renders the separation of signals from prostate microscopic tissue compartments based on a single contrast mechanism (e.g. only diffusion or only T_2) ambiguous [21,24]. Second, current prostate microstructural MRI techniques usually rely on strong assumptions of the underlying tissue microstructure properties, e.g. the number of tissue compartments and the approximate diffusivity or T_2 relaxation time of each tissue compartment need be known a priori, to form a mathematical model for fitting the MRI signals for inferring tissue microstructure [25-27]. This increased the risk of model-induced bias (e.g. over-fitting) and made the interpretation of fitting results more challenging as fitted microstructure properties could be largely influenced by model input parameters that originated from the assumptions [26,27]. Third, the validation of prostate microstructural MRI to ground truth, such as histological measures of microscopic tissue compartments, is generally lacking, and such validation is critical for establishment of prostate MRI techniques for inferring prostate microstructure and microenvironment. Fourth, in order to perform multi-component signal modeling, more MRI contrast encodings in either the diffusion encoding space (e.g. b-values), T_2 relaxation encoding space (e.g. echo time [TE]), or both dimensions are needed; this inevitably increases scan time compared to conventional MRI techniques (such as ADC or T_2 mapping) [25]. Therefore, there is also an immediate need for the development of acquisition acceleration techniques to reduce scan time while maintaining accuracy of prostate microstructure mapping.

1.2 **Specific Aims**

The overall goal of this research work is to contribute to the development of quantitative prostate diffusion MRI techniques and multi-dimensional diffusion-relaxation correlation microstructure MRI techniques for non-invasive characterization of prostate cancer. Quantitative prostate MRI techniques have the potential to provide more reliable characterization of PCa disease states and predict PCa aggressiveness for better management of PCa for improved patient care. This work aims to achieve improved image quality such as higher SNR and reduced geometric distortion for quantitative prostate diffusion MRI, and expand the ability of prostate MRI for inferring prostate microstructure and microenvironment by developing multi-dimensional diffusion-relaxation correlation MRI techniques. The research work presented here can be divided into two themes with a total of four aims. These are:

Theme 1: Development of quantitative diffusion MRI techniques with improved geometric fidelity and signal-to-noise ratio for standard and high-resolution prostate DWI.

Aim 1 – Develop an eddy current-nulled convex optimized diffusion encoding (ENCODE) based prostate DWI technique that achieves short echo time (TE) to maintain SNR while reducing prostate geometric distortion from eddy-current and susceptibility effects.

Aim 2 – Develop a combined TE-minimized ENCODE diffusion encoding acquisition with Random Matrix Theory-based denoising reconstruction to improve the SNR and robustness of high-resolution (in-plane: 1.0x1.0 mm^2) prostate DWI and ADC mapping.

Theme 2: Development of multi-dimensional diffusion-relaxation correlation MRI for improved characterization of prostate cancer tissue microstructure.

Aim 3 – Perform a first proof-of-concept *ex vivo* evaluation and validation of diffusion-relaxation correlation spectrum imaging (DR-CSI) at 3 T for quantifying microscopic tissue compartments (epithelium, stroma and lumen) in prostate cancer using whole-mount digital histopathology as the reference standard.

Aim 4 – Develop and evaluate sequential backward selection analysis for acceleration of DR-CSI through subsampling of the diffusion-relaxation contrast encoding space while maintaining accuracy of prostate microstructure mapping in PCa.

1.3 Overview of the Thesis Structure

Chapter 2 will introduce general concepts and technical background about prostate MRI, diffusion MRI and prostate microstructure MRI for the subsequent chapters. The remaining thesis chapters (see **Figure 1.1**) will present the technical and experimental contributions for developing quantitative prostate diffusion MRI and multi-dimensional diffusion-relaxation correlation MRI for characterization of PCa. **Figure 1.1** describes the overall thesis structure, outlining how specific developments and evaluations contribute to the two overall themes.

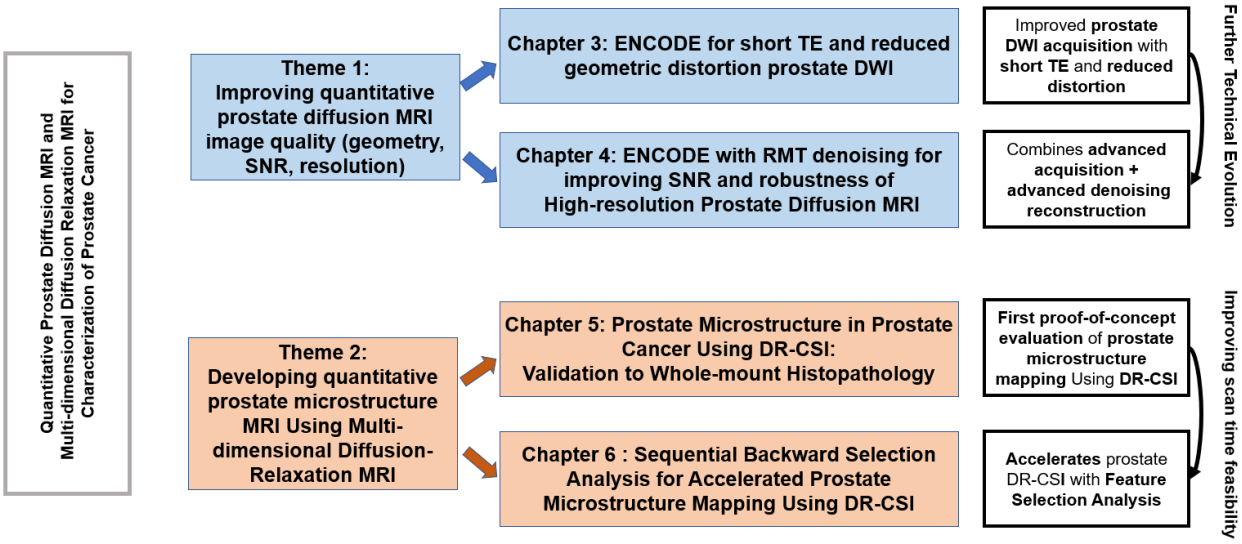

Figure 1.1. Outline of the technical developments and evaluations described in this thesis.

In **chapter 3**, we first evaluated the recently developed eddy current-nulled convex optimized diffusion encoding (ENCODE) [28] framework for designing diffusion encoding waveforms for prostate DWI to achieve short echo time and eddy current distortion compensation. ENCODE prostate DWI was evaluated against the conventional MONO and BIPOLAR diffusion encoding techniques in terms of eddy current-induced distortion, signal-to-noise ratio (SNR) in prostate peripheral zone (PZ) and transitional zone (TZ), and diagnostic image quality. We studied a NIST diffusion phantom, one *ex vivo* prostate specimen, 10 healthy volunteers and 5 patients with PCa to investigate the potential advantages of ENCODE for improving prostate DWI SNR and suppressing eddy current-induced distortion. In a subsequent study, we hypothesized that by combining ENCODE with a reduced phase-encoding field of view (FOV) acquisition technique [29], both eddy current and susceptibility induced geometric distortions in the prostate can be addressed, which may lead to further reduction in geometric distortion compared to a clinical BIPOLAR DWI sequence that only compensated for eddy current distortion. A pilot cohort of 36

patients with clinical suspicion or diagnosis of PCa were recruited for prospective evaluation of rFOV-ENCODE with respect to clinical BIPOLAR DWI in terms of quantitative geometric distortion analysis using the Dice coefficient of prostate boundary overlap with the reference T2W TSE MRI and qualitative radiological image quality scoring by two expert abdominal radiologists.

In **chapter 4**, we further advanced prostate DWI by combining advanced DWI acquisition strategies (such as ENCODE and rFOV) with advanced random matrix theory (RMT)-based denoising reconstruction methodology ("ENCODE-RMT") for maintaining the SNR of technically challenging high-resolution (in-plane: 1.0x1.0 mm^2) prostate diffusion MRI using phased-array body coil only. In order to maintain independent identically distributed (i.i.d.) zero mean Gaussian noise in the data as assumed by RMT for more robust signal and noise component separation [30], we designed and implemented an in-house DWI denoising reconstruction pipeline that was built upon the original Marchenko-Pastur distribution principal component analysis (MP-PCA) algorithm [31], while adopting recent technical developments in using complex DWI raw k-space data and performing coil channel noise normalization to compensate for noise amplification associated with parallel imaging reconstruction. The implemented denoising reconstruction pipeline was validated by comparing the difference between the original and denoised DWI signals against a zero-mean Gaussian distribution. To assess the technical performance of the proposed high-resolution ENCODE-RMT DWI technique, we prospectively scanned 11 patients with clinical suspicion of PCa and compared high-resolution ENCODE DWI, with and without RMT denoising reconstruction, to a standard resolution clinical BIPOLAR DWI in terms of key technical parameters such as SNR and ADC quantification robustness (precision and accuracy).

In **chapter 5**, we investigated the diffusion-relaxation correlation spectrum imaging (DR-CSI) MRI technique [32] for characterizing prostate microscopic tissue compartments (such as

epithelium, stroma and lumen) in PCa. Compared to existing multicomponent MRI signal models proposed for prostate microstructure mapping, the DR-CSI technique has unique advantages of not pre-assuming the number and MRI properties of tissue compartments in prostate MRI signals for probing prostate microstructure and microenvironment. Another common limitation of existing prostate microstructure MRI techniques is the lack of validation with respect to whole-mount histopathology, which means that a solid relationship between the model-predicted signal components and histopathological microscopic tissue compartments was not established. In this proof-of-concept study, we performed validation of DR-CSI for quantifying microscopic tissue compartments in the prostate using spatially aligned digital whole-mount histopathology (WMHP) as the reference. We performed *ex vivo* DR-CSI at 3 T in 9 fresh prostate specimens obtained from PCa patients who underwent radical prostatectomy, and used 3D-printed patient-specific prostate molds to align *ex vivo* DR-CSI slices to spatially matched WMHP slides for comparing DR-CSI signal components to area fractions of epithelium, stroma and lumen quantified by digital histopathology, in benign and PCa regions defined by a pathologist. The number of sub-voxel signal components resolved by DR-CSI and its relationship to underlying microscopic tissue compartments quantified by WMHP were investigated and compared.

In **chapter 6**, we explored and evaluated diffusion-relaxation encoding space subsampling techniques based on sequential backward selection (SBS) analysis to accelerate DR-CSI acquisition while maintaining the accuracy of estimated prostate microstructure parameters. The Mean Squared Error (MSE) of the estimated T_2-diffusivity signal spectrum from subsampled TE-b encoding schemes with respect to the reference reconstruction using all acquired TE-b encodings were defined as the cost function for the SBS analysis. We acquired a reference DR-CSI dataset using a total of 28 TE and b-value (diffusion-relaxation) encodings in 15 fresh *ex vivo* prostate

specimens obtained from PCa patients who underwent radical prostatectomy. We then performed SBS analysis to reduce the number of TE-b encodings as much as possible while maintaining a certain threshold level of accuracy for estimating DR-CSI signal component fractions for characterizing prostate microstructure. The evolution of the cost function and the most important TE-b encodings according to the SBS analysis were reported. The accuracy of signal component fractions in 30 PCa regions defined by WMHP, using the minimal set of 9 TE-b encodings selected through SBS analysis, were evaluated against reference values obtained with all 28 TE-b encodings using linear regression and Bland-Altman analysis. This study provided technical validation of the accuracy of accelerated DR-CSI acquisition for prostate microstructure mapping in PCa, and established one practical strategy to achieve faster prostate microstructure MRI that could benefit future *in vivo* translation.

Finally, in **chapter 7** we concluded the thesis with a summary of all these investigations, technical developments and evaluations, and discuss future directions and outlook in the related research topics.

Chapter 2 **Background**

2.1 **Prostate Cancer (PCa) and PCa Management**

Prostate Cancer (PCa) is the second most common cancer diagnosed in men in the U.S. in 2022 [33], and the American Cancer Society estimated that PCa will lead to more than 34,700 deaths in the U.S. in 2023 [1].

PCa is unusual among solid tumors in the sense that it can exhibit a broad spectrum of biology and span a large range of disease aggressiveness [17]. Many PCa are slowly growing and localized within the prostate gland, which may not cause serious harm and would not warrant immediate intervention, while some PCa can grow and spread rapidly and become life threatening [34]. In the case of potentially lethal PCa, early diagnosis and definitive treatment are paramount for improving outcomes.

These distinct characteristics of PCa means that the priority for clinical management of PCa is to accurately detect and distinguish the clinically significant PCa (csPCa), often defined as Gleason Score (GS) >3+3 [17], from indolent PCa, assess the extent of the disease, and determine the risk of disease progression, such that undertreatment of high-grade PCa can be minimized, while overdiagnosis and overtreatment in men with low-grade PCa can be avoided [34,35]. Treatment often leads to incontinence and impotence, negatively impacting men's quality of life [35], and should thus be considered carefully in terms of risks and benefits.

Prostate-specific antigen (PSA) testing followed by transrectal ultrasonography (TRUS) guided systematic biopsy [36] is the conventional PCa diagnosis pathway and has led to a decrease in PCa related death [37]. However, the PSA test has low specificity, and combined with the blind sampling nature of TRUS guided systematic biopsy, has resulted in the overdiagnosis and overtreatment of PCa with low metastatic risk in general populations [38]. It is therefore clear that

newer technology with high sensitivity and specificity for PCa screening and diagnosis is needed to improve clinical management of PCa for better patient care.

2.2 Multi-Parametric MRI for Clinical Management of PCa: Success and Areas for Improvement

The advent of multi-parametric MRI (including T_2-weighted [T2W] MRI, Diffusion MRI and Dynamic Contrast-Enhanced [DCE] MRI) has revolutionized the diagnostic pathway of PCa in the past decade [18], and has enabled improved localization and detection of csPCa over the traditional PSA + TRUS method [2].

The T2W MRI sequence has high spatial resolution (typical in-plane resolution of 0.6x0.6 mm^2) to generate detailed delineation of prostate zonal anatomy and anatomical structure, where PCa lesions tend to appear as hypo-intense foci [18].

The diffusion MRI sequence provides functional information regarding the degree of cellular packing through sensitizing MRI signals to the water molecules' Brownian motion with strong magnetic field gradients, where PCa typically exhibits restricted diffusion due to pathology associated tissue microstructure changes [3]. Due to its high sensitivity to PCa, DWI now serves as the most important sequence within mp-MRI for assisting the detection and grading of PCa [3].

The DCE MRI sequence provides information about the distribution of blood vessel density in prostate glands through perfusion measurements [18]. The perfusion estimates are obtained by pharmaceutical modeling of the MRI signal dynamics throughout the wash in/out phases of contrast media, where PCa displays earlier signal enhancement and higher perfusion than benign tissue due to tumor angiogenesis [39].

Because mp-MRI allows the non-invasive assessment of the entire prostate and provides spatial localization and functional information of tissue sites suspicious of harboring PCa [40], it has generated a paradigm shift of the PCa management strategy as biopsy no longer needs to be performed in a blind manner and can be precisely targeted to suspicious locations based on lesion visibility and margins on MRI [3]. This helps to reduce the amount of unnecessary biopsy cores, diminish pain and side-effects in patients [41], and can also lead to increased detection of PCa in the anterior prostate, which is easier to be missed through traditional TRUS guided biopsy [41]. Mp-MRI has now been widely adopted clinically for guidance of targeted prostate biopsy (e.g. MRI-ultrasound prostate fusion biopsy [42]) and has shown great promise for PCa risk stratification (e.g. a negative MRI could help rule out the presence of csPCa and avoid unnecessary biopsy [43]). Mp-MRI is playing substantial roles throughout the diagnosis, treatment, and follow-up of PCa [2], and may play a future role in screening as the performance and overall cost-effectiveness of MRI-based screening is under active research investigation [44].

Although prostate mp-MRI has demonstrated great clinical value for detection and management of PCa, there are still substantial needs for improvement of MRI for prostate imaging from both image formation (acquisition and reconstruction) and interpretation perspectives. The current standard acquisition and interpretation scoring system of mp-MRI is the Prostate Imaging Reporting and Data System (PI-RADS) v2.1 [39], which has only moderate inter-reader agreement due to the qualitative and subjective nature of PI-RADS analysis of MRI findings [45]. Interpretation of mp-MRI based on PI-RADS still misses PCa in up to 45% of men [46], and has limited ability to robustly distinguish csPCa from indolent PCa [40]. Besides the variability in image interpretation [45], there is also considerable variability in the image quality and artifact level among different sequences in mp-MRI. For example, prostate DWI can suffer from severe

geometric distortion of the prostate, obscuring PCa diagnosis [47].The degree of artifacts can also vary substantially across different MRI systems [48], e.g. due to different gradient hardware properties. The image quality can also vary considerably across subjects (e.g. different degree of tissue susceptibility effects due to presence of rectal air or not [49]).

As a result of the current suboptimal ability of MRI for detection and grading of PCa, invasive biopsy for histopathology analysis of PCa remains the gold standard for diagnosis [50]. Based on the microscopic appearance of PCa, the pathologist assigns a Gleason Score to indicate its aggressiveness [17], which has been shown to be the most indicative marker for predicting the long term prognosis of PCa [51]. Therefore, MRI technologies must be improved to enable better diagnosis and characterization of PCa.

In the next section, I will first review the key technical factors and limitations impacting the image quality of the DWI component of prostate MRI, which will provide context and motivations for the development of new prostate DWI acquisition and reconstruction techniques in **chapter 3** and **chapter 4** respectively, to achieve improved image quality for prostate DWI.

2.3 Technical Factors Impacting Image Quality of Prostate Diffusion MRI: Geometric Distortion, SNR and Spatial Resolution

2.3.1 Prostate DWI Image Quality Limiting Factor: Geometric Distortion

Eddy Current-Induced Geometric Distortion

In this section, I will introduce the two main sources of geometric distortion in prostate DWI using the common single-shot spin-echo echo-planar imaging (EPI) sequence. The first source of distortion comes from eddy current effects introduced by the application of high gradient

amplitude diffusion encoding waveforms. One of the standard DWI encoding schemes is the monopolar (MONO) waveform [5], which has a short temporal footprint, therefore permitting a relatively short TE to limit T_2 signal decay. However, the two gradient lobes of the MONO waveform before and after the 180 degree refocusing pulse excite eddy current fields that do not cancel each other by the end of diffusion encoding duration, leading to a residual magnetic field perturbation that lasts during the EPI readout [52]. This residual magnetic field leads to alterations in the actual EPI k-space data sampling trajectory and results in image distortion artifacts after reconstruction.

Because the eddy current field is a vector quantity, whose direction is determined by the orientation of diffusion encoding gradients (e.g., diffusion encoding gradients applied along x, y or z directions), the particular direction of distortion (image shearing/widening) will be different in DWI acquired at different directions [53]. In the context of prostate DWI, this leads to inconsistent prostate tissue positions, including prostate boundaries, across diffusion directions as shown in the example in **Figure 2.1**. The degree of distortion also scales with the strength of diffusion weighting (i.e., b-values); the diffusion-weighted image with the highest b-value will display the greatest degree of eddy current distortion.

Such inconsistency in prostate boundaries will affect the final prostate geometry after trace averaging. Although subtle, this constitutes one source of distortion that can negatively impact the geometric fidelity of prostate DWI. Blurriness of tissue boundaries and features have been reported in the literature for body DWI using MONO waveform when eddy current-induced distortions were not retrospectively corrected, e.g., using software registrations [54].

From the diffusion encoding aspect, one solution to mitigate eddy current-induced distortion is to use a twice-refocused spin-echo sequence with BIPOLAR diffusion encoding gradient

waveforms [6], as shown in **Figure 2.1B**. The BIPOLAR waveform used specially designed gradient lobes with opposing polarities to cancel out eddy current fields induced by each individual gradient lobe's ramp up and ramp down, therefore reducing geometric distortion from eddy current effects (see example in **Figure 2.1B**). However, such features come with the price of increased achievable minimal TE compared to MONO, leading to lower SNR due to a greater degree of T_2 signal decay [6,5]. This can be problematic for prostate DWI as it already inherently has low SNR because of the large distance between the surface coil arrays and the center of the pelvis [55,56]. This means to achieve the same SNR as MONO, more signal averaging and longer scan time would be needed for prostate DWI using BIPOLAR. In our institution, BIPOLAR DWI was the default clinical DWI sequence [40] for body imaging including for prostate, as it offers intrinsic eddy current distortion compensation which is valued for accurate depiction and spatial localization of prostate tissue including PCa. However, currently there is no consensus in literature which diffusion encoding technique (MONO or BIPOLAR) is overall superior for prostate DWI, possibly due to the unsatisfactory trade-offs between SNR and eddy current-induced distortion reduction with these methods. Efforts to resolve such trade-offs for prostate DWI are presented in **chapter 3** using the recently developed Eddy Current-Nulled Convex Optimized Diffusion Encoding (ENCODE) gradient design framework introduced by Aliota E et al [28].

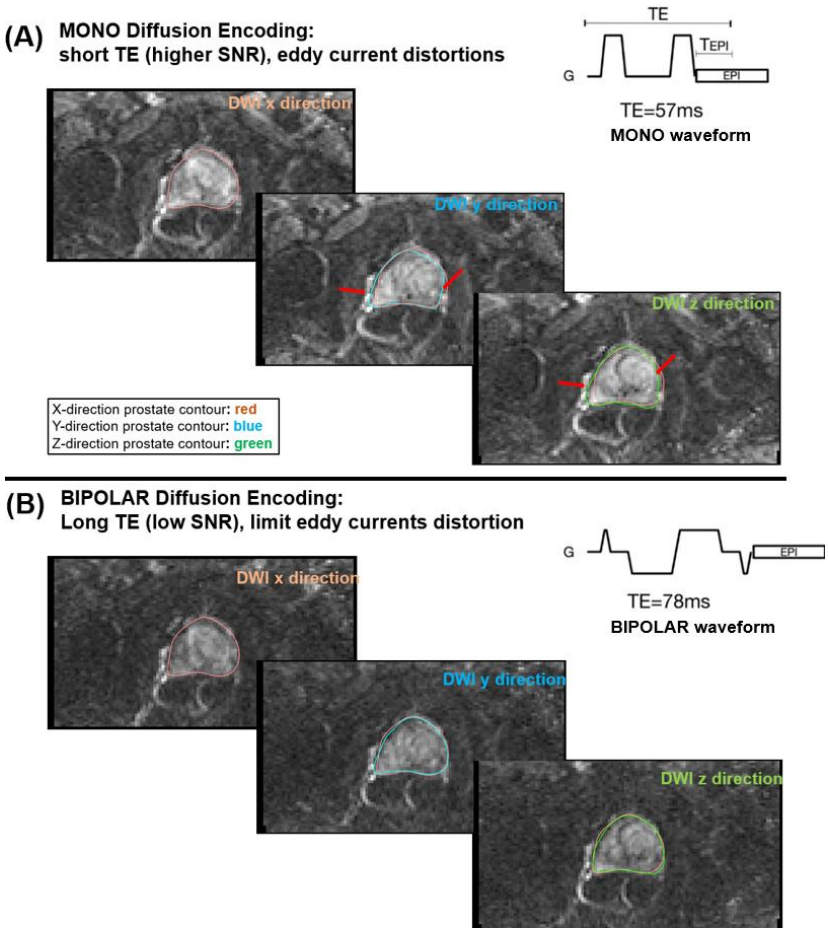

Figure 2.1. **(A)** Representative example showing that prostate DWI suffered from directional dependent distortions (red arrows) due to eddy current effects induced by strong diffusion encoding gradients (b=800 s/mm^2) using MONO waveform. These distortions lead to spatially inconsistent prostate boundaries across DWI directions, and affect the geometric fidelity of trace weighted DWI. **(B)** While BIPOLAR diffusion waveforms can reduce eddy current and limit distortions, it has substantially longer TE leading to lower SNR than MONO.

Susceptibility-Induced Geometric Distortion

Another major source of geometric distortion in the prostate is susceptibility differences that lead to spatial inhomogeneity in the magnetic field [49]. Unlike the subtle nature of eddy current-induced directionally dependent distortions, susceptibility-induced distortion is usually more obvious as it impacts all DWI images including the non-diffusion-weighted b0 image, and the appearance and degree of distortion manifest in a comparable manner across all acquired b-values [49].

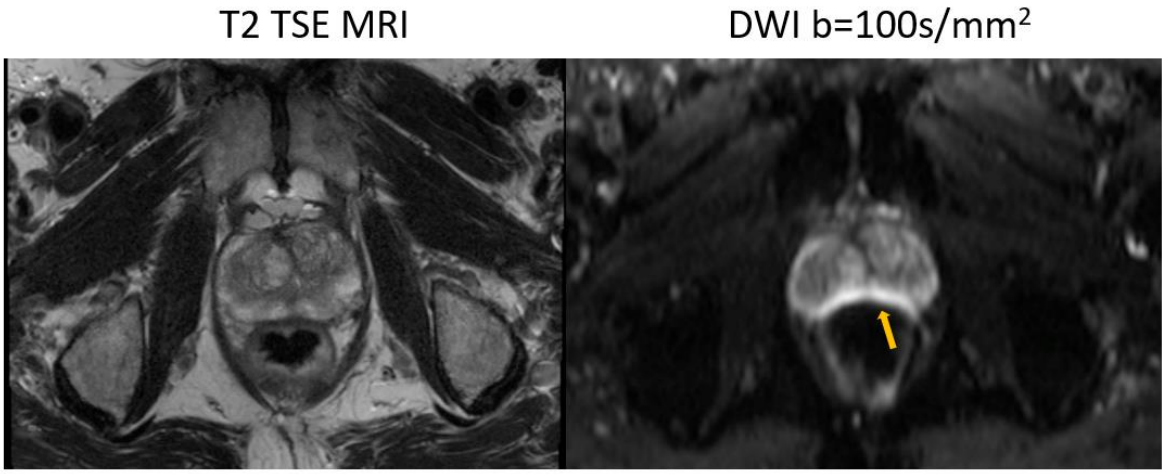

Figure 2.2. Representative example showing prostate DWI suffered from geometric distortion artifacts with signal pile up in comparison with the anatomical reference T2 weighted (T2W) Turbo Spin Echo (TSE) MRI. The large susceptibility difference at rectal tissue-air interface led to severe

As the prostate resides adjacent to the rectum, any gas retention in the rectum will create a sharp susceptibility gradient along the rectal tissue-air interface that directly impacts prostate tissue signal. This B_0 field inhomogeneity due to the susceptibility gradient will lead to non-linear displacement of imaging voxels after image reconstruction of DW-EPI data [14], and the specific direction of the displacement depends on the phase-encoding direction, which can manifest as

severe signal pile up as shown in the example in **Figure 2.2**. This can be especially problematic as more than 60% of PCa resides in prostate peripheral zone, which happens to be in the immediate vicinity of the rectum. The signal pile up artifacts can obscure PCa signals and render the DWI non-diagnostic. Substantial efforts to reduce such distortion artifacts have been made by the MRI scientific and clinical community. In terms of clinical practice, mechanical measures have been introduced to remove rectal gas prior to an MRI exam, e.g., using a catheter or bowel preparation using enema [57]. These measures were shown to be effective for avoiding severe susceptibility induced geometric distortions in prostate DWI [57] ,but could be uncomfortable for some patients.

From the DWI acquisition side, alternative DWI sequences such as readout-segmented EPI DWI [58], reduced field of view (rFOV) DWI using specialized radiofrequency pulses via parallel transmit (pTx) systems [59], or rFOV DWI using outer volume suppression pulses [60,29], are being developed and evaluated for reducing susceptibility-induced distortion in the prostate. These DWI sequences, including the rFOV ENCODE DWI technique evaluated in **chapter 3** and **chapter 4**, aim to prospectively reduce the degree of geometric distortion by reducing the duration of EPI readout through increased phase-encoding bandwidth [53] which are the key MRI technical parameters determining the resultant distortion magnitude, as a shorter EPI duration will lead to reduced accumulation of phase errors in the presence of off-resonance effects.

On the other hand, DWI geometric distortion can also be addressed from the reconstruction aspect. For example, a B_0 field map could be acquired in advance, e.g., using a gradient echo sequence or using EPI acquisitions with opposite phase encoding polarities, to provide additional information for improved model-based DWI reconstruction [61]. The estimated B_0 field map can be incorporated into an imaging model to mathematically solve for the "corrected" positions of displaced imaging voxels [61], therefore reducing geometric distortion in reconstructed DWI.

Parallel-imaging acquisition and reconstruction is also an effective strategy to reduce EPI distortion by reducing the effective phase-encoding bandwidth by skipping k-space lines [53]. This produced a smaller phase-encoding FOV while the resulting aliasing artifacts were resolved through algorithms such as GeneRalized Autocalibrating Partial Parallel Acquisition (GRAPPA) [62].

Lastly, all these separate strategies can be combined to achieve a greater degree of overall geometric distortion reduction. The rFOV ENCODE technique investigated in this thesis (**chapters 3 and 4**) adopted such an integrated approach by combining rFOV and parallel imaging for reducing susceptibility-induced distortion while addressing eddy current-induced distortion using ENCODE diffusion encoding waveforms.

2.3.2 Prostate DWI Image Quality Limiting Factor: SNR

SNR is a fundamental limiting factor for DWI in general, as achieving sensitivity of image contrast to diffusion processes relies on the application of strong gradient amplitudes to attenuate MRI signals through inducing intra-voxel spin dephasing [53]. Prostate DWI has intrinsically lower SNR than most other DWI applications (e.g., in the brain) since the prostate is located deep in the body and is far away from the phased array receiver coil elements. Moreover, the detection of PCa against background normal tissues required that DWI be acquired with a sufficiently large maximum b-value, e.g., b_{max}=800~1000 s/mm^2 per PI-RADS v2.1 recommendation [39], to achieve enough sensitivity to low diffusivity prostate tissues including PCa.

Given the tremendous need to address the limited SNR of prostate DWI, the MRI community has long engaged in the development of physical and technical solutions (e.g., from acquisition and reconstruction aspects) for this problem.

Clinically, the endorectal coil was proposed in the 1990s to improve prostate MRI SNR by having the receiver coil elements placed directly adjacent to the prostate [63]. For the MRI systems at common intermediate field strengths (e.g., 1.5 T), it was shown that the endorectal coil was necessary to achieve good diagnostic quality for prostate DWI [55]. As the hardware evolved over time, 3 T MRI became the state of the art for prostate MRI, and many studies have found that the use of endorectal coil may not provide as great a benefit to improving SNR compared to phased-array body coils, as it was at 1.5 T [63]. Nonetheless, endorectal coil provided 2-5 times higher SNR for prostate MRI including DWI regardless of field strengths [55]. The downside of endorectal coil is also apparent as many patients found its placement uncomfortable [63]. Although there are still ongoing debates in literature regarding the advantages and necessity of endorectal coil for 3 T prostate MRI, a majority of institutions are now opting to stop using the endorectal coil to improve patient comfort and streamline MRI scan setup [63].

From the acquisition aspect, the most widely used strategy to increase DWI SNR is through repeated acquisitions for signal averaging [14]. As shown in the example in **Figure 2.3**, the SNR improved for prostate DWI as the number of averages increased, which approximately follow $SNR \propto \sqrt{the\ number\ of\ repetitions}$. This approach is robust and effective. However, it inevitably increases the scan duration in proportion to the number of repetitions. Theoretically, the repetition number should be "optimized" to approximately assign more signal averages to DWI acquisition at higher b-value and a minimal number of averages should be used for low b-value DWI to manage overall scan time [8]. However, there are currently no consensus on exactly how many averages should be assigned according to applied b-values as different centers usually have different prostate DWI protocols (and different MRI systems from different vendors) complicating protocol design [48].

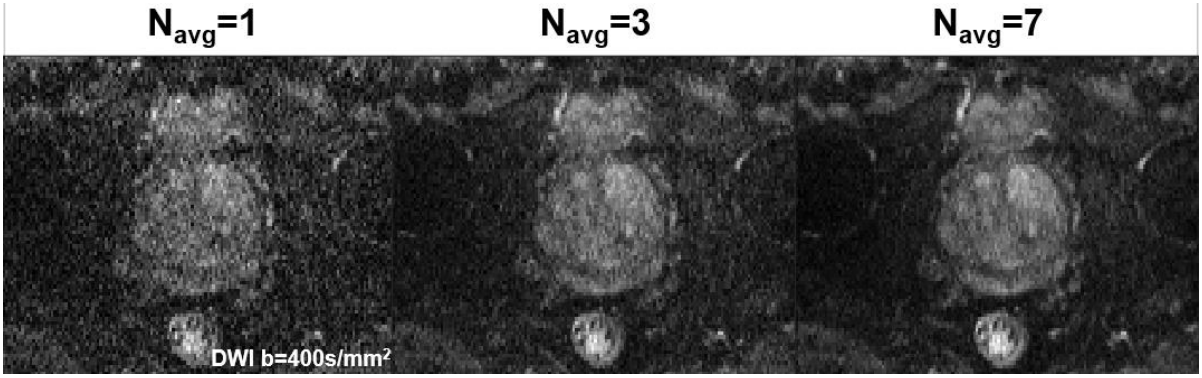

Figure 2.3. Representative example showing the use of repeated acquisitions to perform averages of prostate DWI for improving SNR, the effects of using different number (1-7) of averages were shown. DWI averaging is commonly performed using magnitude images instead of complex images to avoid signal cancellation due to phase errors introduced by bulk motion across repetitions.

Since signal averaging can be time consuming, alternative acquisition strategies to improve SNR are highly desirable. The recently developed Convex Optimized Diffusion Encoding (CODE) framework introduced by Aliotta et al. offers a novel strategy to improve DWI SNR by optimizing the temporal footprint of diffusion encoding gradients using convex optimization to achieve the shortest possible TE for any given targeted b-value and imaging protocol [64]. This approach improved SNR through minimizing the amount of T_2 signal decay at the DWI signal echo time and does not increase scan time, in contrast to the averaging approach. In chapter 3, we investigated a variation of the CODE technique, the ENCODE technique, for improving prostate DWI SNR in prostate peripheral zone and transitional zone while limiting eddy current-induced distortion.

From the reconstruction aspect, the resultant SNR of reconstructed DWI can also be largely influenced by reconstruction pipeline. For example, the most standard sum of squares (SOS) algorithm for combining images from multiple coil elements (channels) will produce much noisier

prostate DWI compared to an improved algorithm called adaptive coil combination (ACC) [65], as shown in the example in **Figure 2.4**.

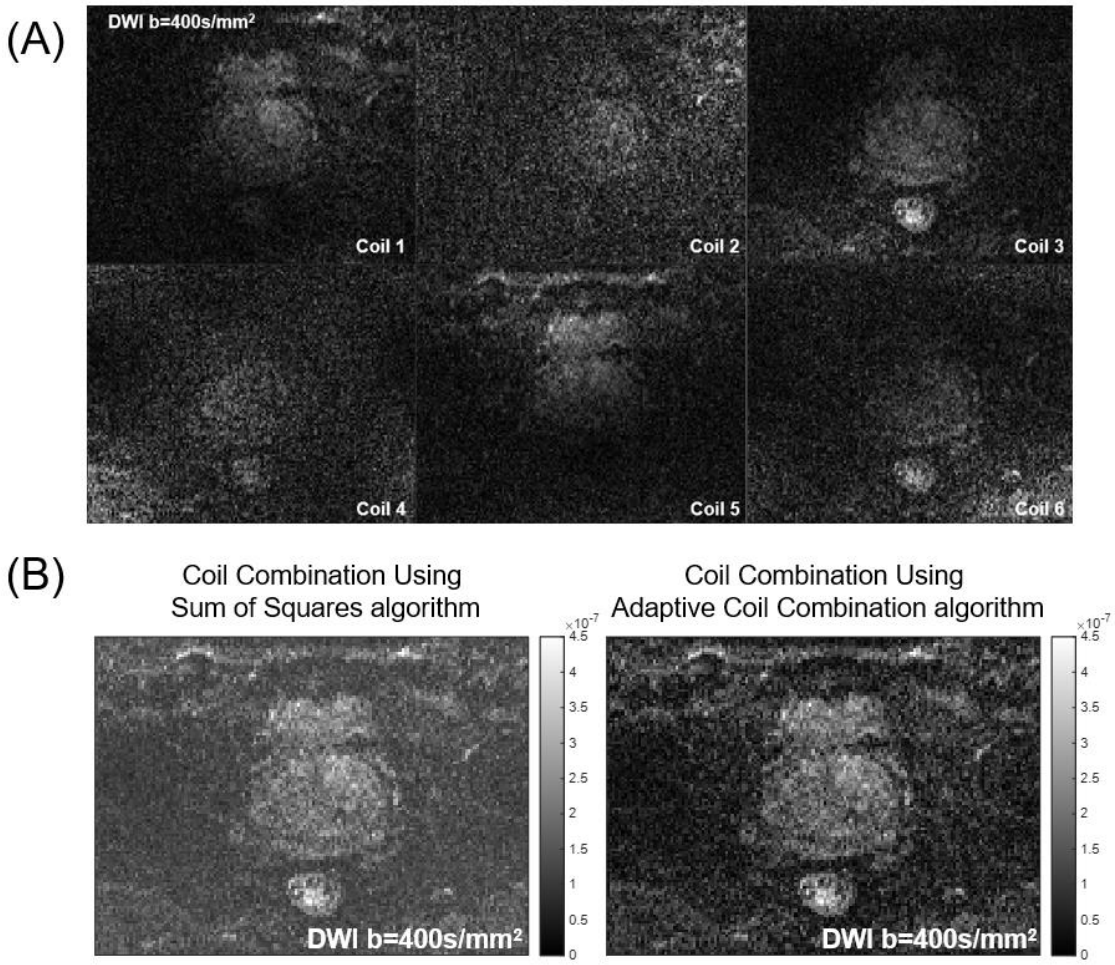

Figure 2.4. **(A)** Representative example showing inherently low SNR of prostate DWI from each coil channel, and **(B)** the effects of coil combination reconstruction algorithms in resultant SNR of coil combined DWI images (e.g., sum of squares algorithm vs. adaptive coil combination method).

The ACC algorithm was designed to specifically optimize the coil combination weights to maximize the degree of noise cancellation for achieving near optimal post coil combination SNR by considering the phase variations of the complex coil sensitivities across coil channels [65]. Likewise, there are tremendous opportunities to improve DWI SNR through advanced reconstruction algorithms to achieve better noise suppression during the image formation pipeline.

The work in **chapter 4** investigated one such approach called random matrix theory based denoising [66,30], in the context of improving SNR for high-resolution prostate DWI.

2.3.3. Prostate DWI Image Quality Limiting Factor: Spatial Resolution

As part of the multi-parametric prostate MRI protocol, DWI is usually acquired with a much lower spatial resolution than its T2W MRI counterpart [56]. A typical 2D T2W TSE MRI has an in-plane resolution around 0.6x0.6 mm^2, while the DWI is acquired with in-plane resolution around 1.6x2 mm^2, which has almost 3 times larger voxel size. These prominent spatial resolution differences can be easily appreciated visually as DWI images have much blurrier tissue features, e.g., as shown in the example in **Figure 2.5**.

As the radiologist needs to review and find correspondence between features of interest across different components of mp-MRI, it would be more ideal if imaging characteristics, such as spatial resolution would be uniform across sequences. This is not the case in practice as DWI has much lower inherent SNR due to additional signal attenuation from diffusion encoding on top of T_2 decay. Essentially, the clinically adopted resolution of 3.5 mm^2 is a practical compromise between maintaining SNR and the level of image detail that is acceptable to radiologists.

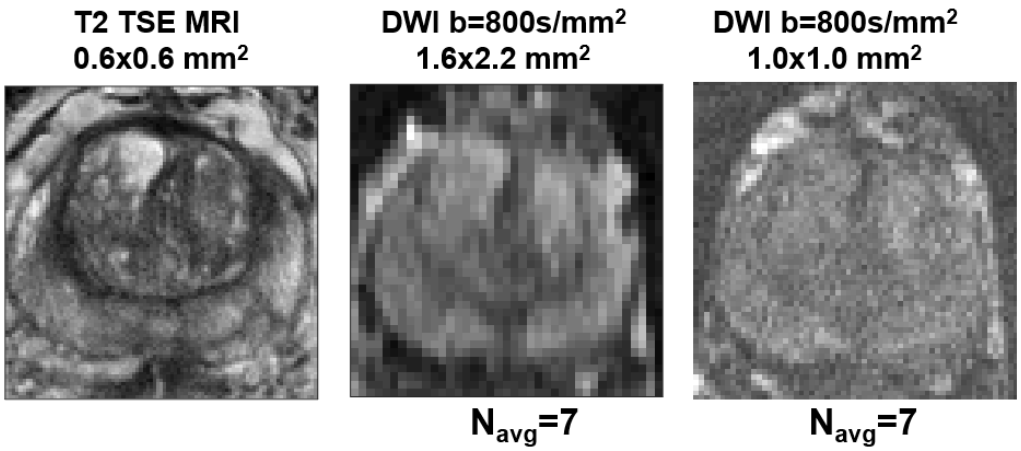

Figure 2.5. Representative example showing the SNR penalty associated with reduced voxel sizes that makes achieving higher spatial resolution prostate DWI (e.g., compared to standard clinical DWI at 1.6x2.2 mm^2 in plane resolution) technically challenging, which produced noisy DWI images at b=800 s/mm^2 even after 7 repetitions for signal averages. As a result, prostate DWI was acquired at much lower resolution than its T2W MRI counterpart.

For large PCa tumors that span several mm-sized voxels, performing DWI at a relatively low resolution may still be sufficient for tumor localization and diagnosis. However, it has been found that at least more than 30% of csPCa tend to intermix substantially with adjacent normal tissues [13]; these sparse tumors would be more likely to be missed by DWI due to the substantial partial volume averaging effects from a large 3.5 mm^2 voxel [10]. This could also contribute to underestimation of tumor volume on MRI compared to the tumor volume determined by histopathology exam after resection.

For this reason, developing DWI techniques with higher spatial resolution (e.g., in-plane 1.0x1.0 mm^2) may be a strategy to improve the diagnosis and characterization of sparse prostate tumors. However, SNR is proportional to the voxel size, and a 2-fold increase in in-plane spatial resolution will lead to a 4-fold reduction in voxel size and SNR per unit time. $V' = \frac{1}{2}\Delta x \frac{1}{2}\Delta y \Delta z = \frac{1}{4}V;\ SNR' = \frac{1}{4}SNR \propto \sqrt{Navg};$ With the same acquisition time, higher spatial resolution prostate

DWI inevitably will suffer from low SNR and result in noisy images that are inadequate for diagnosis, as shown in the example in **Figure 2.5**.

This means to maintain the same SNR level of standard low-resolution DWI, 16 times more repetitions for signal averages would be required for a 4-fold reduction in voxel size. $N'_{avg} = N^2_{avg}$. This is clearly not feasible from a scan time perspective, as standard resolution DWI already used 7-10 averages for higher b-value with a total scan time around 5 min. Thus, there is need for developing advanced acquisition and reconstruction methodologies to address the SNR limitation of high-resolution prostate DWI while managing overall scan time. We proposed to develop and apply a DWI technique that combines ENCODE acquisition with RMT-based denoising to address this intriguing technical problem in **chapter 4**.

2.4 Prostate Tissue Microstructure Factors Complicating the Quantitative Interpretation of Prostate Diffusion and T2 MRI Signals

2.4.1 Standard Mono-Exponential Signal Model and ADC in Prostate

The current clinically adopted signal model for describing prostate diffusion MRI signal is the mono-exponential signal decay model, which was derived based on the assumption that each MRI voxel contains a single tissue compartment (or single diffusion microenvironment) where water molecules undergo a diffusion process that follows a Gaussian displacement probability function at a single diffusivity rate, represented by the apparent diffusion coefficient (ADC) [15].

The mono-exponential signal model is:

$$S(b) = S_0 \exp(-b\ ADC) \quad (2.1)$$

Where b-value represents the diffusion weighting introduced by the diffusion encoding gradients and S_0 represents the signal intensity at b=0 s/mm^2.

The advantage of this single-compartment signal model is that the overall diffusion properties in prostate tissue are summarized in a single parameter ADC. A larger degree of cell packing (e.g. as seen in many cancers including PCa) is assumed to lead to lower ADC values and vice versa [67]. The associations between ADC and pathological Gleason grade of PCa have been demonstrated in multiple studies [4], and it is currently deemed as the most critical MRI-based biomarker for characterizing prostate tissue status and predicting aggressiveness [68].

2.4.2 Limitations of the ADC Model

Despite its clinical usefulness, the mono-exponential signal model (for ADC mapping) is not adequate in characterizing prostate tissue and has major limitations in terms of over-simplifying the diffusion process and ignoring heterogeneity of prostate tissue microenvironment, including in PCa. For example, due to the limited spatial resolution (~mm) of clinical MRI, it is apparent that each MRI imaging voxel would contain a large variety of cells where water molecules would exhibit distinct diffusion properties (e.g., compartmental diffusivity) within the complex microenvironment. This means the assumption of a single Gaussian displacement function for water diffusion is invalid, and the ADC calculated using the mono-exponential signal model would rather be a weighted average of the compartmental diffusivity of each microenvironment [15]. Moreover, the weighting factors will not only depend on the approximate proportions of co-existing microscopic tissue compartments (e.g., tissue component fractions), but will also depend

on DWI acquisition parameters such as echo time (TE) and diffusion weighting (b-value and diffusion time) [69,19] due to tissue compartmental T_2 differences and possible water exchange across cell membranes. This rendered the quantitative comparison of ADC derived using DWI acquisition protocols with unequal TE and b-value ranges challenging, as the difference in ADC will not only relate to difference in tissue biological status (e.g., tissue composition difference) but also reflect variations in acquisition parameters. This contributed one major source of uncertainty and variability that rendered the standardized, quantitative interpretation of diffusion MRI signals for PCa characterization based on the simple ADC model challenging [15]. Similarly, there are ambiguities in quantitatively interpreting T_2 values calculated using a mono-exponential signal model in relation to the underlying tissue biology status due to similar modeling challenge.

Due to the non-specific nature of mono-exponential signal models for heterogeneous tissue microenvironments, it is difficult or even impossible to infer microstructural information and tissue composition based on metrics like ADC that do not consider heterogeneity in water diffusion environments. This limits the ultimate capability of conventional quantitative MRI metrics (e.g., mono-exponential ADC or T_2 value) for characterizing PCa aggressiveness since pathological changes in PCa are associated with specific changes in multiple microscopic tissue compartments (e.g., epithelium, stroma and lumen etc.) and do not follow a simple scenario of increasing cellularity, as shown in **Figure 2.6** [70]. In other words, tissue microstructural changes reflect the pathological process of PCa progression, which also form the basis of histopathological evaluation of PCa, such as the Gleason score system for assessing the aggressiveness of PCa. Thus, there is a need to develop more accurate (multi-component) signal models for prostate MRI (including diffusion MRI), to better reflect the biological picture of prostate pathophysiological changes for more accurate diagnosis and characterization of PCa [15]. The group of emerging techniques that

aim to capture the microstructural information from prostate MRI and improve PCa diagnosis are commonly called prostate microstructural MRI sequences, which will be introduced in the next sections.

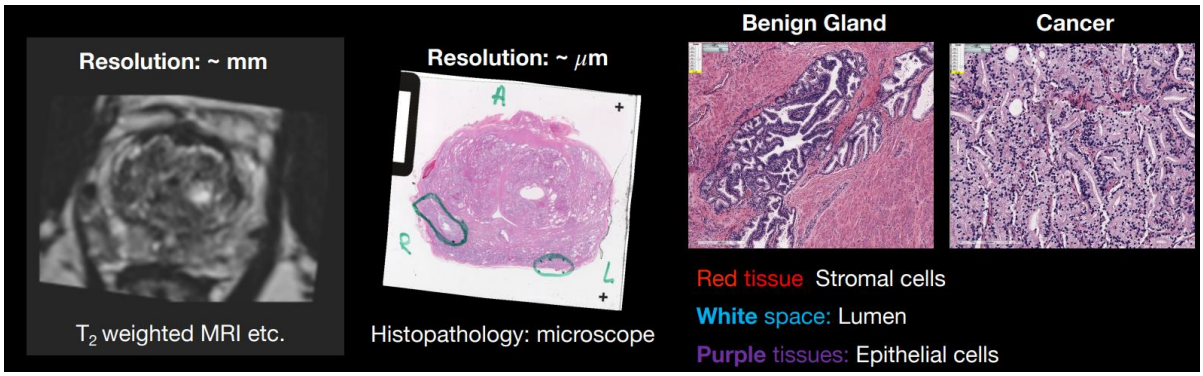

Figure 2.6. Due to the ~mm spatial resolution limit of clinical MRI, the information of prostate MRI at each pixel position reflects the mean signal averaged over a large volume of heterogeneous microscopic tissue compartments. The histopathology exam relied on analyzing the microscopic appearance of PCa for diagnosis and characterization of its aggressiveness.

2.5 Emerging Multi-Component MRI Signal Models for Characterization of Prostate Microstructure

2.5.1 Diffusion-Based Multi-Component MRI Signal Models for Prostate Microstructure

To address the limitation of the over-simplified ADC model and improve the biological specificity of prostate diffusion MRI for inferring underlying tissue microstructure, multi-component signal models have been proposed to model prostate diffusion MRI signal more accurately by accounting for the existence of multiple diffusion environments within each voxel [20].

One such representative model is the Vascular, Extracellular, and Restricted Diffusion for Cytometry in Tumors (hereafter, VERDICT) model [20]. VERDICT is based on a biophysical model of three non-exchanging water compartments within the intracellular space, extracellular-extravascular space and vascular (f_{vasc}) space.

The overall MRI signal equation for the VERDICT model is:

$$\frac{S(b)}{S(0)} = f_{vas}S_{vas}(D_{vas} = 8, b) + f_{in}S_{in}(D_{in} = 2, R, b) + f_{ees}S_{ees}(D_{ees} = 2, b) \quad (2.2)$$

Where f_{ic} , f_{ees} , and f_{vas} represent the tissue fractions of intracellular space, extracellular space and vascular space, respectively, and D_{ic}, D_{ees}, and D_{vas} represent the diffusivity of water in intracellular space, extracellular space, and vascular space. To improve model fitting in the presence of noise, some model parameters (such as D_{in}, D_{ees} and D_{vas}) were fixed to predetermined values based on literature [20].

The VERDICT model defined a set of specific water compartments within prostate tissues [20], where it is hypothesized that the intracellular space would capture the water protons' diffusion dynamics trapped in the epithelium layer (modeled as impermeable spheres with cell radius R), the water protons in extracellular-extravascular space (stroma and lumen lumped altogether) undergo unrestricted Gaussian diffusion processes represented by D_{ees}, and the vascular space is modeled as sticks with uniformly distributed orientations in all directions within a voxel.

The VERDICT model acquired DWI using a protocol with TE ranging from 50 to 90 ms (minimized TE associated with each desired b-value) with a range of b-values from 0 to 3000 s/mm^2 [20]. The VERDICT model originally assumed a single T_2 species per voxel and did not consider multi-component T_2 arising from differences in chemical environments between each

tissue compartment, but it was recently modified to accommodate compartmental T_2 differences between intracellular (T_{2in}) and extracellular spaces (T_{2ess}) [71].

2.5.2 T_2-Based Multi-Component MRI Signal Models for Prostate Microstructure

Similar efforts have been made to improve the conventional single-component T_2 model by developing multi-component signal models to accommodate differences in chemical environments (captured by compartmental T_2 relaxation times) between tissue compartments.

Multi-exponential T_2 mapping in the prostate was first demonstrated as early as in 1987 [72], and more recently re-introduced as the Luminal Water Imaging (LWI) technique [21] by recognizing that the two major T_2 components resolved in prostate MRI signals likely reflect the large T_2 difference (reflecting chemical composition) between the luminal compartment containing free water with long T_2>150 ms and the remaining cellular compartments (e.g. stroma/epithelium) with shorter T_2 in the range of 40~150 ms [21].

The MR signal model for LWI [21] is:

$$S(TE) = S_0 \int p(T_2) exp\left(-\frac{TE}{T_2}\right) dT_2 = S_0 \ [LWF \cdot exp\left(-\frac{TE}{T_{2L}}\right) + (1 - LWF) \cdot exp\ (-\frac{TE}{T_{2S}})] \quad (2.3)$$

Where LWF represents the luminal water fraction, corresponding to the signal fraction of the long T_2 signal component. TE represents a specific echo time of the turbo spin echo (TSE)

sequence used to perform LWI; T_{2L} and T_{2S} represent the long and short T_2 components. $p(T_2)$ represents the probability density function for a given T_2 species considered in the fitting of T_2 spectra.

A non-negative lease square (NNLS) algorithm was proposed to fit the T_2 spectral function $p(T_2)$ based on acquired signals at various TE for determining the positions of the two peaks with distinct T_2. The LWF was calculated by integrating the signal fraction density function over the area under the short T_2 spectral peak followed by normalization [21]. Interestingly, although the spectral formulation for LWI does not impose constraints on the number of signal components (spectral peaks) contained in T_2 MRI signal in the prostate, usually two distinct spectral peaks were resolved by the NNLS fitting [21]. A likely explanation is that the T_2 difference within cellular compartments (e.g. between epithelium and stroma) was relatively small and had some degree of overlap, thus luminal and the combined cellular compartments were more readily distinguished by multi-exponential T_2 modeling.

2.5.3 Combined Diffusion and T_2 Multi-Component Biophysical MRI Signal Models

The multi-component diffusion-based or T_2-based prostate microstructural MRI techniques have demonstrated the feasibility to quantify signal components with distinct diffusivity or T_2 relaxation time, and showed promise to improve upon the single compartment signal models (e.g. ADC) for the task of distinguishing csPCa from indolent PCa [23]. However, the results reported by various diffusion-based or T_2-based prostate microstructural MRI methods exhibited inconsistencies in terms of the estimated signal fraction from the two tissue compartments assumed by the models

[73], e.g. signal fractions between the low and high ADC compartments and signal fractions between short and long T_2 compartments.

This raised an interesting question of whether the signal components resolved by multi-exponential T_2 modeling or multi-exponential diffusion modeling were the same entities that corresponded to similar water compartmentalization (e.g. between intracellular/extracellular space, between cellular/luminal space, etc.) or actually reflected different water compartments. There were also limitations regarding the accuracy of tissue fractions estimated using pure diffusion-based multi-component signal model since the commonly used diffusion-weighted spin echo EPI sequence is also inherently T_2-weighted [14]. This embedded T_2 dependence implied the signal fraction estimated from pure diffusion acquisition will theoretically contain information regarding the T_2 relaxation time of tissue compartments, and not accurately reflect the tissue compartment fractions that the microstructural MRI method had aimed to estimate [19].

Motivated by the above limitations of pure diffusion-based prostate microstructure models, as well as research questions regarding the unknown relationship between diffusion and T_2 water compartmentalization in prostate, recently there are ongoing efforts to perform joint T_2 and diffusion modeling for simultaneous estimation of prostate microstructure parameters. The joint T_2 and diffusion prostate microstructure mapping techniques implemented two-dimensional contrast encodings in both b-value (diffusion encoding) and TE (T_2 relaxation time encoding) dimensions, and formulated multi-compartment models parameterized by the coupled compartmental T_2 and diffusivity (D) [25]. I will first introduce two joint T_2 and D biophysical multi-compartment models for prostate microstructure in this section [19,22], as they preceded the continuous spectral modeling approach for prostate microstructure that was the focus of investigation in this thesis.

Biophysical Models of Prostate Time-dependent Diffusion and Relaxometry

In 2018, Lemberskiy et al. proposed a biophysics-based two-compartment model for joint T_2 and diffusion modeling of prostate microstructure [19]. The authors made the observations that differentiation of diffusion compartments alone in the prostate were nontrivial, as different tissue compartments in prostate likely exhibit different functional forms of diffusion propagators (e.g. some compartments exhibited higher diffusion kurtosis), while reliable tissue compartment separation could more likely be performed in the T_2 domain by taking advantage of the large T_2 difference reported in luminal and cellular compartments [19].

The MRI signal model for time-dependent diffusion and relaxometry is [19]:

$$S(b,TE) = S_0(TM,T_1) \cdot [f_L \exp(-bD_L(t)) \exp\left(-\frac{TE}{T_{2L}}\right) + f_C \exp(-bD_C(t)) \exp\left(-\frac{TE}{T_{2C}}\right)] \quad (2.4)$$

Where f_L represents the luminal water fraction, corresponding to the signal fraction of the long T_2 signal component and assumed to have a higher coupled diffusivity $D_L(t)$. f_C is equal to 1-fL, and represents the cellular water fraction (combined epithelium/stroma) corresponding to the signal fraction of the short T_2 signal component assumed to be associated with lower coupled diffusivity $D_C(t)$. TE represents a specific echo time of the stimulated echo acquisition mode (STEAM) diffusion-weighted EPI sequence. T_{2L} and T_{2C} represent the long and short T_2 components corresponding to lumen and cellular compartments. TM represents the mixing time of the STEAM acquisition.

A unique feature of the proposed model is that the functional form of the time dependent diffusivity of cellular and luminal compartment was not fixed, and the determination of the D(t)

functional form was part of the model selecting process. This reduced the risk of over-fitting the model by biasing toward a certain assumed water diffusion dynamic of each compartment [19]. A potential limitation of this model formulation is that epithelium and stroma were combined into a single cellular compartment with a single T_2 relaxation time, and therefore difficult to further separate within the cellular compartments.

Three-compartment Biophysical Model for Hybrid-multidimensional MRI

In 2018, Chatterjee et al. extended the previously developed hybrid-multidimensional MRI method with a three compartment Gaussian diffusion model and constrained range of T_2 and diffusivity (D) for each compartment [22]. The authors hypothesized that the three diffusion compartments resolved at high-field strength MR microscopy (highest D in lumen, intermediate D in stroma, and low D in epithelium) could form the basis for decomposing the "hybrid" prostate MRI signal acquired at different TE and b-values into three signal components [24]. By constraining the fitted compartmental T_2 and D values with pre-determined literature values of that associated with epithelium, stroma, and lumen, the signal fractions fitted by the tri-exponential decay was defined as MRI-estimated epithelial, stromal and luminal tissue fractions [22].

The MR signal model for hybrid-multidimensional MRI is [22]:

$$S(b,TE) = S_0 \cdot [f_L \exp(-bD_L) \exp\left(-\frac{TE}{T_{2L}}\right) + f_S \exp(-bD_S) \exp\left(-\frac{TE}{T_{2S}}\right) + f_E \exp(-bD_E) \exp\left(-\frac{TE}{T_{2E}}\right)] \quad (2.5)$$

Where f_L represents the luminal tissue fraction, which is assumed to have a long T_2 >200 ms and coupled with high diffusivity. f_S represents the stromal tissue fraction, which is assumed to

have a short T_2>40 ms and coupled with intermediate diffusivity D_S. f_E represents the epithelial tissue fraction, which is assumed to have a short T_2 <70 ms and coupled with low diffusivity D_E.

Since tri-exponential fitting is highly sensitive to noise, the authors proposed to stabilize the model fitting by constraining the range of permitted compartmental D and T_2 according to approximate values previously reported in literature, e.g., measurements from high-field strength MR microscopy of formalin fixed prostate specimens [24]. To maximize available in vivo prostate MRI SNR for maintaining model fitting quality, an endorectal coil was used along with a phased array body coil for imaging in the original studies [22] . The SNR feasibility of non-endorectal coil imaging using the hybrid-multidimensional MRI sequence is a topic of ongoing investigation.

2.5.5 Summary of Existing Prostate Microstructure MRI Techniques

Figure 2.7 summarized the existing multi-component signals models for prostate microstructure mapping. The existing methods generally can be categorized into primarily diffusion-based multi-component signal models and primarily T_2-based multi-component signal models, which relied on one dimensional contrast encodings using either b-values (including diffusion time) or echo time (TE). Recently, combined diffusion and T_2 joint modeling strategies have emerged to better utilize the complementary information of both contrast mechanisms for probing prostate microstructure. In this thesis, I approached joint T_2 and D modeling of prostate MRI signals using a continuous spectral based modeling method called diffusion-relaxation correlation spectrum imaging (DR-CSI) [32], which has the unique advantages of not requiring assumptions of the number of tissue compartments and compartment-specific T_2 and D properties; this is a distinct difference compared to existing biophysical compartment models for joint T_2 and D modeling of prostate microstructure

[22]. The specific investigations conducted in this area are detailed in **chapter 5** and **chapter 6** of this thesis.

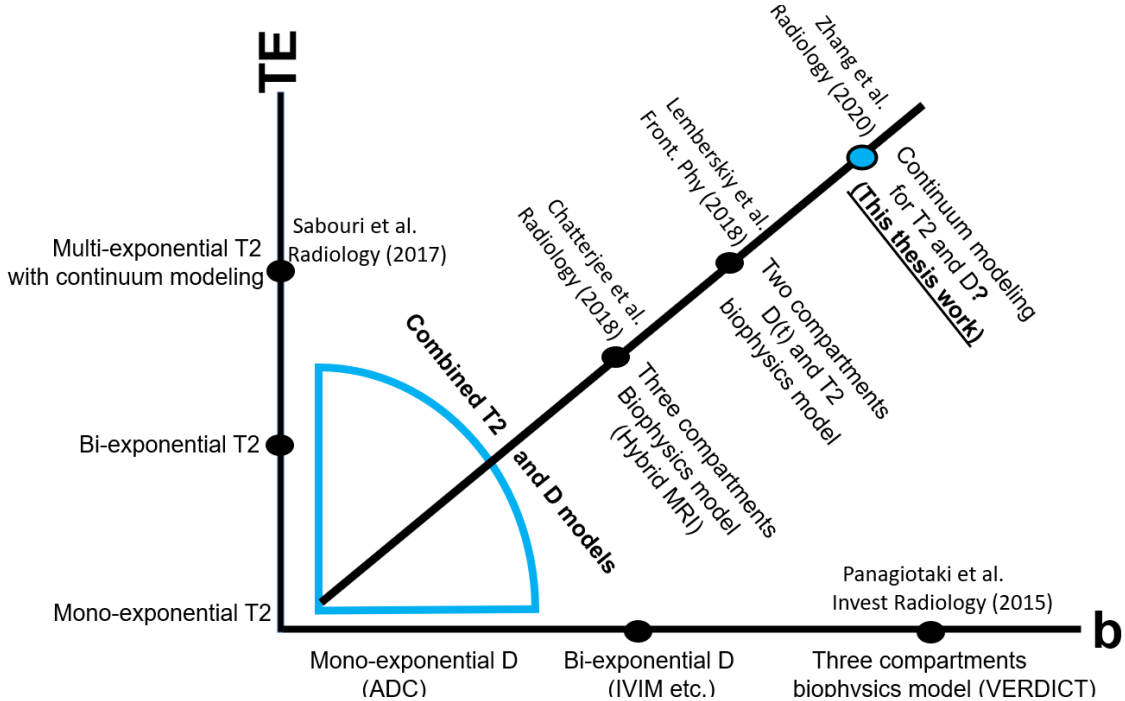

Figure 2.7. Summary of the past works in prostate microstructure MRI techniques and the relationship of this thesis work to existing literature.

2.6 Multi-Dimensional Diffusion-Relaxation Correlation MRI for Inference and Spatial Mapping of Tissue Microstructure and Microenvironment

2.6.1 Continuum Modeling Framework

As reviewed in the previous section, multi-component signal modeling using a pre-determined number of tissue compartments informed by biophysical prior knowledge has been a popular approach for tissue microstructure mapping, including in the prostate. However, this approach faces limitations as it required pre-specifications of many key model parameters (e.g., the number

of tissue compartments and compartment-specific T_2 and diffusivity values from literature) that can have substantial impact on the accuracy and interpretation of estimated tissue microstructure parameters.

Thus, a more flexible tissue microstructure mapping framework that can in principle accommodate an arbitrary number of microscopic tissue compartments without the need of pre-constraining the range of MR properties of each tissue compartment has the potential to further improve MRI-based microstructure mapping with reduced risk of model-induced bias, including for the prostate.

The Laplace nuclear magnetic resonance (NMR) framework, first developed in 1982, provided such a theoretical framework that expressed the MR signal containing heterogeneous tissue compartments as the summation of a continuous distribution of exponential decay functions parameterized by MR parameters such as relaxation time (T_1, T_2) or diffusivity (D) [74].

For example, consider a one-dimensional (1D) T_2 relaxation time-based Laplace NMR experiment acquired with a spin-echo sequence. The observed MR signal from a voxel is expressed as:

$$S(TE) = S_0 \int w(T_2) exp\left(-\frac{TE}{T_2}\right) dT_2 = L\,[w(T_2)] \tag{2.6}$$

Where $w(T_2)$ represents a continuous distribution of T_2 relaxation time parameters to be estimated, and L represents the Laplace transform. In the Laplace NMR framework, $w(T_2)$ is often referred as the T_2 relaxation time spectra of the sample [74].

In analogy to MR spectroscopy, which aims to estimate the resonance frequency spectra of the sample to resolve its chemical compositions [75], the estimated MR property spectra obtained

through Laplace NMR provides information about the distribution of underlying tissue microenvironments labeled by their distinct MR spectral parameters [75].

The number of spectral peaks resolved in the estimated continuous T_2 spectra are expected to correspond to the number of tissue compartments with distinct compartmental T_2 relaxation times, while the location of the peaks reflect the measured compartmental relaxation time properties of underlying compartments [75]. In this theoretical framework, neither the number of tissue compartments nor the MR properties of the compartments are needed as they can be naturally extracted from the estimated MR spectra as part of the measurements.

To estimate the tissue compartment fractions, e.g., for the signal component (A) resolved in T_2 spectra, spectral integration can be performed followed by normalization.

$$f_A = \frac{\int_{\textbf{Area under peak A}} w(T_2) dT_2}{\int_{\textbf{entire } \boldsymbol{T_2} \textbf{ range}} w(T_2) dT_2} \tag{2.7}$$

2.6.2 Inverse Laplace Transform: An Ill-Posed Inverse Problem

The inverse problem of estimating the continuous distribution of underlying MRI properties in the Laplace framework by fitting the observed MR signals is called the inverse Laplace transform (ILT), and for 1D spectra estimation, it is often termed 1D ILT [76] .

This inversion problem is a classical ill-posed mathematical problem, which means the solution is highly unstable and very sensitive to noise perturbation [76]. To stabilize the solution, regularization strategies were required to improve the precision of the solution. One standard constraint for ILT for MR-based microstructure mapping is a non-negativity constraint for the

estimated parameter spectra, as physically a positive or zero signal fraction from underlying tissue compartments is expected [27]. This also motivated the most widely used non-negative least squares (NNLS) algorithm for solving ILT [76].

Another challenge associated with estimating the parameter spectra is the requirement of collecting a large number of measurements in the encoding space. This requirement comes from the fact that the spectra need be discretized with a sufficient number of dictionary entries to reflect the continuous nature of the underlying tissue parameter distribution. This substantially increases the number of unknowns in the model equations that need to be balanced with substantially more signal measurements (on the order of 100 in Laplace NMR literature [75]).

A third challenge of inverse Laplace transform is that when the sample contains tissue compartments with similar MR properties, e.g., similar compartmental T_2 or T_1, it became extremely hard to separate the compartments through the ID ILT inversion due to the substantial overlap in spectral peaks corresponding to the two compartments [75]. In this situation, an extremely large number of dense samples in the signal encoding space and high SNR are needed to enable higher spectral resolution to resolve the overlap in spectral parameters [77], which would still be challenging and impractical.

2.6.3 Improved Inversion using Multidimensional Contrast Encoding

The multi-dimensional DR-CSI approaches recently developed for spatial mapping of tissue microstructure can find their roots in the single-voxel multi-dimensional diffusion-relaxation correlation spectroscopy (DR-COSY) methods first developed by Sir Paul Callaghan et al [75].

DR-COSY was developed based on the observation that while the separation of tissue compartments with a single MR contrast mechanism (T_2 only or diffusivity only) has fundamental

limitations in terms of spectral peak overlap, this ambiguity can be greatly improved by estimating two-dimensional correlation spectra of different MR properties (e.g., diffusivity correlated with T_2 for resolving signal components in DR-COSY). This can be achieved by performing a two-dimensional contrast encoding experiment that simultaneously encodes diffusion sensitivity and T_2 relaxation time sensitivity into the MR signal [75]. For example, this can be achieved through acquiring MRI signals with different degrees of T_2 and diffusion weighting by sampling on a rectangular grid of signals *S(TE,b)* at different combinations of echo time (TE) and b-value, as shown in **Figure 2.8**.

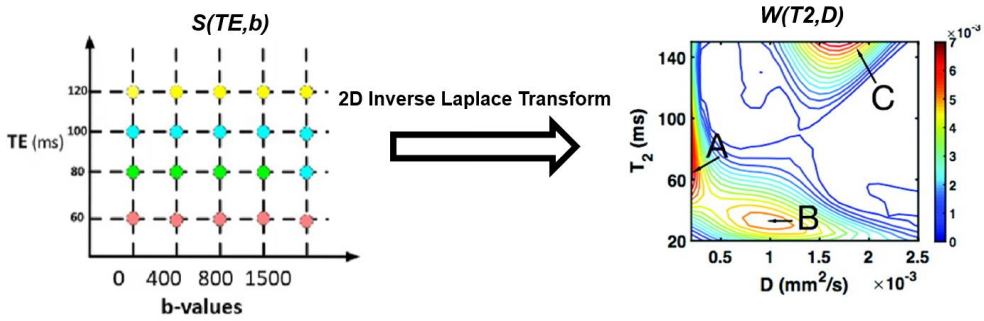

Figure 2.8. Illustration for multidimensional contrast encoding acquisition scheme and 2D T2 and diffusivity correlation spectrum reconstruction for DR-COSY and DR-CSI.

This multidimensional contrast encoding scheme permits the reconstruction of the 2D T_2 and diffusivity correlation spectrum *w(T2,D)* of the sample.

The MR signal equation for DR-COSY (and later DR-CSI) using a spin-echo diffusion-weighted MR sequence is [75]:

$$S(TE,b) = S_0 \int w(T_2,D) exp\left(-\frac{TE}{T_2}\right) exp(-bD)\, dT_2 dD = L_{2D}\,[w(T_2,D)] \qquad (2.8)$$

Where $w(T_2, D)$ represents the 2D correlation spectra of T_2 relaxation and D, and L_{2D} represent the 2D Laplace transform [75].

2.6.4 Improved Inversion using Spatial Correlation Constraints in DR-CSI

Inspired by the original single-voxel DR-COSY method, where multi-dimensional contrast encoding improved microstructure resolution, Kim D et al., further made the new observation that in an imaging experiment, it will yield many T_2-D spectra from hundreds or thousands of voxels, which are expected to exhibit some degree of correlation with each other, e.g., due to spatial proximity [32]. This implied that the estimation of T_2-D spectra may not need to be independently performed in a voxel-by-voxel manner where only limited signal measurements corresponding to each specific voxel were used for estimating its spectrum. Instead, measurements between adjacent voxels can be potentially shared to effectively boost the number of measurements for improving the condition of inverting 2D ILT [27].

Based on the above theoretical observations, the DR-CSI approach used the additional prior knowledge that the T_2-D spectra at spatially adjacent voxel locations are expected to vary smoothly due to the inherent correlation in spatial structure embedded in an imaging experiment [32]. This knowledge was combined with the classical non-negativity constraint for solving the voxel-wise 2D inverse Laplace transform problem. Mathematically, this is expressed as solving the following optimization problem [32]:

$$w = \text{argmin } \|S - Lw\|_F^2 + \lambda\, TV_{xy}(w), \text{subject to } w \geq 0 \qquad (2.9)$$

$$S(x, y, TE, b) = \iint w(x, y, T_2, D) \exp\left(-\frac{TE}{T_2}\right) \exp(-bD) dT_2 dD = Lw \qquad (2.10)$$

where *S(x,y,TE,b)* represents the voxel-wise measured signals with each TE-b encoding, *w(x,y,T_2,D)* represents the voxel-wise T_2-D spectra to be reconstructed, and *L* represents the Laplace Transform. To solve for *w(x,y,T_2,D)*, non-negativity (i.e., *w(x,y,T_2,D)*$\geq$0) and spatial total variation (TV_{xy}), constraints were applied [32]. λ is a regularization parameter adjusting how strong the spatial total variation constraint should be enforced relative to the data consistency constraint. The above optimization is convex and can be solved globally from arbitrary initializations [32]. An efficient variable splitting and alternative direction method of multiplier (ADMM) algorithm can be adopted to solve the above numerical problem [32].

For each resolved spectral peak on the voxel-wise T_2-D spectra, its spectral signal component fractions (e.g. f_A, f_B, f_C, if three peaks A, B, C exist on T_2-D spectra) can be calculated by integrating each spectral peak on the voxel-wise or region-averaged T_2-D spectra followed by normalization.

For example, to calculate f_A:

$$f_A(x,y) = \frac{\int_{\textbf{Area under peak A}} w(x,y,T_2,D)\,dT_2\,dD}{\int_{\textbf{entire } (\boldsymbol{T_2}-\textbf{D}) \textbf{ space}} w(x,y,T_2,D)\,dT_2\,dD} \tag{2.11}$$

Chapter 3 **Prostate Diffusion MRI with Minimal Echo Time Using Eddy Current-Nulled Convex Optimized Diffusion Encoding**

3.1 **Introduction**

Diffusion weighted MRI (DWI) is one of the key components of multi-parametric (mp) MRI for diagnosis of prostate cancer (PCa) [68], and analysis of DWI signals, such as apparent diffusion coefficient (ADC) mapping can provide tissue specific physiologic and microstructural information that has shown value for characterization of PCa aggressiveness [68,4,78]. The most widely used encoding schemes for prostate DWI are monopolar spin echo (MONO) and twice-refocused bipolar spin echo (BIPOLAR) [5,6]. MONO has a short echo time (TE), but suffers from eddy current induced distortion artifacts [6,52,79]; BIPOLAR uses a modified gradient design and a second refocusing pulse to mitigate eddy current fields that are produced by each gradient lobe at the end of diffusion encoding, but at a cost of substantially increased TE (and lower SNR) compared to MONO [6,54,80]. In general, both a short TE and reduced eddy current-induced distortion artifacts are desired to maintain sufficient SNR (or improve acquisition speed) and minimize overall image distortion in prostate DWI [8,81,82].

However, these two desired features are not achievable at the same time using current encoding schemes (MONO or BIPOLAR). Therefore, optimization of the diffusion encoding scheme to meet both needs is desired for prostate DWI. Furthermore, improving the spatial resolution of prostate DWI may improve its performance for PCa diagnosis with finer depiction of prostate tissues compared to standard clinical prostate DWI protocols, which typically use single-shot echo planar imaging (EPI) readouts and have in-plane resolution limited to 1.6x1.6~2x2 mm^2 [83,10]. However, the temporal footprint of the diffusion encoding gradients and the associated substantial

TE increase for higher-resolution DWI protocols using longer EPI readout durations results in additional T_2 decay that reduces SNR [14,28,64].

Recently, the Convex Optimized Diffusion Encoding (CODE) framework for designing diffusion encoding gradient waveforms was modified to support eddy current nulling (ENCODE), which suppresses eddy current-induced distortion artifacts and minimizes the TE for a given targeted b-value and EPI readout duration [28,64]. It has been shown in a brain DWI protocol that ENCODE gradient waveforms have a TE similar to MONO while reducing eddy current effects to a level consistent with BIPOLAR [28]. The advantages of ENCODE could benefit prostate DWI by producing diffusion gradient waveforms that minimize TE (and improve SNR) for a range of sequence parameters, including higher spatial resolution and longer EPI readouts.

The purpose of this study was to design and evaluate new ENCODE prostate DWI in comparison to standard encoding schemes (MONO and BIPOLAR), in terms of eddy current artifact reduction, TE, SNR, ADC, and diagnostic image quality and overall geometric distortion.

3.2 **Methods**

3.2.1 Study Population

In this Health Insurance Portability and Accountability Act of 1996 (HIPAA) compliant, Institutional Review Board (IRB) and biosafety committee approved study. All subjects provided signed statements of informed consent prior to research procedures. *Ex vivo* MRI of a prostate specimen was obtained from a PCa patient who underwent robotic-assisted radical prostatectomy. From June 2017 to May 2019, we scanned 10 healthy male subjects (age: 27±3 years), along with 5 male patients (age: 62±7 years) undergoing clinically indicated prostate MRI for pre-biopsy planning to evaluate ENCODE prostate DWI. From June 2021 to March 2022, we scanned a

separate cohort of 36 patients (age: 55±6 years) with clinical suspicion of PCa undergoing pre-biopsy or pre-surgery prostate MRI to further investigate a combined reduced field-of-view (rFOV) with ENCODE prostate DWI technique for reducing overall geometric distortion from both eddy current and susceptibility effects.

3.2.2 Prostate DWI Protocols

For evaluation of standard FOV prostate DWI using MONO, BIPOLAR and ENCODE with single-shot spin-echo EPI acquisition, imaging experiments were performed on a 3T MRI scanner (Prisma, Siemens, Erlangen, Germany) with a high-performance gradient system (maximum gradient amplitude G_{max} = 80 mT/m and maximum slew rate SR_{max} = 200 T/m/s). For evaluation of rFOV ENCODE prostate DWI versus standard FOV BIPOLAR DWI, imaging experiments were performed on two MRI scanners (Prisma or Skyra, Siemens, Erlangen, Germany) with a high-performance (G_{max} = 80 mT/m and SR_{max} = 200 T/m/s) and standard-performance gradient system (G_{max} = 45 mT/m and SR_{max} = 200 T/m/s), respectively. Standard FOV prostate DWI were first evaluated using clinical standard parameters, including 1.6x1.6 mm^2 in-plane resolution and partial Fourier (pF) factor 6/8 [84]. In addition, two higher-resolution protocols were evaluated: 1) in-plane resolution increased to 1.0x1.0 mm^2 with pF=6/8, and 2) in-plane resolution 1.6x1.6 mm^2 with the pF factor set to 1 (i.e., pF=off). Partial Fourier acquisitions and reconstructions result in a broadened imaging point spread function (PSF) in the phase encoding direction that decreases the effective resolution of the image [85]. Both approaches, either increasing matrix resolution or turning off pF, would result in increased EPI duration, as characterized by the time to echo (T_{EPI}) duration (**Figure 3.1**). Detailed sequence and imaging parameters for standard FOV Prostate DWI and rFOV prostate DWI are listed in **Table 3.1** and **Table 3.2**, respectively. All protocols have the

same scan time using interleaved 2D multi-slice acquisition mode with TR=4800 ms. The b-values for all sequences were calculated using:

$$b = \gamma^2 \int_0^T \left(\int_0^t G(\tau)d\tau\right)^2 dt \quad (3.1)$$

where γ is the gyromagnetic ratio of hydrogen and T represents the end time point of the diffusion encoding waveform *G*.

3.2.3 Theoretical Comparisons

Eddy Current Effects

The ENCODE gradient waveforms for the evaluated prostate DWI protocols (**Table 3.1**) were designed to null eddy current fields with decay time constant λ_{null} = 80 ms [28]. The BIPOLAR and MONO diffusion encoding gradient waveforms for comparison were also designed using the same pulse sequence parameters and hardware constraints as ENCODE. We used the eddy current model [53]:

$$EC = \frac{dG}{dt} * e^{-\frac{t}{\lambda}} \quad (3.2)$$

where *G* is the applied gradient waveform, λ is the eddy current time constant, and * denotes the convolution operator. This convolution relationship models eddy current magnitudes as being affected by both the temporal evolutions of gradient derivative functions and exponential decay functions. The dominant time constant was measured to be 80 ms on the MRI system used in this study [28]. The approximated eddy current magnitude from **Eqn. 3.2** (EC, arbitrary units) of each encoding gradient waveform at the end of diffusion encoding were computed and compared for each clinical standard and higher-resolution protocol.

TE and Expected Signal

TE and TE differences (ΔTE) between MONO, BIPOLAR and ENCODE were evaluated for clinical standard and higher-resolution protocols. Expected signal amplitudes were evaluated based on the spin-echo DWI signal model $S=M_0 \bullet \exp(-TE/T_2) \bullet \exp(-bD)$, where b is the maximum applied b-value (800 s/mm^2), TE is the minimum TE for each diffusion encoding scheme considering b-value and EPI time to echo (T_{EPI}), T_2 is the transverse relaxation time, and D is the apparent diffusion coefficient in prostate tissues. Expected percentage signal differences (ΔS) between ENCODE and reference techniques (MONO or BIPOLAR) were calculated as:

$$\Delta S_{ENCODE,REF} = \frac{S_{ENCODE} - S_{REF}}{S_{REF}} = (\exp\left(-\frac{\Delta TE_{REF}}{T_2}\right) - 1) \cdot 100\% \quad (3.3)$$

ΔS only depends on TE differences between sequences (ΔTE) and T_2 of prostate tissue. We assumed normal prostate peripheral zone (PZ) $T_{2,PZ}$ = 120 ms and normal prostate transitional zone (TZ) $T_{2,TZ}$ = 80 ms at 3T [86]. Expected percentage signals differences (ΔS) in normal PZ and TZ tissues were computed for clinical standard and higher-resolution protocols.

3.2.4 Phantom Imaging to Assess Eddy Current-Induced Artifacts

Phantom experiments were performed to compare eddy current-induced image distortion artifacts between diffusion encoding schemes using standard and higher-resolution prostate DWI protocols. A National Institute of Standards and Technology (NIST) diffusion phantom containing multiple vials [87], was imaged at 3T with a 20-channel head coil. The phantom was placed in the head coil with vials pointing along the main magnetic field direction. DWI scans were acquired with b=0, 100, 400, 800 s/mm^2 along three diffusion encoding directions (3 scan trace mode) for standard

and higher-resolution protocols (**Table 3.1**). All acquisition parameters were matched and DWI scans were performed with the minimum TE for each diffusion encoding scheme.

Eddy current-induced distortion artifacts were evaluated for each diffusion encoding scheme by measuring the pixel-wise coefficients of variation (CoV) across diffusivity maps of each diffusion direction [81]. The mean CoV within edge voxels (CoV_{edge}) at the tube-water interfaces were measured, and the global mean CoV_{edge} across all tubes was computed and compared between the diffusion encoding schemes.

Protocol*	FOV (mm^2)	Voxel size (mm^2)	pF factor	T_{EPI} (ms)	b values (s/mm^2)	Diffusion Directions	TE (ms)		
							MONO	BIPOLAR	ENCODE
Standard	260×216	1.6×1.6	6/8	17	0,100, 400, 800	3 Scan Trace	57	77	63
Higher-Resolution		1.6×1.6	Off	28			77	102	67
		1.0×1.0	6/8	24			70	98	65

Table 3.1:
Summary of sequence and imaging parameters used in phantom, *ex vivo* prostate, and *in vivo* prostate DWI. FOV: field of view. pF: partial Fourier. T_{EPI}: time to echo for echo-planar readout. TE: echo time. *Common parameters for all protocols included: slice thickness = 3.6 mm, 20 slices, repetition time (TR) = 4800 ms, parallel imaging factor = 2, number of averages = 7 for all b values, and scan time = 5 min 53 s.

3.2.5 Ex Vivo Prostate Specimen Imaging

An *ex vivo* prostate specimen was imaged to evaluate MONO, BIPOLAR, and ENCODE prostate DWI in the absence of motion and with minimized susceptibility artifacts. A fresh whole prostate specimen was obtained from a PCa patient immediately after robotic-assisted radical prostatectomy. The prostate specimen was placed inside a patient-specific 3D-printed mold, then positioned inside a plastic container. The mold had a mesh interior that allowed fluid to permeate. The mold and specimen were then immersed in a perflurocarbon solution (Fomblin, Solvay) to

match the magnetic susceptibility of prostate tissue and suppress susceptibility artifacts while generating zero background signal. The whole container was then scanned using a 15-channel knee coil in a position corresponding to feet-first supine MRI [88]. MONO, BIPOLAR and ENCODE prostate DWI scans were acquired using standard and higher-resolution protocols with seven repetitions.

SNR and ADC Evaluations

SNR maps were calculated from the seven repetitions of the b=800 s/mm^2 images for MONO, BIPOLAR, and ENCODE (voxel-wise mean signal divided by standard deviation across repetitions). ADC maps were reconstructed for all acquisitions using linear least-squares fitting. The mean SNR and mean ADC were sampled from 12 uniformly spaced circular regions of interest (ROIs, 24 mm^2 each), in the prostate specimen for comparison between MONO, BIPOLAR and ENCODE for both clinical standard and higher-resolution protocols. Linear regression was performed to compare the correlation of ADC between different diffusion encoding methods for clinical standard and higher-resolution protocols.

Eddy Current-Induced Distortion

Directionally dependent eddy current induced distortion artifacts were qualitatively compared by overlapping the prostate boundaries on DWI (b=800 s/mm^2) acquired for each diffusion encoding direction (X, Y, Z) for MONO, BIPOLAR and ENCODE. In *ex vivo* MRI experiments, background signal was zero and enabled direct segmentation of prostate boundaries on DWI through manual tracing (**Figure 3.3)**. Inconsistencies in the prostate boundary across diffusion directions on DWI were attributed to eddy current effects.

3.2.6 In Vivo Imaging in Healthy Subjects

To evaluate MONO, BIPOLAR and ENCODE prostate DWI *in vivo*, 10 healthy male subjects (27±3 years old) were scanned at 3T using 18-channel body and spine array coils.

SNR and ADC Evaluations

SNR maps were computed from the seven repetitions of the b=800 s/mm^2 images (voxel-wise mean signal divided by standard deviation across repetitions) for MONO, BIPOLAR and ENCODE. ADC maps were reconstructed for MONO, BIPOLAR and ENCODE using linear least-squares fitting. For ADC and SNR evaluation, the prostate was manually segmented into peripheral zone (PZ) and transition zone (TZ) on T_2-weighted MRI by a researcher, and zonal ROIs were mapped into DWI. The mean SNR and mean ADC in prostate TZ and PZ were compared across MONO, BIPOLAR and ENCODE in 10 healthy subjects for clinical standard protocol and higher-resolution protocols.

3.2.7 In Vivo Prostate Imaging in a Cohort of PCa Patients

A pilot evaluation of PCa patients (N=5 males, 62±7 years old) undergoing clinically indicated prostate mp-MRI prior to biopsy were recruited for this study. Scans were acquired at 3 T using the body and spine array coils (without endorectal coil). The protocol included a clinical standard prostate DWI sequence using BIPOLAR encoding with standard resolution (1.6x1.6 mm^2, pF = 6/8). In addition, we acquired a higher-resolution ENCODE prostate DWI sequence (1.6x1.6 mm^2, pF = off) that had minimum echo time (TE = 67 ms vs. TE = 77 ms for clinical BIPOLAR DWI),

while other imaging parameters were identical to the clinical standard prostate BIPOLAR DWI sequence (**Table 3.1**).

Diagnostic Image Quality Evaluation

Three readers, an expert abdominal radiologist (S.R., 25 years of experience) and two abdominal radiology fellows (S.A. and M.H., 2-4 years of experience), independently evaluated the diagnostic image quality of ENCODE and clinical BIPOLAR diffusion-weighted images with b-value=400 s/mm^2 and ADC maps. Images were scored on a scale of 1-4 for six categories: prostate TZ signal, prostate PZ signal, muscle/fat signal, rectum signal, overall image quality for DWI, and lesion conspicuity on ADC map. These categories were chosen by the expert radiologist to reflect the ability of DWI to depict prostate zonal anatomy and surrounding tissues of interests (muscle/fat and rectum) for the clinical diagnosis of PCa. The criteria were: 1 – poor image quality, 2 – moderate image quality, 3 – good image quality, and 4 – excellent image quality. The images were displayed to the readers blinded to any information identifying the sequence and in a randomized order. The image quality scores in each category were reported for each patient, and the medians for all patients were reported. The intra-class correlation coefficient (ICC) [89,7] was computed to evaluate the agreement in the ratings for the six image quality categories between readers 1 and 2, readers 2 and 3, and readers 1 and 3. The mean of the ICCs were computed as an indicator of overall inter-reader agreement among all three readers.

ADC Evaluation

The expert radiologist identified and contoured suspected cancerous lesions according to the prostate imaging - reporting and data system version 2 (PI-RADS v2) criteria [90] on anatomical

T_2-weighted turbo spin-echo images and clinical DWI (BIPOLAR) and the ADC map [91]. In addition, benign PZ and TZ ROIs were also drawn on clinical DWI. The ROIs were transferred to the ENCODE DWI and ADC maps. ENCODE ADC was compared with BIPOLAR ADC in PCa, benign PZ, and benign TZ ROIs.

3.2.8 Combining ENCODE with rFOV to Reduce Overall Prostate Geometric Distortion

rFOV-ENCODE Prostate DWI Protocol

The reduced Field-of-View (rFOV)-ENCODE prostate DWI protocol was designed to have the same scan time as clinical standard resolution DWI used in our institution, with matched diffusion parameters including b-values, diffusion directions, and repetitions for averages (**Table 3.2**).

The rFOV-ENCODE sequence used outer volume suppression RF pulses [29] to reduce the phase encoding (PE) field-of-view, and enabled encoding of an image matrix with higher in-plane spatial resolution while reducing B_0 inhomogeneity-induced geometric distortion [60,92]. The achievable reduction in PE-FOV depended on the peripheral nerve stimulation limits of each scanner; the rFOV-ENCODE protocol achieved 40% and 35% reduction of PE-FOV on the Prisma and Skyra systems, respectively.

Protocol parameter	rFOV-ENCODE	Standard BIPOLAR
Echo time (TE) (ms)	**63/79***[1]	80
b value (s/mm^2)	0, 100,400, 800	
Repetition time (TR) (ms)	4800	
Field of view (mm^2)	220x**124**/250x**144***[2]	260x216
Acquisition Resolution (mm^2)	1.6 x 1.6	1.6x2.2
Slice thickness (mm)	3.6	
Diffusion directions	3-scan trace	
Parallel imaging factor	2	
Partial Fourier factor	6/8	
Phase encoding direction	A-P	
Number of slices	16-20	
Averages	7	
Scan time	5 min 58 s	

Table 3.2:
Sequence parameters for rFOV-ENCODE prostate diffusion MRI and clinical standard BIPOLAR diffusion MRI. *Note: [1] The minimum TE achieved by ENCODE waveform depends on gradient hardware limits. 63/79 ms represents the TE achieved on 3T Prisma (G_{max}=76 mT/ms), and 3T Skyra (G_{max}=40 mT/ms) systems, respectively. [2] The minimal achievable phase-encoding FOV on 3T Prisma and 3T Skyra were 125 and 144 mm^2 respectively due to different peripheral nerve stimulation limits of each scanner.

Experiments

We acquired rFOV-ENCODE DWI and standard BIPOLAR DWI in 36 patients with clinical suspicion of prostate cancer at 3 T (Prisma or Skyra; Siemens) with body array coils, and performed qualitative and quantitative geometric distortion analysis within this cohort of patients.

Quantitative Prostate Geometric Distortion Comparison

For quantitative evaluation of geometric distortion, a researcher, supervised by a radiologist, contoured the prostate on each DWI sequence at b=100 s/mm^2 and on reference T2W TSE MRI. Dice's similarity coefficient (DSC; 0 to 1) of the prostate contours between each DWI sequence and T2W MRI was used to quantify geometric fidelity.

Qualitative Radiological Image Quality Assessment of Geometric Distortion

For qualitative evaluation, two expert radiologists (R1, R2) independently scored rFOV-ENCODE and standard full-FOV BIPOLAR (ST) DWI in a blinded randomized fashion for prostate geometric distortion on a 5-point scale (1: none, 2: minimal, 3: mild, 4: moderate, 5: severe), and overall diagnostic image quality (1: excellent, 2: good, 3: moderate, 4: compromised and 5: poor image quality). Differences in the scores were assessed by two-sided Wilcoxon signed-rank tests.

3.2.9 Statistical Analysis

Statistical analysis was performed in MATLAB (MathWorks, Natick, MA). For the *ex vivo* prostate specimen and *in vivo* healthy subject prostate imaging experiments, the Kruskal-Wallis test was used first to assess the differences in SNR or ADC among MONO, BIPOLAR and ENCODE prostate DWI. If the Kruskal-Wallis test yielded significant differences, pair-wise comparisons were made between groups (e.g. ENCODE vs. BIPOLAR) using Wilcoxon signed-rank tests. For the *ex vivo* prostate specimen imaging experiment, linear correlation and Bland-Altman analysis were performed to evaluate the strength of a linear correlation and mean differences (bias) between MONO, BIPOLAR and ENCODE. Linear correlation analysis yields an equation for linear regression between two compared techniques and the slope and intercept

were determined. The coefficient of determination (R^2) was used to evaluate the strength of the linear correlation. Bland-Altman analysis was used to calculate the mean difference (MD) between two techniques, and the 95% limits of agreement (LoA) were reported as the deviation from the mean difference by ±1.96 standard deviation (SD). For all statistical comparisons, a *P* value of <0.05 was considered significant. For the analysis of inter-reader agreement, ICC values of 0.75-1 were considered excellent, 0.6-0.74 considered good, 0.4-0.59 considered fair, and less than 0.4 considered poor [89,7].

3.3 **Results**

3.3.1 Theoretical Comparisons

Eddy Current Effects

Estimates based on **Eqn 3.2** show that MONO has the largest residual eddy current effects at the end of diffusion encoding. BIPOLAR and ENCODE achieved substantial reduction in eddy current effects by more than one order of magnitude for the standard protocol (1.6x1.6 mm^2 and pF=6/8: EC_{MONO}=1.14, $EC_{BIPOLAR}$=2.71e-2, EC_{ENCODE}=1.36e-3) and higher-resolution protocols (1.6x1.6 mm^2 and pF=off: EC_{MONO}=0.93, $EC_{BIPOLAR}$=1.94e-2, EC_{ENCODE}=2.78e-3; 1.0x1.0mm^2 and pF=6/8: EC_{MONO}=0.97, $EC_{BIPOLAR}$=2.02e-2, EC_{ENCODE}=6.5e-6).

TE and Expected Signal

By optimizing the temporal footprint of the diffusion encoding gradients to achieve the desired diffusion weighting (b-value) and eddy current compensation, ENCODE shortened the associated TE substantially compared to BIPOLAR and achieved similar or even shorter TE compared to MONO for a range of protocol parameters (**Figure 3.1**). The advantage of ENCODE in shortening

TE compared to BIPOLAR and MONO is more pronounced for protocols with longer EPI time to echo (T_{EPI}).

Table 3.3 summarizes the TE differences (ΔTE) and expected percent signal differences (ΔS) in prostate TZ and PZ using MONO, BIPOLAR, and ENCODE for standard and higher-resolution imaging protocols. Reduction in TE contributed to enhancement in the expected signal using ENCODE compared to BIPOLAR for the higher resolution imaging protocol with longer T_{EPI}.

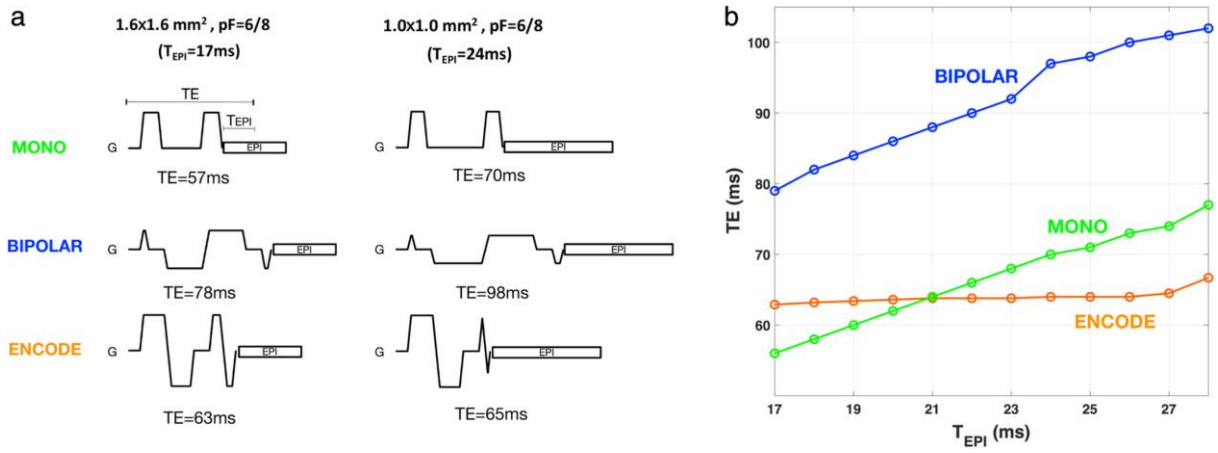

Figure 3.1. ENCODE prostate DWI sequence. **(a)** Sequence diagrams of MONO, BIPOLAR, and ENCODE DWI for clinical standard (in-plane resolution = 1.6 × 1.6 mm^2, partial Fourier factor [pF] = 6/8, EPI time to echo [T_{EPI}] = 17 msec) and higher-resolution (in-plane resolution = 1.0 × 1.0 mm^2, pF = 6/8, T_{EPI} = 24 msec) prostate DWI protocols with b-value of 800 s/mm^2 and using the three-scan trace mode. **(b)** TE dependency of MONO, BIPOLAR, and ENCODE DWI on T_{EPI}.

Protocol	$\Delta TE_{ENCODE,BIPOLAR}$	$\Delta TE_{ENCODE,MONO}$	$\Delta S_{ENCODE,BIPOLAR}$		$\Delta S_{ENCODE,MONO}$	
			PZ	TZ	PZ	TZ
Standard: 1.6 mm, pF: 6/8	-14 ms	+6 ms	12%	19%	-5%	-7%
Higher-resolution: 1.6 mm, pF: off	-35 ms	-10 ms	34%	55%	9%	13%
Higher-resolution: 1.0 mm, pF: 6/8	-33 ms	-5 ms	32%	51%	4%	6%

Table 3.3:

Theoretical echo time (TE) and expected signal levels for MONO, BIPOLAR, and ENCODE DWI for standard and higher-resolution protocols. TE differences (ΔTE) and expected percentage signal differences (ΔS) were reported for prostate peripheral zone (PZ) and transition zone (TZ) tissues. pF: partial Fourier.

3.3.2 Phantom Imaging: Eddy Current-Induced Distortion

CoV maps for MONO, BIPOLAR, and ENCODE for clinical standard and higher-resolution protocols are shown in **Figure 3.2** and the means of CoV_{edge} across all tubes are reported. The high CoV_{edge} for MONO showed the effect of eddy current-induced directionally dependent distortions, which was further increased for higher-resolution protocols (1.0x1.0 mm^2 and pF = 6/8; 1.6x1.6 mm^2 and pF = off). For clinical standard and higher-resolution imaging protocols, CoV_{edge} was consistently reduced by ENCODE and BIPOLAR. These results demonstrate that ENCODE and BIPOLAR had comparable performance in reducing eddy current effects, while eddy current induced distortion artifacts were more evident and severe for MONO.

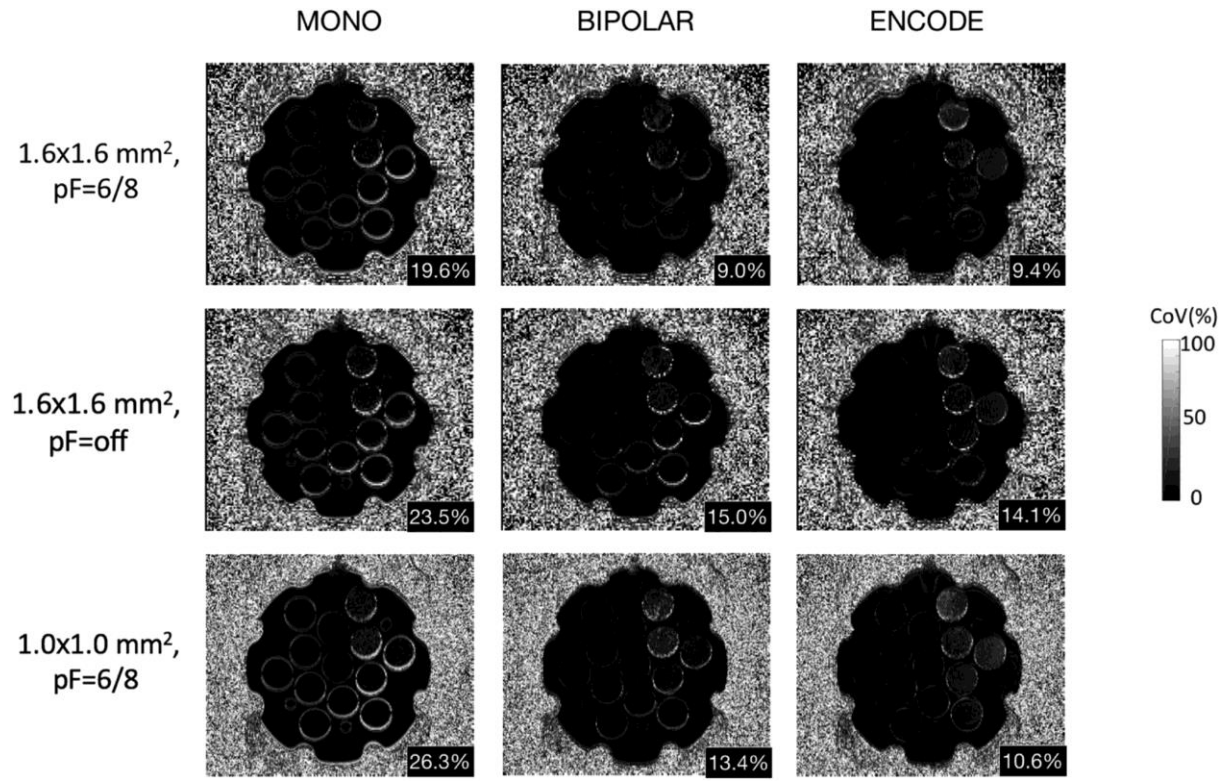

Figure 3.2. Evaluation of eddy current effects in a diffusion phantom. The CoV was measured across ADC maps of three diffusion directions for MONO, BIPOLAR, and ENCODE DWI, using clinical standard and higher-resolution protocols. The CoV maps are shown for each DWI sequence and protocol. The mean CoV within edge voxels (CoV_{edge}) at the tube-water interfaces were measured and the global mean CoV_{edge} across all tubes were reported (in black boxes at the lower right corner of the CoV maps).

3.3.3 Ex vivo Prostate Specimen Imaging

Eddy Current-Induced Distortion

Figure 3.3 shows comparisons of prostate boundary consistency on DWI of b-value=800 s/mm^2 across three diffusion directions for MONO, BIPOLAR, and ENCODE. Inconsistency of prostate boundaries was evident on MONO DWI, while there was minimal discrepancy when using BIPOLAR and ENCODE. These results demonstrate that eddy-current induced distortion artifacts

could lead to unfaithful spatial representation of prostate boundary using MONO DWI, while BIPOLAR and ENCODE effectively reduced this source of distortion.

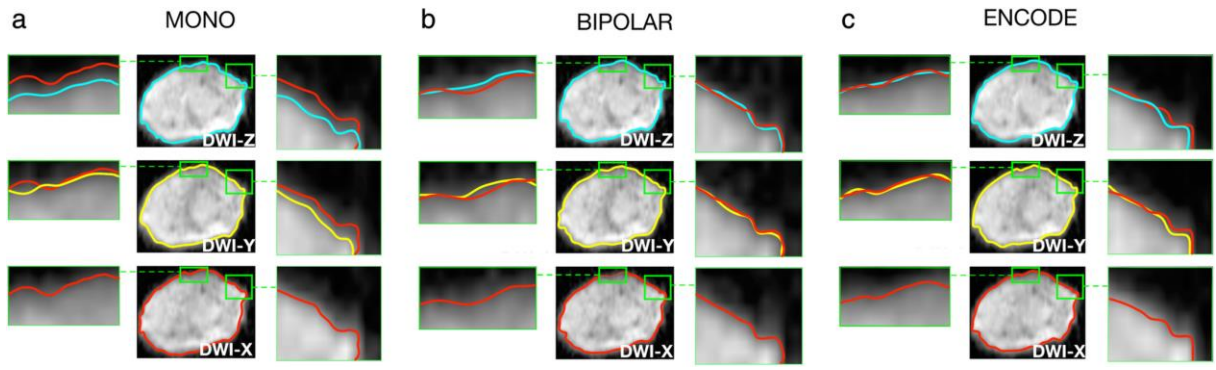

Figure 3.3. Comparison of eddy-current-induced distortion artifacts for DWI in an ex vivo prostate specimen. The prostate boundaries on directional diffusion-weighted MR images (b-value of 800 (mm^2) are delineated in red, yellow, and blue for the X, Y, and Z diffusion encoding directions, respectively. Zoomed-in views are shown for the regions outlined by green boxes. **(a)** Comparison of prostate boundaries on directional DWI for MONO. **(b)** Comparison of prostate boundaries on directional DWI for BIPOLAR. **(c)** Comparison of prostate boundaries on directional DWI for ENCODE.

SNR and ADC Evaluation

Figure 3.4 shows example diffusion weighted images of an *ex vivo* prostate specimen acquired using MONO, BIPOLAR, and ENCODE schemes for clinical standard and higher-resolution imaging protocols. For the clinical standard imaging protocol, ENCODE mean SNR across the 12 ROIs was 16% higher than BIPOLAR (P<0.05) and 11% lower than MONO (P=N.S). For higher-resolution imaging protocols, ENCODE mean SNR across the ROIs was 46% higher than BIPOLAR (P<0.001) and 16% higher than MONO (P<0.05) for 1.6x1.6 mm^2 with pF = off, and 44% higher than BIPOLAR (P<0.001) and 13% higher than MONO (P<0.05) for 1.0x1.0 mm^2 with pF = 6/8 (**Figure 3.4**).

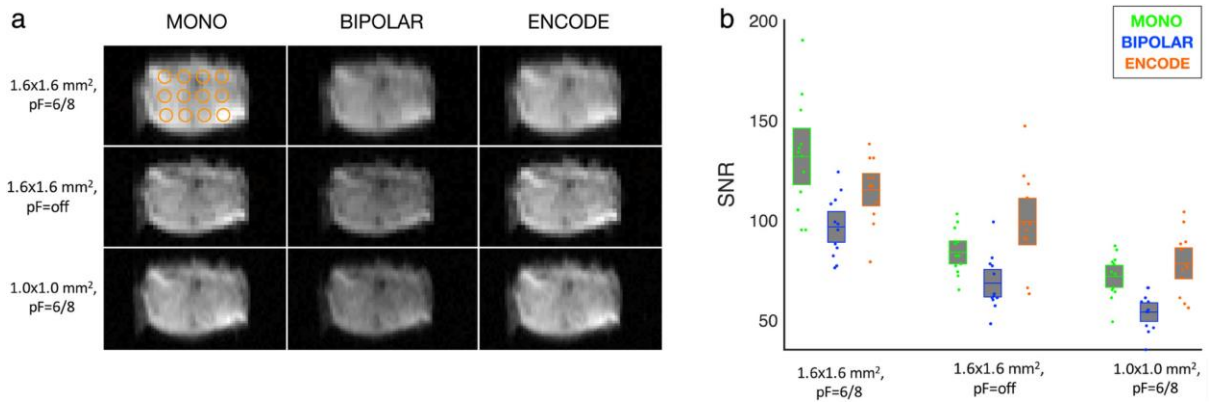

Figure 3.4. Comparison of DWI SNR in an ex vivo prostate specimen. **(a)** Ex vivo prostate DWI (b-value of 800 s/mm^2) acquired using MONO, BIPOLAR, and ENCODE sequences for clinical standard (1.6×1.6 mm^2 with partial Fourier factor [pF] = 6/8) and higher-resolution protocols (1.6×1.6 mm^2 with pF = off and 1.0×1.0 mm^2 with pF = 6/8).The same display window/level was used for all images. **(b)** Boxplots of SNR distributions of MONO, BIPOLAR, and ENCODE DWI for clinical standard and higher-resolution protocols. The regions of interest for measuring SNR are denoted as orange circles on DWI in (a). ENCODE achieved significantly higher SNR than BIPOLAR for all three prostate DWI protocols.

A range of ADC values (400~1200·10^{-6}mm^2/s) were observed within the *ex vivo* prostate specimen (**Figure 3.5a**). MONO, BIPOLAR, and ENCODE ADC values showed significant linear correlation with each other across all protocols (R^2>0.97) (**Figure 3.5b**). Bland-Altman analysis results showed absolute mean differences <50·10^{-6} mm^2/s and absolute limit of agreement <105·10^{-6} mm^2/s when comparing ADC between sequences and across protocols (**Figure 3.5c**). These results demonstrated that ENCODE ADC achieved close agreement with MONO and BIPOLAR in the *ex vivo* prostate specimen.

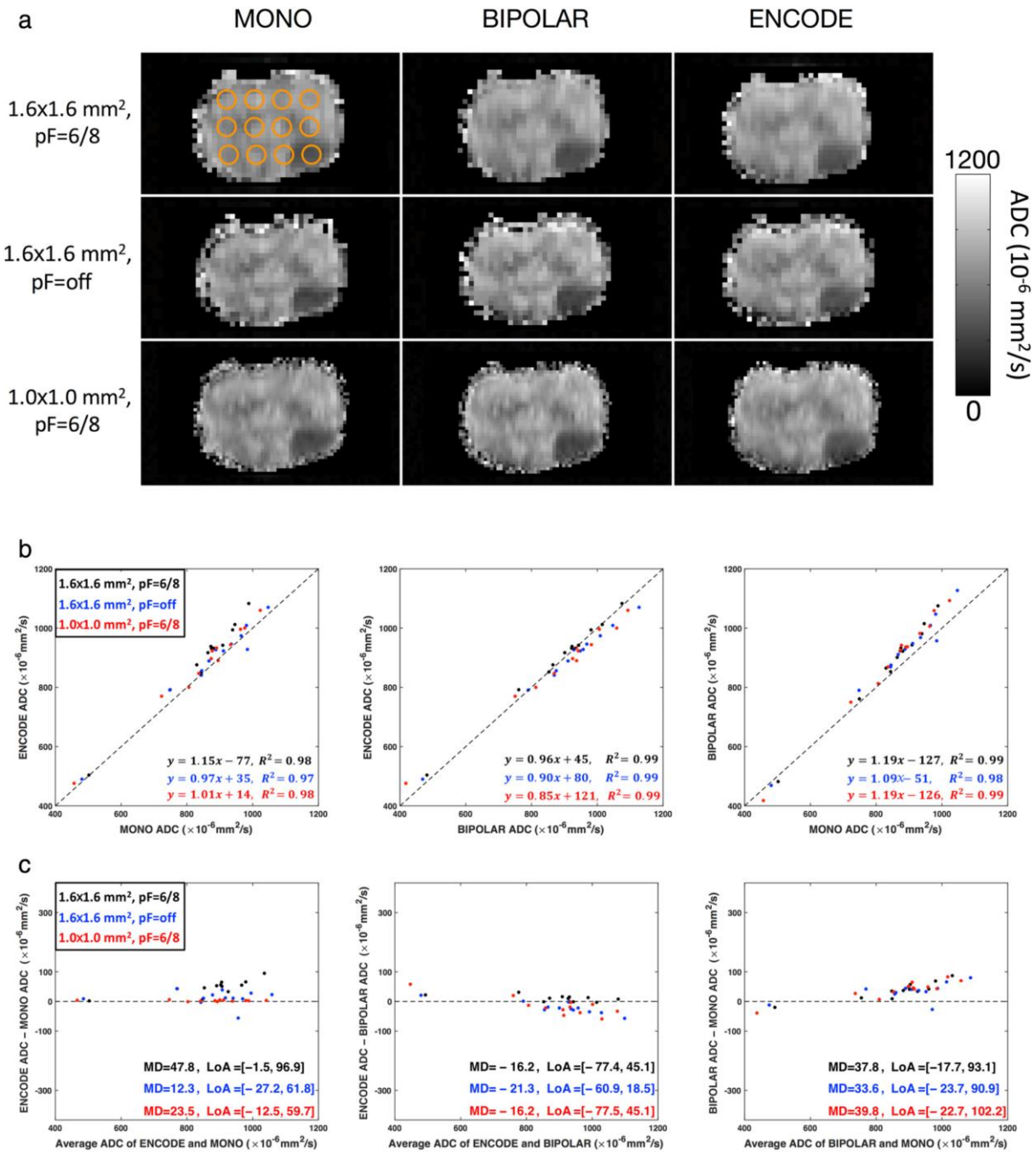

Figure 3.5. Comparison of ADC in an ex vivo prostate specimen. **(a)** Ex vivo prostate ADC maps obtained using MONO, BIPOLAR, and ENCODE sequences for standard and higher-resolution protocols. **(b)** Linear correlation results between MONO, BIPOLAR, and ENCODE ADC for standard and higher-resolution protocols. The dashed line represents y = x. The regions of interest for measuring ADC are denoted as orange circles in (a). **(c)** Bland–Altman plots comparing ADC obtained using MONO, BIPOLAR, and ENCODE sequences for standard and higher-resolution protocols. pF: partial Fourier factor.

3.3.4 In Vivo Prostate Imaging in Healthy Subjects

SNR and ADC Evaluations

Example *in vivo* prostate DWI and ADC maps are shown in **Figure 3.6**. For the clinical standard imaging protocol, the Kruskal-Wallis test yielded statistically significant SNR differences in prostate PZ ($P<0.05$) and TZ ($P<0.05$) across MONO, BIPOLAR, and ENCODE. ENCODE mean SNR for prostate PZ was 29% higher than BIPOLAR ($P<0.01$) and 8% lower than MONO ($P<0.05$), and ENCODE mean SNR for prostate TZ was 27% higher than BIPOLAR ($P<0.01$) and 13% lower than MONO ($P<0.05$) (**Figure 3.6c**). For higher-resolution imaging using 1.6x1.6 mm^2 with pF = off, statistically significant differences in SNR were found across sequences in both PZ ($P<0.05$) and TZ ($P<0.05$). ENCODE mean SNR for prostate PZ was 58% higher than BIPOLAR ($P<0.01$) and 17% higher than MONO ($P<0.01$), and ENCODE mean SNR for prostate TZ was 70% higher than BIPOLAR ($P<0.01$) and 21% higher than MONO ($P<0.01$) (**Figure 3.6c**). There were no significant differences between MONO, BIPOLAR, and ENCODE mean ADC in prostate PZ and TZ for the clinical standard imaging protocol (1.6x1.6 mm^2 with pF = 6/8) and higher-resolution protocol (1.6x1.6 mm^2 with pF = off) (**Figure 3.6d**). The higher-resolution *in vivo* imaging protocol using 1.0x1.0 mm^2 with pF = 6/8 yielded DWI with low SNR for all encoding schemes within the clinical standard acquisition time (5 min 53 sec) and were excluded from SNR and ADC comparisons.

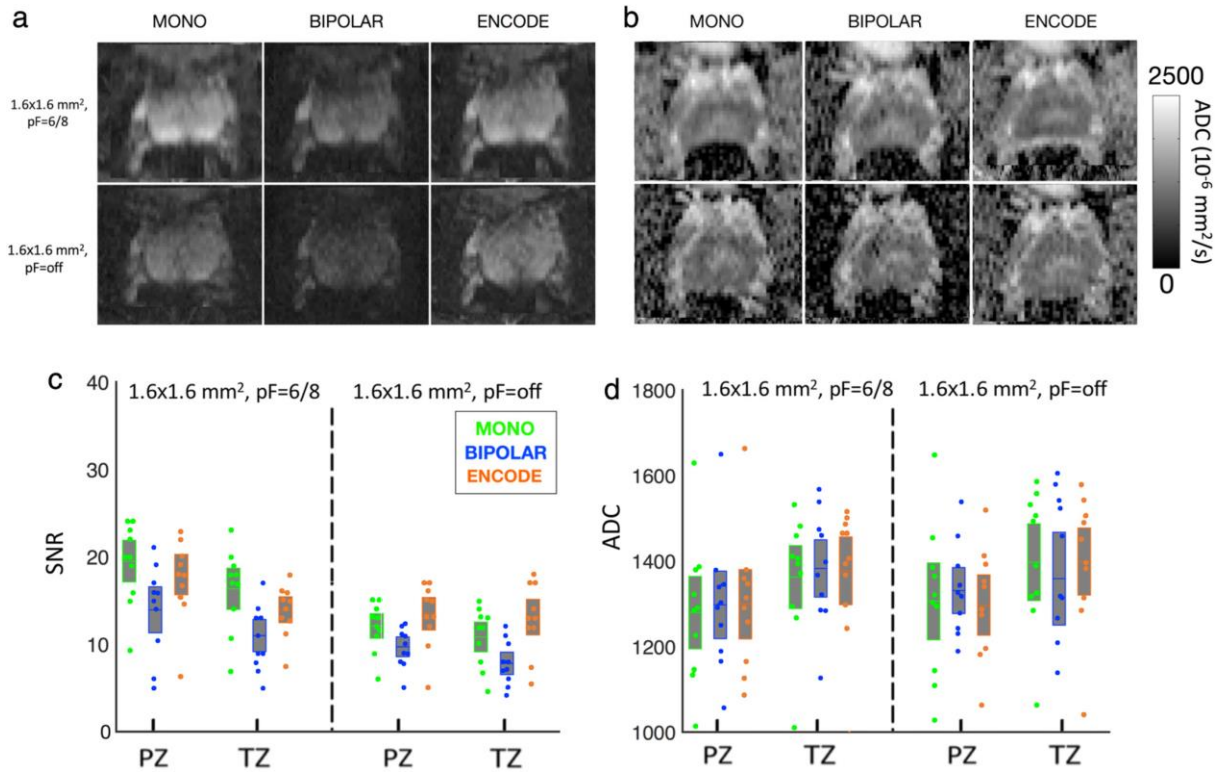

Figure 3.6. Prostate DWI SNR and ADC comparisons in healthy subjects (n = 10). **(a)** in vivo prostate DWI (b-value of 800 s/mm^2) obtained using MONO, BIPOLAR, and ENCODE sequences for standard and higher-resolution protocols. The same display window/level was used for all images. **(b)** In vivo prostate ADC maps obtained using MONO, BIPOLAR, and ENCODE sequences for standard and higher-resolution protocols. **(c)** Boxplots of SNR distributions of MONO, BIPOLAR, and ENCODE DWI for standard and higher-resolution protocols. **(d)** Boxplots of ADC distributions obtained by MONO, BIPOLAR, and ENCODE sequences for standard and higher-resolution protocols. The SNR and ADC results for prostate PZ and TZ are shown in (c,d). pF: partial Fourier factor.

3.3.5 In Vivo Imaging in a Pilot Cohort of PCa Patients

Diagnostic Image Quality Evaluation

Representative images comparing the diagnostic image quality of higher-resolution ENCODE DWI and clinical standard BIPOLAR DWI acquired from a PCa patient are shown in **Figure 3.7.**

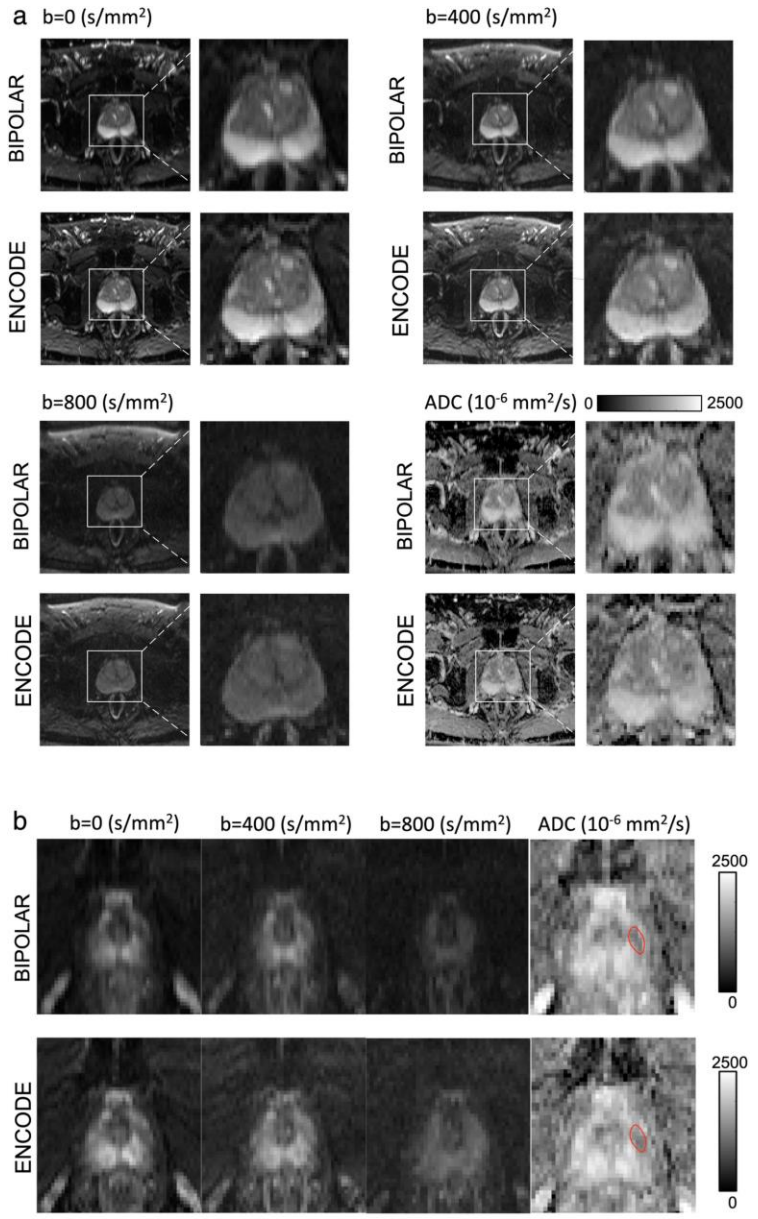

Figure 3.7. Prostate DWI comparisons in a prostate cancer patient. **(a)** Representative DWI and ADC maps acquired in a PCa patient (patient 1) using higher-resolution ENCODE DWI and clinical standard BIPOLAR DWI are shown. Each pair of BIPOLAR and ENCODE diffusion-weighted images with the same b-value are displayed with the same window/level. ENCODE achieved comparable or higher diagnostic image quality compared to the reference clinical prostate BIPOLAR DWI sequence (see Table 3.4). **(b)** A suspected lesion (PI-RADS v2 score of 4) was identified by a radiologist on BIPOLAR and ENCODE ADC maps (red contours). ENCODE ADC ($1453 \pm 370 \cdot 10^{-6} mm^2/s$) and BIPOLAR ADC ($1475 \pm 337 \cdot 10^{-6} mm^2/s$) were comparable to each other in the lesion region of interest (red contour).

Diagnostic image quality scores for all five patients are listed in **Table 3.4**.

Image Quality Scores (Reader 1 / Reader 2 / Reader 3)								
TZ signal	**Patient 1**	**Patient 2**	**Patient 3**	**Patient 4**	**Patient 5**	**Median**	**ICC (Reader1&2, 2&3, 1&3)**	**Mean ICC**
BIPOLAR	2/2/2	2/1/1	2/1/1	3/2/1	4/2/1	2/2/1	0.78/0.93/0.49	0.73
ENCODE	3/3/3	3/2/2	3/2/2	3/3/3	4/3/3	3/3/3		
PZ signal								
BIPOLAR	2/2/2	2/1/1	2/2/1	4/2/1	4/2/1	2/2/1	0.66/0.85/0.86	0.79
ENCODE	3/3/3	3/2/2	3/3/2	4/3/3	4/3/2	3/3/2		
Muscle/Fat Signal								
BIPOLAR	2/2/1	2/1/1	2/2/1	3/2/1	3/1/1	2/2/1	0.60/0.75/0.83	0.73
ENCODE	3/3/3	3/2/3	3/3/2	4/3/3	4/2/3	3/3/3		
Rectum Signal								
BIPOLAR	2/2/1	2/2/1	2/1/1	4/2/1	2/2/1	2/2/1	0.69/0.76/0.57	0.67
ENCODE	3/3/3	3/3/3	3/2/3	4/3/2	3/3/2	3/3/3		
Overall DWI Quality								
BIPOLAR	2/2/1	2/1/1	2/2/1	3/2/1	4/2/1	2/2/1	0.73/0.89/0.70	0.77
ENCODE	3/3/3	3/3/3	3/3/2	4/3/3	4/3/3	3/3/3		
Lesion conspicuity on ADC								
BIPOLAR	2/3/1	2/2/1	2/1/1	3/2/2	2/2/1	2/2/1	0.41/0.26/0.70	0.46
ENCODE	3/3/2	2/2/2	3/2/2	3/3/1	2/3/2	3/3/2		

Table 3.4:
Radiological image quality scores for prostate DWI using the higher-resolution ENCODE and clinical standard BIPOLAR protocols. The images were scored for prostate transition zone (TZ) signal, prostate peripheral zone (PZ) signal, muscle/fat signal, rectum signal, overall DWI quality, and lesion conspicuity on the ADC map. A scale of 1-4 was used: 1 denotes bad image quality and 4 denotes excellent image quality. ICC: intra-class correlation coefficient.

ENCODE achieved higher or similar scores than BIPOLAR in all six categories from three readers. Inter-reader agreement among three independent readers in terms of mean ICC was good to excellent for TZ signal, PZ signal, muscle signal, rectum signal, and overall DWI signal categories, and fair for lesion conspicuity on ADC maps. These results show that the proposed higher-resolution ENCODE prostate DWI sequence has comparable or higher diagnostic image quality compared to the reference clinical BIPOLAR DWI sequence, and was consistent among three independent readers.

ADC Evaluation

In five PCa patients, four suspected cancerous lesions were identified on standard prostate mp-MRI. For the first suspected lesion (PI-RADS v2 score of 4, lesion diameter 1 cm), which was in the PZ, ENCODE ADC = 1453±370 $\cdot 10^{-6}$ mm^2/s and BIPOLAR ADC = 1475±337$\cdot 10^{-6}$ mm^2/s. For the second suspected lesion (PI-RADS v2 score of 3, lesion diameter 0.9cm), which was in the TZ, ENCODE ADC = 1227±301 $\cdot 10^{-6}$ mm^2/s and BIPOLAR ADC = 1261±299$\cdot 10^{-6}$ mm^2/s. For the third suspected lesion (PI-RADS v2 score of 4, lesion diameter 1cm), which was in the PZ, ENCODE ADC =944±282 $\cdot 10^{-6}$ mm^2/s and BIPOLAR ADC =1089±190 $\cdot 10^{-6}$ mm^2/s. For the fourth suspected lesion (PI-RADS v2 score of 4, lesion diameter 1.4cm), which was in the TZ, ENCODE ADC =1097±217 $\cdot 10^{-6}$ mm^2/s and BIPOLAR ADC =985±204 $\cdot 10^{-6}$ mm^2/s. In addition, ENCODE ADC =1800±220 $\cdot 10^{-6}$ mm^2/s (mean ± SD of all patient ROIs) and BIPOLAR ADC = 1872±178 $\cdot 10^{-6}$ mm^2/s in benign PZ, and ENCODE ADC = 1393±135 $\cdot 10^{-6}$ mm^2/s and BIPOLAR ADC = 1441±77 $\cdot 10^{-6}$ mm^2/s in benign TZ. These results show that ENCODE and BIPOLAR ADC were comparable to each other in all regions of suspected PCa, benign PZ, and benign TZ.

3.3.6 Combining ENCODE with rFOV to Reduce Prostate Geometric Distortion

Quantitative Prostate Geometric Distortion Comparison

The quantitative evaluation of prostate geometric distortion in terms of the Dice similarity coefficient (DSC) was shown in **Figure 3.8**. In 36 patients, rFOV-ENCODE achieved higher median DSC than standard BIPOLAR DWI (0.87 vs 0.80, P<0.01).

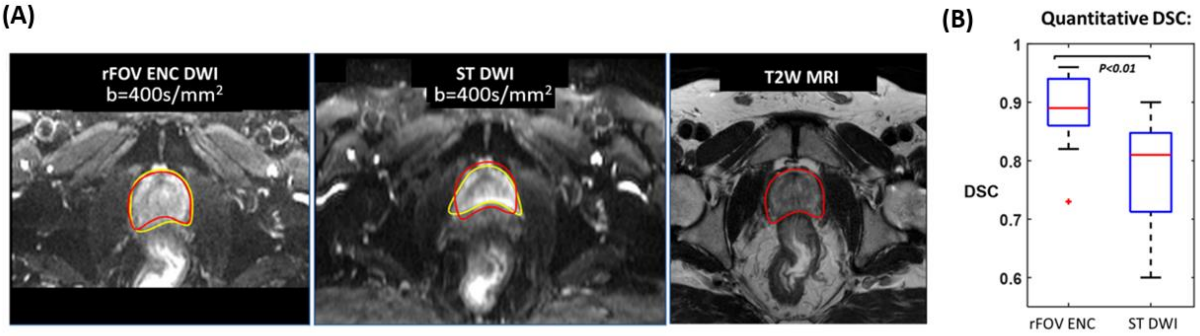

Figure 3.8. Quantitative prostate geometric distortion comparisons between rFOV-ENCODE DWI, standard BIPOLAR DWI, with respect to the T2 TSE MRI reference **(A)** Representative example for comparing geometric fidelity of rFOV-ENCODE DWI and standard BIPOLAR (ST) DWI in reference to the T2 TSE anatomical reference. **(B)** Boxplots of the Dice's similarity coefficient (DSC) calculated between mid-gland prostate contours on DWI (rFOV-ENCODE or BIPOLAR with A-P phase encoding direction) and T2W TSE from 36 prostate cancer patient scans.

Qualitative Radiological Image Quality Assessment of Prostate Geometric Distortion

Representative examples of image quality comparison between rFOV-ENCODE and standard BIPOLAR DWI were shown in **Figure 3.8**. The qualitative radiological image quality scoring results were shown in **Figures 3.9 and 3.10**.

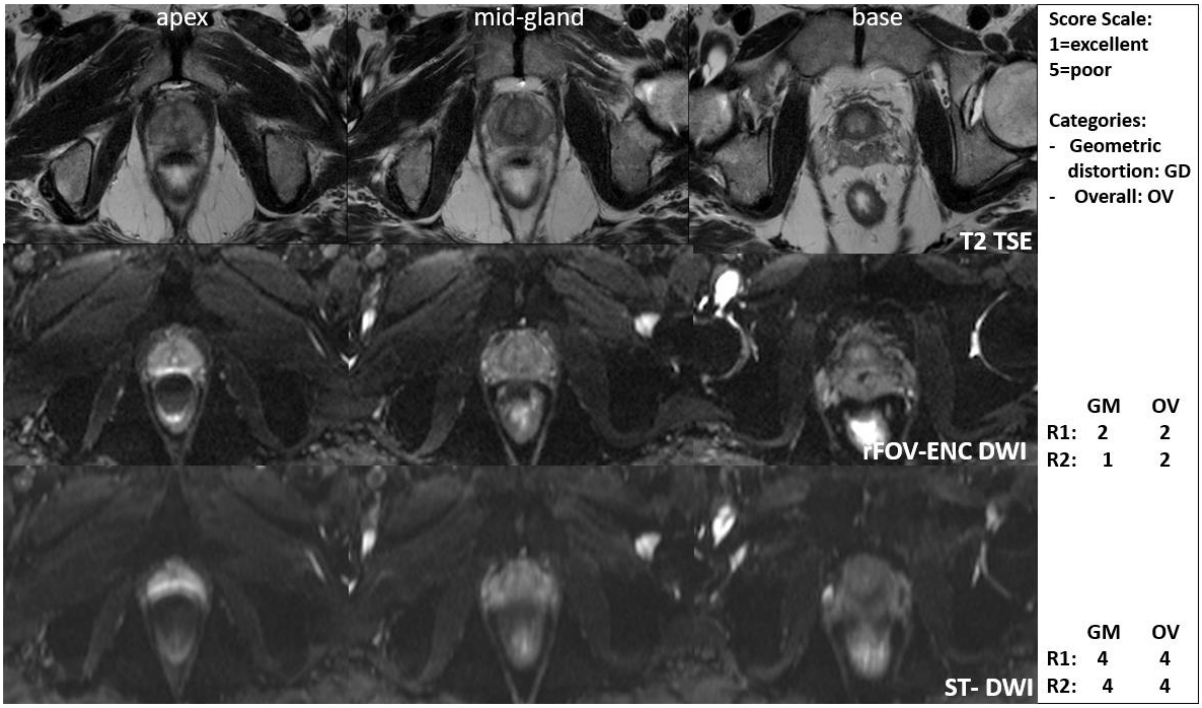

Figure 3.9. Qualitative radiological image quality assessment of geometric distortion in a prostate cancer patient between rFOV-ENCODE DWI and standard (ST) bipolar DWI, along with T2W TSE as the geometric reference. In this example, both expert radiologist reader 1 (R1) and reader 2 (R2) scored rFOV-ENCODE DWI with lower geometric distortion scores and better overall image quality scores compared to ST DWI after reviewing both sequences across slices covering the prostate apex to base in a blinded and randomized fashion, using T2W TSE as the reference.

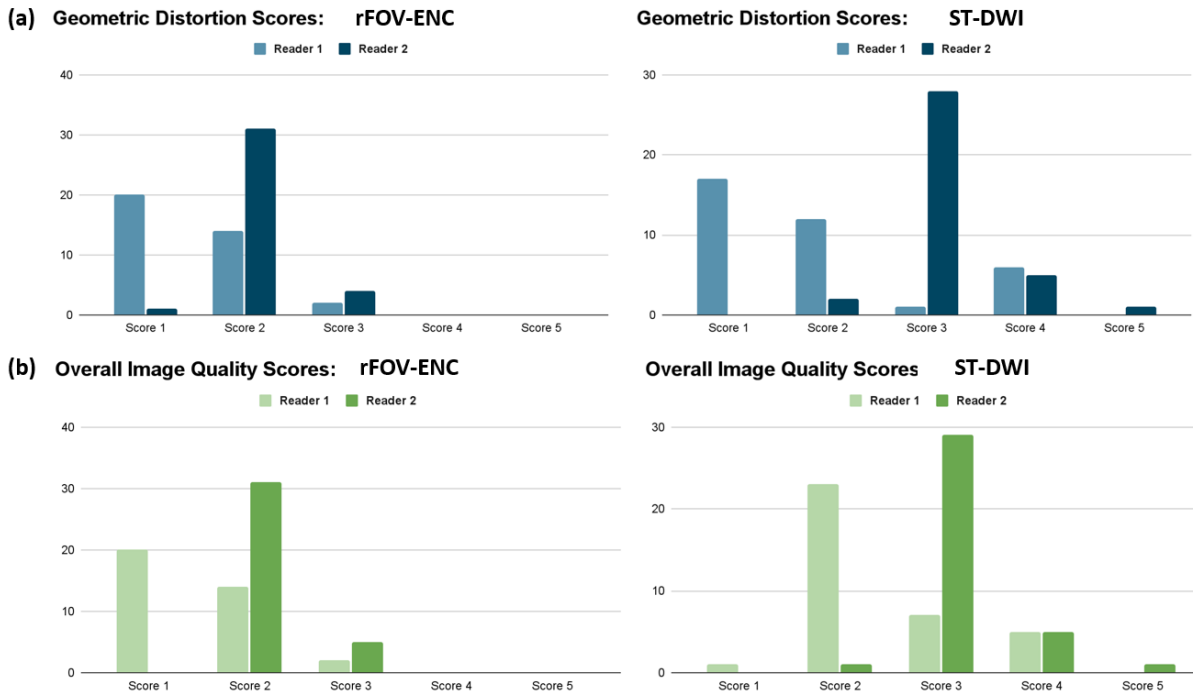

Figure 3.10. Qualitative geometric distortion (a) and overall image quality scores (b) for rFOV-ENCODE (left) and ST-DWI (right) rated by two expert radiologists (Reader 1 and 2). Prostate geometric distortion was scored on a 5-point scale (1: none, 2: minimal, 3: mild, 4: moderate, 5: severe), as was overall diagnostic image quality (1: excellent, 2: good, 3: moderate, 4: compromised, and 5: poor image quality).

rFOV-ENCODE achieved lower geometric distortion scores than standard BIPOLAR DWI (R1: 1.2±0.4 vs 1.9±1.1, P<0.001; R2: 2.0±0.4 vs 3.1±0.5, P<0.001) and better overall image quality scores (R1: 1.5±0.6 vs 2.4±0.8, P<0.001; R2: 2.1±0.4 vs 3.2±0.5, P<0.001). Notably, the scores for rFOV-ENCODE were all in the range of 1~3, while standard BIPOLAR DWI had scores of 4~5 in 6/36 (16.7%) cases, indicating compromised diagnostic quality due to geometric distortion of the prostate.

3.4 **Discussion**

In this study, a new prostate DWI method based on the ENCODE framework was compared to standard MONO and BIPOLAR encoding schemes for clinical standard and higher-resolution protocols. Our results demonstrated eddy current-induced distortion artifacts were evident on MONO, while effectively suppressed by both BIPOLAR and ENCODE. For a clinical standard prostate DWI protocol, ENCODE substantially reduced TE compared to BIPOLAR (63 ms vs 78 ms) and resulted in significantly higher DWI SNR in prostate TZ and PZ. No significant differences were found in mean TZ and PZ ADC between MONO, BIPOLAR, and ENCODE. For higher-resolution prostate DWI protocols, ENCODE achieved the shortest TE and highest prostate DWI SNR among all techniques.

Prostate DWI is known to be sensitive to distortion artifacts that lead to inaccurate localization and representation of prostate tissues including cancer [8,81,7,11,49]. Eddy current fields originating from the use of large gradient amplitudes for diffusion encoding, if not carefully compensated or corrected, can have an enduring impact during the EPI readout and contribute one source of distortion artifacts in prostate DWI [52,79,54,8,81] . Our phantom and *ex vivo* imaging experiments used identical imaging parameters as clinical *in vivo* prostate DWI, with the benefit of no patient motion and minimal susceptibility effects [88], thus distortion could be attributed to eddy current effects with high confidence. The results from our *ex vivo* prostate DWI scans demonstrated that directionally dependent discrepancies of the prostate boundary and misrepresentation of prostate tissue locations were evident on MONO DWI, but these effects were effectively suppressed on BIPOLAR and ENCODE. Although in this study we did not specifically compare the eddy current distortion effects for *in vivo* prostate DWI, eddy currents originate purely

from the imaging hardware system and gradient waveform design. Thus, our findings in phantom and *ex vivo* experiments would translate to *in vivo* imaging.

The generated ENCODE waveforms and associated TE mainly depends on the targeted b-values and EPI readout duration for the imaging protocol. The clinical prostate DWI protocol at our institution uses a maximum b-value of 800 s/mm^2, with FOV and spatial resolution parameters that result in T_{EPI} =17 ms. Under this protocol, the resultant ENCODE waveform and associated TE is substantially shorter than BIPOLAR and slightly longer than MONO. Due to reduced T_2 decay with shortened TE, our results demonstrated 27% and 29% higher DWI SNR in prostate TZ and PZ compared to BIPOLAR. This indicated that ENCODE can generate diffusion encoding waveforms with similarly short TE as MONO to provide higher SNR than BIPOLAR and reduce eddy current in prostate DWI at the same time. Prostate DWI typically uses multiple repetitions (averages) to improve SNR. Our clinical prostate DWI protocol with BIPOLAR encoding uses seven repetitions for all b-values, which results in a total scan time of 5 min 53 sec. Since each individual ENCODE prostate DWI acquisition has ≥25% higher SNR in prostate TZ and PZ than BIPOLAR, ENCODE can potentially reduce number of averages from seven to five with total DWI scan time down to 4 min 12 sec (estimated based on $SNR_{avg} \propto \sqrt{N_{avg}}$, to maintain the same averaged SNR as the reference clinical BIPOLAR DWI protocol). Prostate DWI using multiple averages may also suffer from motion artifacts during long scans [93,47]. Therefore, a shortened ENCODE prostate DWI could have less motion artifacts and potentially improved image quality.

ADC is a key MRI parameter for detecting and characterizing prostate cancer [3,67,94]. Despite differences in diffusion encoding waveforms, no significant differences were found in mean prostate TZ and PZ ADC between MONO, BIPOLAR, and ENCODE in healthy subjects (N=10). In the pilot PCa patient study (N=5), ENCODE ADC was also in agreement with ADC

obtained by the clinical BIPOLAR DWI sequence in benign tissue ROIs and suspected cancer ROIs. However, the ADC comparisons between DWI methods with varying diffusion encoding waveforms has intrinsic limitations because the mono-exponential DWI model and ADC has inaccuracies due to underlying complex prostate tissue microstructure. For example, recent studies have shown that at the sub-voxel level, cellular and luminal compartments in prostate tissues have appreciable T_2 differences. As a result, the ADC calculated at the voxel level using the mono-exponential model would be dependent on TE due to T_2 relaxation effects [19,21]. On the other hand, advanced DWI methods are taking advantage of the multi-component T_2 signal properties and non-Gaussian diffusion phenomenon in microscopic tissue compartments to map prostate microstructure by sampling and modeling DWI signals at various TEs and diffusion times [19]. ENCODE could potentially improve the SNR as well as achieve a larger range of TE for advanced DWI acquisition as it optimizes the minimal achievable TE for any given b-value, to further improve the performance of DWI-based prostate microstructure mapping [19,95].

ENCODE was also evaluated for higher-resolution prostate DWI protocols. In this work, two higher-resolution protocols were studied: voxel size reduced to 1.0x1.0 mm^2 from 1.6x1.6 mm^2, or partial Fourier factor pF changed to 1 (i.e., off) from 6/8. Changes in voxel size and pF resulted in an increase in T_{EPI} from 17 ms to 24 ms and 28 ms, respectively. Theoretical comparisons showed that while MONO and BIPOLAR waveforms and the associated TE increase linearly with increased T_{EPI} (MONO TE: 57 ms to 70 ms, BIPOLAR TE: 77 ms to 102 ms), ENCODE TE had minimal increase from 63 ms to 67 ms. This is because the ENCODE framework optimized the temporal footprint of the diffusion encoding waveforms for any given T_{EPI}, including long T_{EPI}. For higher-resolution prostate DWI protocols, ENCODE had the shortest TE and highest SNR in prostate TZ and PZ compared to BIPOLAR and MONO. This means ENCODE could be an

advantageous diffusion encoding scheme to maintain the SNR of higher-resolution prostate DWI by reducing the amount of T_2 decay due to TE increase. However, higher-resolution prostate DWI still has reduced SNR due to reduced imaging voxel size. Multiple averages and longer total scan duration may still be required to achieve sufficient SNR, but fewer averages would be required for ENCODE compared to BIPOLAR and MONO. In the future, it remains to be seen whether this improvement in SNR for higher-resolution DWI would result in more accurate detection and characterization of prostate cancer, especially for smaller PCa lesions that are challenging to detect using clinical standard mp-MRI.

Partial Fourier acquisition and reconstruction is commonly used for clinical DWI protocol to reduce TE by keeping EPI readout short, but it also results in a broadened point spread function and decreases the effective resolution of the image [85]. Using ENCODE, prostate DWI can be acquired with full Fourier acquisition without penalty in substantially increased TE, maintaining sufficient SNR while improving effective resolution of DWI. The tendency of higher diagnostic image quality scores for ENCODE in all categories compared to a clinical BIPOLAR prostate DWI sequence could be due to the improvement in effective imaging resolution (ENCODE: pF = off vs. clinical BIPOLAR: pF = 6/8) and SNR (ENCODE: TE= 67 ms vs. clinical BIPOLAR: TE = 77 ms), which can improve the depiction of prostate tissues for radiological evaluation of prostate anatomy and function [10,11].

To address both susceptibility and eddy current-induced geometric distortion in the prostate, we designed a combined rFOV-ENCODE technique that utilized outer volume saturation RF pulses to reduce PE-FOV and enable shorter EPI readout while mitigating eddy current effects from diffusion encoding using ENCODE. In the pilot study of 36 patients, both quantitative and qualitative assessment found that the rFOV-ENCODE performed better in terms of reducing

overall geometric distortion than standard full FOV BIPOLAR DWI. These results showed that both eddy current and susceptibility sources of geometric distortion need be addressed at the same time to better maintain the geometric fidelity of the prostate on DWI, supporting a combined approach to tackle prostate DWI distortion.

Limitations

Our study has limitations. First, *in vivo* prostate DWI SNR comparisons were performed in healthy subjects but not in prostate cancer patients. For SNR measurements, each DWI protocol was acquired seven times to generate voxel-by-voxel SNR maps by calculating the temporal mean divided by standard deviation. Acquiring SNR maps for all evaluated protocols requires substantial scan time and was not practical to perform for the clinical PCa patient scans. However, the improvement in SNR is related to reduction in TE, which theoretically translates to clinical patient imaging. Second, all diffusion encoding waveforms compared herein were generated on a 3T MRI system with high performance gradient hardware with G_{max} = 76 mT/m, and the ENCODE framework takes full advantage of G_{max} in this case to achieve the minimally possible TE. On other MRI systems with lower G_{max}, the ENCODE waveform and minimal TE are expected to be longer and the relative advantages in reducing TE and improving SNR compared to BIPOLAR and MONO would be different. Third, for diagnostic image quality analysis, we only evaluated ENCODE compared to clinical DWI in five patients. The sample size was too small to perform statistical analysis of the differences (or improvements) using ENCODE higher-resolution DWI compared to clinical sequences for diagnosis of PCa. We plan to enroll more eligible PCa patients for future research. Fourth, we only investigated ENCODE compared to MONO and BIPOLAR using the diffusion-weighted single-shot EPI sequence, since it is the most widely used prostate

DWI acquisition scheme. There is growing interest in alternative DWI sequences, such as multi-shot readout-segmented EPI [7]. The specific ENCODE waveforms and TE and SNR properties using these alternative DWI acquisition schemes would be an interesting topic for future work. Fifth, we only evaluated ENCODE DWI with respect to MONO/BIPOLAR using the clinically employed mono-exponential ADC model, which is inaccurate as multiple microscopic tissue compartments exist in prostate tissue. The effects of ENCODE waveforms and potential advantages of shortened TE in modeling prostate microstructure using DWI need to be evaluated in a separate study that uses more advanced multi-component signal models [95,96].

3.5 **Conclusion**

We used the ENCODE framework to generate eddy-current compensated diffusion encoding with minimized TE for prostate DWI for both standard and higher resolution imaging protocols. The combined ENCODE with reduced phase encoding FOV DWI acquisition further reduced overall geometric distortion compared to standard FOV BIPOLAR DWI by addressing both eddy current and susceptibility-induced geometric distortion in the prostate. The improved performance in reducing geometric distortion artifacts and improving prostate DWI SNR using ENCODE prostate DWI has the potential to improve prostate cancer diagnosis.

Chapter 4 High-Resolution Prostate Diffusion MRI Using Eddy Current-Nulled Convex Optimized Diffusion Encoding with Random Matrix Theory-Based Denoising

4.1 Introduction

High-spatial-resolution prostate DWI (e.g., in-plane resolution $\leq$1.0x1.0 mm^2) has potential to provide finer depiction of prostate tissue and improve conspicuity of lesions with diffusion contrast [11,60,10,12,9] compared to standard prostate DWI with in-plane resolution limited to around 1.6x2.0 to 2.0x2.0 mm^2, and can enable ADC mapping with reduced partial volume averaging effects [13,15], which may improve the delineation of PCa when the tumor is intermixed substantially with adjacent normal tissue and smaller imaging voxels are desired for better tumor differentiation [13,10]. However, the signal-to-noise ratio (SNR) penalty with smaller voxel sizes makes it technically challenging [14], especially with the increasingly common practice of using a phased-array body coil instead of an endorectal coil for prostate MRI [55,63]. Since standard prostate DWI at moderate in-plane resolution (e.g. 1.6x2.0 mm^2) already performs signal averaging (e.g., 6-10 measurements) to address the intrinsically low SNR [8], further increasing the number of signal averages to maintain SNR for higher spatial resolution may lead to prolonged exam durations.

The ENCODE framework is a recently proposed diffusion waveform design technique [64,28,97] that automatically minimizes echo time (TE) while compensating for eddy current effects from diffusion encoding gradients for any given DWI protocol. It was recently shown that ENCODE single-shot echoplanar imaging (EPI) prostate DWI [97] improved SNR by maintaining a short TE to limit T_2 signal decay while reducing eddy current-induced distortion in the prostate

compared to conventional twice-refocused bipolar and monopolar DWI waveforms, especially for protocols with longer EPI readout [28,54,6] , i.e., those associated with higher spatial resolution. On the other hand, DWI using reduced field-of-view (FOV) acquisition in the phase encoding direction has also been demonstrated to be an effective technique in limiting susceptibility-induced distortion for achieving higher spatial resolution for prostate DWI [60,59]. This indicates that combining ENCODE with the reduced-FOV (rFOV) technique could be an advantageous DWI acquisition strategy for high-resolution prostate DWI with short TE and reduced geometric distortion due to eddy current and susceptibility effects. However, such a high-resolution DWI technique is still expected to suffer from SNR losses proportional to the reduction in voxel size (e.g., from 1.6x2.0 to 1.0x1.0 mm^2 in-plane resolution), and maintaining SNR remains a challenge.

Recently, random matrix theory (RMT)-based denoising techniques, such as Marchenko-Pastur principal component analysis (MP-PCA) [31,66], achieved promising performance in reducing thermal noise for diffusion MRI by exploiting the redundancy of noise statistics and anatomical/functional information shared across multiple diffusion encoding strengths/directions and repeated acquisitions (i.e., signal averaging) inherent to DWI protocols [31]. Moreover, based on RMT, a data-driven threshold can be automatically determined to distinguish between the noise-only and signal-carrying components for effective denoising while preserving the underlying signals that contain anatomical and functional information [31,30]. MP-PCA denoising of diffusion MRI has been demonstrated in multiple organs including the prostate [98], but it has not been specifically evaluated in the context of improving SNR for high-spatial-resolution (e.g., 1.0x1.0 mm^2) prostate DWI. Since ENCODE acquisition and RMT-based denoising each address the SNR limitations of high-resolution prostate DWI from the acquisition and reconstruction

perspectives, respectively, the joint application of both methods may lead to further improvements in maintaining SNR.

Therefore, the purpose of this study was to develop a combined ENCODE-RMT technique and evaluate its technical performance for maintaining the SNR and robustness of ADC mapping for high-resolution (in-plane: 1.0x1.0 mm^2) prostate DWI. Specifically, the improvement in ENCODE DWI SNR with RMT-based denoising and the associated improvement in ADC mapping in terms of precision and accuracy in the prostate were quantitatively measured and evaluated, with respect to a standard-resolution clinical DWI sequence, in a pilot cohort of subjects with clinical suspicion of PCa. This enabled a reduction in the phase encoding FOV (PE-FOV) to achieve an imaging matrix with higher in-plane spatial resolution of 1.0x1.0 mm^2 vs. 1.6x2.2 mm^2 in the standard full-FOV prostate DWI protocol while limiting B_0 inhomogeneity-induced geometric distortion.

The achievable reduction in PE-FOV depended on specific peripheral nerve stimulation limits on each MRI system, and the minimal PE-FOV permitted on each scanner under a parallel imaging acceleration factor of 2 were used for high-resolution DWI protocols, which reduced PE-FOV by 40% compared to standard full-FOV prostate DWI. Overall, the EPI readout duration characterized by EPI time-to-echo increased from 17 ms (full-FOV with standard resolution of 1.6x2.2 mm^2) to 24 ms for reduced PE-FOV (rFOV) high-resolution 1.0x1.0 mm^2 protocols.

4.2 **Methods**

4.2.1 High-Resolution ENCODE Prostate DWI Sequence and Protocol

The proposed high-resolution prostate DWI protocol was designed to have the same scan time as the standard-resolution clinical DWI protocol used at our institution [40], with matched

parameters including b-values, diffusion directions, and repetitions for signal averaging (**Table 4.1**).

Parameter	**High-resolution ENCODE**	**Standard bipolar**
Echo time (TE) (ms)	66; 73 [1]	80
b value (s/mm^2)	0, 100, 400, 800	
Repetition time (TR) (ms)	4800	
Field of view (mm^2)	220 x 124 [2]	260 x 216
Acquired resolution (mm^2)	1.0 x 1.0	1.6 x 2.2
Slice thickness (mm)	3.6	
Phase-encoding direction	Anterior to Posterior (A-P)	
Diffusion directions	3-scan trace	
Parallel imaging factor	2	
Partial Fourier factor	6/8	
Fat saturation method	SPAIR	
Number of slices	16-20	
Averages	7	
Scan time (min:sec)	5:50	

Table 4.1:
Sequence parameters for high-resolution ENCODE prostate diffusion MRI and clinical standard-resolution twice-refocused bipolar diffusion MRI. SPAIR: SPectral Attenuated Inversion Recovery. *Note: [1] The minimum TE achieved by the ENCODE waveform depends on gradient hardware performance limits. The TE was 66 and 73 ms on a standard-bore scanner (3T Prisma, Siemens, Germany; Gmax=76 mT/ms; 60-cm diameter bore) and a wide-bore scanner (3T Vida, Siemens, Germany; Gmax=55 mT/ms; 70-cm diameter bore), respectively. [2] The high-resolution ENCODE sequence used outer volume suppression RF pulses to reduce the phase-encoding field-of-view and enable image acquisition with higher in-plane spatial resolution while reducing B_0 inhomogeneity-induced geometric distortion.

One main difference between the high-resolution ENCODE DWI protocol and the standard biploar DWI protocol was the application of outer volume suppression RF pulses in the high-resolution protocol to null the signals from tissue outside of the desired FOV centered around the

prostate [29]. This enabled image acquisition with higher in-plane spatial resolution of 1.0x1.0 mm^2 vs. 1.6x2.2 mm^2 in the standard full-FOV prostate DWI protocol while reducing B_0 inhomogeneity-induced geometric distortion [60,29,59].

The achievable reduction in PE-FOV depended on specific peripheral nerve stimulation limits on each MRI system, and the minimal PE-FOV permitted on each scanner under a parallel imaging acceleration factor of 2 were used for high-resolution DWI protocols, which reduced PE-FOV by 40% compared to standard full-FOV prostate DWI. Overall, the EPI readout duration characterized by EPI time-to-echo increased from 17 ms (full-FOV with standard resolution of 1.6x2.2 mm^2) to 24 ms for reduced PE-FOV (rFOV) high-resolution 1.0x1.0 mm^2 protocols.

Under identical gradient hardware parameters to reach a maximum b-value of 800 s/mm^2 with 3-scan trace diffusion encoding for high-resolution rFOV DWI protocols, the minimal achievable TE using ENCODE, conventional twice-refocused bipolar, and conventional monopolar waveforms were 66/98/69 ms and 73/93/71 ms on one standard-bore whole-body 3 T MRI system (G_{max}=76 mT/ms, 60-cm diameter bore; Prisma, Siemens, Germany) and one wide-bore whole-body 3 T MRI system (G_{max}=55 mT/ms, 70-cm diameter bore; Vida, Siemens, Germany), respectively. ENCODE achieved nearly identical or shorter TE than monopolar DWI with the additional benefit of eddy current compensation, and always reduced TE by about 20 ms compared to bipolar DWI for both scanners, highlighting the advantages of ENCODE for reducing TE (improving SNR) compared to conventional DWI sequences for high-resolution prostate DWI. For the detailed descriptions of ENCODE waveform design, we refer the readers to the prior publications [28,97].

4.2.2 Theoretical and Application-Specific Considerations for RMT-Based Denoising:

Based on RMT, for a low rank 2D matrix contaminated by additive noise with an independent identically distributed (i.i.d.) zero-mean Gaussian distribution [31,66], the asymptotic distribution of noise-only component singular values will follow the Marchenko-Pastur (MP) distribution, while the signal-carrying components will appear as "spiked" singular values falling on the right side of the bounded MP distribution [66]. This RMT-based model of noise provides a data-driven threshold to distinguish the signal from noise components in the singular value spectrum domain for denoising using MP-PCA [31,30].

MP-PCA has been used to denoise magnitude images in DWI and has proven to be effective for datasets with moderate SNR (e.g., >10) [31]. However, for low SNR applications (e.g., <5 for high-resolution DWI), applying MP-PCA on complex DWI data becomes necessary for effective denoising [99-101]. as the Rician noise distribution of magnitude data no longer approximates the Gaussian distribution [102].

In addition, modern DWI datasets are commonly acquired with parallel imaging (PI) acceleration, such as Sensitivity Encoding (SENSE) or GeneRalized Autocalibrating Partial Parallel Acquisition (GRAPPA) [62,103], which also alters noise statistics and introduces channel-dependent spatially varying noise amplification [104]. Coil combination algorithms (e.g., a sum of squares or adaptive coil combination [65] can also lead to further deviation from white Gaussian noise statistics in the coil-combined DWI . Addressing these sources of noise statistics distortion before performing MP-PCA, e.g., by using noise normalization techniques, becomes crucial for satisfying RMT assumptions [101].

Lastly, the choice of the dimensions (e.g., 3D or 2D) of the local spatial kernel for forming the locally low rank matrix for MP-PCA also depends on the properties of the specific dataset. In contrast to most brain DWI applications that have isotropic high resolution (e.g., 1.25^3 mm^3), prostate DWI is commonly acquired with substantially higher in-plane resolution than slice resolution [8]. This can cause larger signal intensity and phase differences across voxels along the slice direction [105]. Thus, the use of 2D local spatial kernels for denoising complex prostate DWI data with MP-PCA is more appropriate to satisfy the spatial locally low rank assumption.

4.2.3 RMT Denoising Pipeline

Inspired by prior RMT denoising works [100,101,106,99,31] and motivated by the theoretical and application-specific considerations mentioned in the previous section, in order to minimize deviations from the i.i.d. noise statistics assumption of RMT for MP-PCA, we designed a reconstruction, denoising, and processing pipeline for high-resolution ENCODE DWI (**Fig. 4.1**). The main steps in our pipeline are described below.

1. A separate noise scan (part of the calibration scan for DWI) was used to estimate the inter-coil-channel noise covariance matrix, which was then used to de-correlate the received DWI signal and noise across coil channels in the actual acquisition through Cholesky decomposition [103,99].

2. A 3-line navigator was used to perform linear phase correction of k-space data for reducing the ghosting artifacts resulting from misalignment of odd and even EPI echoes.

3. The scanner-introduced k-space zero-filling associated with partial Fourier acquisition and reconstruction was undone [99] (i.e., zeros were removed from k-space and the k-space matrix dimensions were reverted to the originally acquired size). This step avoided the introduction of spatially correlated noise into the image domain [107] before MP-PCA. Later in the pipeline (see

step 6), the zeros were re-introduced into k-space to perform partial Fourier reconstruction after denoising and prior to coil combination.

4. The PI undersampled multi-coil k-space data were reconstructed using GRAPPA [62]. At the same time, coil-by-coil g-factor maps characterizing the spatially varying noise amplifications were computed analytically using knowledge of the GRAPPA convolution kernel [62]. The GRAPPA-reconstructed images for each coil were divided by its corresponding g-factor map to transform its spatially varying noise statistics to spatially stationary noise. This helped to satisfy the assumptions of RMT and MP-PCA that local spatial patches possess a constant noise variance [101].

5. MP-PCA denoising of complex DWI signals was performed in a channel-by-channel and slice-by-slice fashion. A sliding window incorporating a 2D 3x3 local spatial kernel was vectorized into one dimension (N_r=9) and combined with the diffusion contrast encoding dimension (N_{diff}=70: 4 b-values; 3 directions for b-values >0; 7 repetitions) to form the 2D matrix for MP-PCA denoising of data in each coil channel separately. In this step, we chose a minimal local kernel size of 3x3 for MP-PCA to better satisfy the locally low rank assumption. This implied that we assumed the voxels at directly adjacent spatial locations (differing by 1 voxel position) to exhibit some degree of correlation. We did not choose a larger patch size such as 5x5, which would assume that tissue signals separated by two voxels were also similar. The choice of a small kernel size, such as 3x3x3, was also shown to be effective in prior studies applying MP-PCA for denoising isotropic high-resolution brain DWI datasets [99,108].

6. Partial Fourier reconstruction and adaptive coil combination [65] were performed to combine the MP-PCA denoised multi-coil DWI data.

7. Finally, we averaged the magnitude DWI data over multiple repetitions (signal averages) and computed trace-weighted DWI. ADC maps were calculated from DWI using a simple least-squares fit to a mono-exponential signal decay model across DWI signals at 4 b-values (0, 100, 400, 800 s/mm^2).

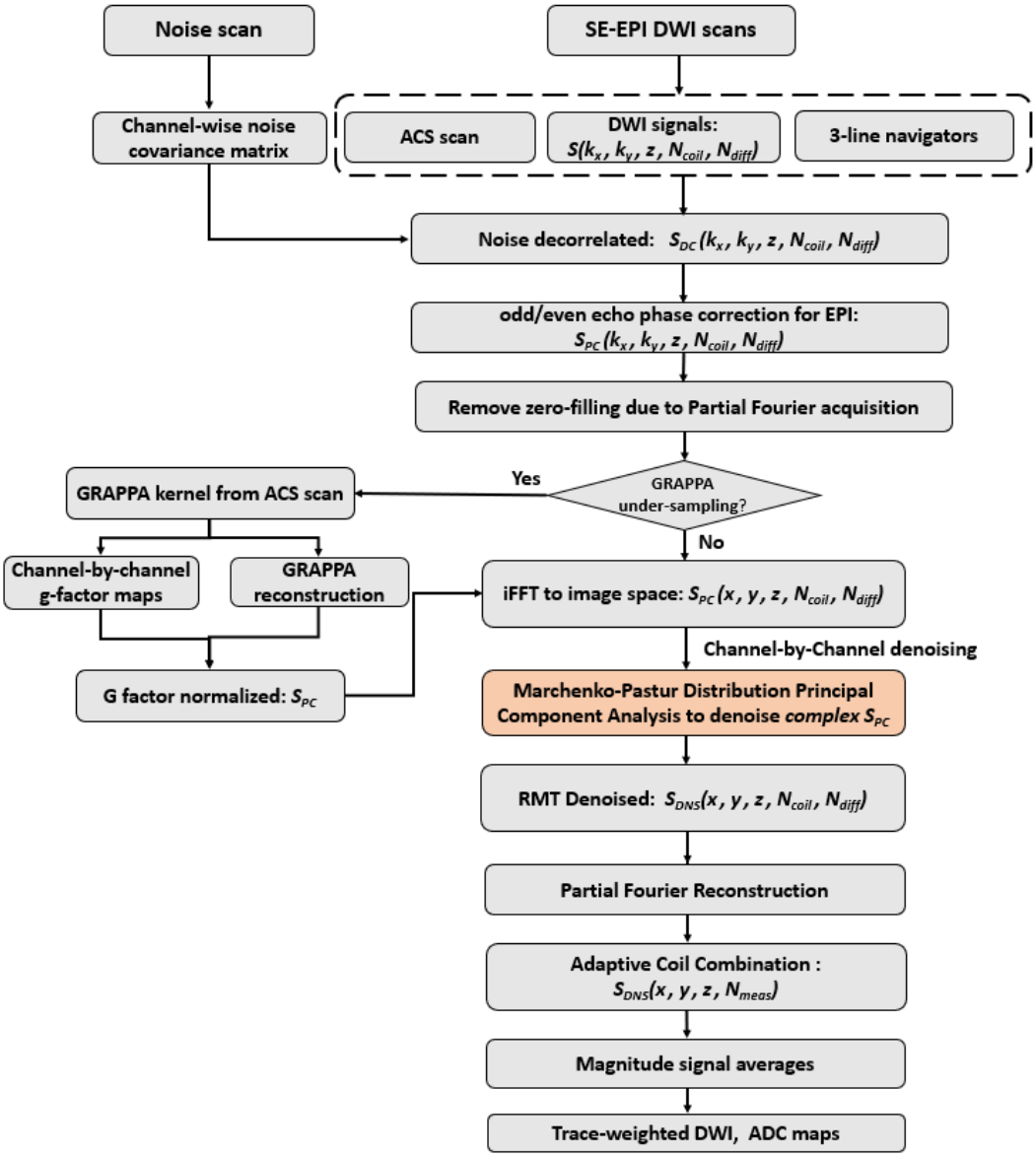

Figure 4.1. Reconstruction pipeline for high-resolution ENCODE prostate DWI with random matrix theory (RMT)-based denoising. The key components included: coil-channel noise decorrelation using a noise scan, odd and even echo phase correction for EPI readouts, GRAPPA parallel imaging reconstruction, channel-by-channel g-factor correction to normalize spatially varying noise, and channel-by-channel Marchenko-Pastur distribution-based principal component analysis (MP-PCA) for denoising of complex signals by utilizing the information redundancy of DWI data across different diffusion encodings (N_{diff}) including b-values/directions/repetitions, Partial Fourier reconstruction, adaptive coil combination, and post-processing to generate averaged trace-weighted DWI and compute ADC maps. ACS: autocalibration scans.

4.2.4 Experiments

In this HIPPA and IRB approved study, 11 male subjects (age: 64±12 years, body-mass index [BMI]: 24.8±6 kg/m^2; prostate-specific antigen [PSA] levels: 5.6±2.4 ng/ml) with clinical suspicion of PCa were recruited and scanned on two 3 T MRI systems using phased-array body coils. 6 subjects were scanned on a standard-bore scanner (Prisma, Siemens, Germany) and 5 subjects were scanned on a wide-bore scanner (Vida, Siemens, Germany). Scanner gradient specifications were reported in the previous section regarding ENCODE sequence design. The imaging protocol consisted of a high-resolution T_2-weighted (T2w) 2D Turbo Spin Echo (TSE) MRI sequence [40]. a standard-resolution (in-plane resolution: 1.6x2.2 mm^2) clinical bipolar single-shot EPI DWI sequence used in the mpMRI protocol [40] in our institution, and the proposed high-resolution (in-plane resolution: 1.0x1.0 mm^2) ENCODE single-shot EPI DWI sequence with identical scan time (TR=4800 ms and 7 measurements for signal averaging) and slice thickness of 3.6 mm as clinical DWI. The detailed imaging parameters for DWI are listed in **Table 4.1**. The number of activated receiver coil channels, automatically determined by the scanner for each subject, ranged from 10 to 20.

4.2.5 Analysis and Evaluations

Residual Properties of RMT Denoising

To validate that the proposed RMT-based denoising and reconstruction pipeline properly removed additive zero-mean Gaussian noise components with minimal removal of anatomical information, one subject was randomly chosen from the study cohort for analysis of the residuals. From this subject, the complex residuals (real and imaginary parts of DWI signals) calculated as the difference between the RMT-based denoising result and the input data across all receiver coil

channels (e.g., 20), all 16 slices, and all diffusion encodings were pooled together (~$5x10^8$ data points) as a set of samples to be compared against a zero-mean Gaussian distribution. After normalization with respect to the estimated noise standard deviation (σ) calculated from all residual samples, the mean and the standard deviation of the residual distribution were reported with 95% confidence intervals.

tSNR Measurements in Prostate Zonal Regions

We quantified the SNR gains using RMT-based denoising for high-resolution ENCODE DWI within the prostate peripheral zone (PZ) and transition zone (TZ). The voxel-by-voxel temporal SNR (tSNR) maps for the acquired 3 scan trace-weighted image with b-value of 800 s/mm^2 using ENCODE DWI and ENCODE DWI with RMT-based denoising ("ENCODE-RMT" DWI) were generated by computing the mean signal over standard deviation of the signals over 7 repetitions (acquired for signal averaging). The standard DWI reconstruction followed the same steps in the RMT-based denoising reconstruction pipeline (**Fig. 4.1**) except that the MP-PCA denoising step was omitted. The mid-gland slice of the prostate, defined as the central slice between the most superior slice containing the prostate base and the most inferior slice containing the prostate apex, was manually segmented into PZ and TZ by a prostate MRI researcher (>6 years of experience) on the standard reconstructed b=0 s/mm^2 DWI while referring to the T2w TSE MRI as an anatomical reference. The segmented PZ and TZ masks were used to extract mean tSNR measurements on the evaluated b=800 s/mm^2 DWI.

CoV of ADC Measurements in Prostate Zonal Regions

We characterized the robustness of ADC measurements in terms of precision within prostate zonal regions. For each of the 7 repetitions (for signal averaging), we used the acquired DWI to compute the ADC map. The coefficient of variation (CoV) of ADC maps over the 7 repetitions was computed by taking the standard deviation of ADC estimates divided by the mean ADC estimates across all 7 repetitions. Similar to region-specific tSNR analysis, the mean of ADC-CoV in prostate PZ and TZ were measured and compared between high-resolution ENCODE DWI and ENCODE-RMT DWI. In addition, ADC-CoV of the standard-resolution clinical bipolar DWI sequence with standard reconstruction was also measured in spatially matched PZ and TZ regions to serve as a reference.

ADC Measurements in Prostate Zonal Regions

To evaluate the accuracy of ADC measurements using high-resolution ENCODE-RMT DWI and ENCODE DWI, the ADC measurements in prostate PZ and TZ were obtained and the agreement with the standard-resolution bipolar DWI reference was assessed.

4.2.6 Statistical Analysis

For noise residual analysis of RMT-based denoising, the relationship between the log probability density of the set of residual samples ($\ln p(r)$) versus the squared sample residual magnitude (r^2) in the range of $r=0\sim4\sigma$ was examined by performing simple linear regression, and the slope of the fitted line was reported. Note that a slope of -0.5 would indicate a perfect zero-mean Gaussian distribution.

For tSNR comparisons between high-resolution ENCODE-RMT DWI and ENCODE DWI, we performed two-sided Wilcoxon signed-rank tests to compare the pair-wise differences in the median measurements over the study cohort (N=11 subjects). For each subject, one mean tSNR measurement per PZ and TZ region at the midgland central slice of the prostate was extracted from ENCODE DWI and ENCODE-RMT DWI and used for statistical analysis. For all statistical comparisons, $P < 0.05$ was considered significant.

For comparisons of ADC-CoV between high-resolution ENCODE-RMT DWI, high-resolution ENCODE DWI, and standard-resolution bipolar DWI, group differences were first tested using the Kruskal-Wallis test. If the Kruskal-Wallis test showed significant differences, then pair-wise differences between each pair of techniques were further evaluated using two-sided Wilcoxon signed-rank tests. The same PZ and TZ regions used in the tSNR analysis (one mean ADC-CoV measurement per PZ and TZ region, per subject) in the subjects were used for the analysis here.

For comparisons of mean ADC measurements in PZ and TZ, Bland-Altman analyses were conducted between high-resolution ENCODE-RMT DWI and standard-resolution bipolar DWI, as well as between high-resolution ENCODE DWI and standard-resolution bipolar DWI, using ADC measurements extracted from the same PZ and TZ regions used in the prior ADC-CoV analysis. The mean differences in zonal ADC measurements and 95% limits of agreement were reported.

4.3 **Results**

4.3.1 Residual Properties of RMT Denoising

Results of denoising residuals were shown in **Figure 4.2**.

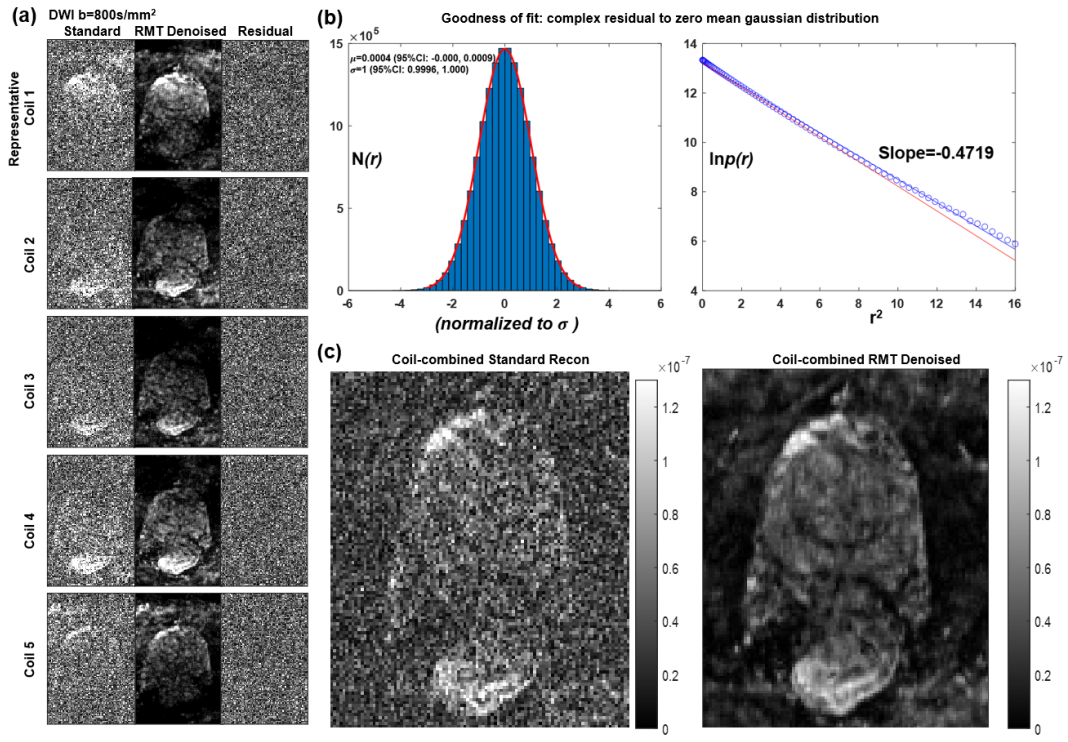

Figure 4.2. Evaluation of channel-wise noise residuals after random matrix theory (RMT)-based denoising of high-resolution ENCODE prostate DWI. **(a)** Comparison between results from ENCODE DWI using standard reconstruction and RMT-based denoising for individual coil channels. Results for DWI at b=800 s/mm^2 (x direction) from 5 representative coils and the associated residuals (magnitude of the complex residual) are shown. **(b)** Goodness of fit for the complex residual data samples (real and imaginary parts pooled together) across all coils and slices for a zero-mean Gaussian distribution. The red reference line (slope = -0.5) indicates the ideal Gaussian distribution. **(b)** Comparison of the adaptive coil-combined DWI at b=800 s/mm^2 using standard reconstruction and RMT-based denoising.

From the per-coil channel denoising residuals, there were no identifiable anatomical details, providing evidence that the proposed denoising pipeline did not remove tissue information. After fitting the pooled real and imaginary parts of the residuals to a Gaussian distribution, the distribution mean was μ=0.0004 (95% CI=[-0.000,0.009]) and the normalized standard deviation was 1 (95% CI=[0.9996, 1]). The linear regression analysis of the log probability density of

residual samples (ln*p(r)*) versus the squared sample residual magnitude (r^2) in the range of r=0~4σ yielded a line with slope = -0.4719 (blue line), which was close to a perfectly zero-mean Gaussian distribution with slope = -0.5 (red line). The fitted blue line had a close agreement with the reference red line in the range of r=0~3σ (r^2=0-9), and only started to deviate slightly beyond 3σ, showing that the residuals after denoising achieved a close agreement with the zero-mean Gaussian noise statistics assumed by RMT.

4.3.2 Effects of RMT Denoising on Reconstructed DWI

A representative example showing the qualitative effects of RMT-based denoising for high-resolution ENCODE DWI at different b-values and associated ADC maps is shown in **Figure 4.3a**. The effects of denoising were most apparent for the higher b-values of 400 s/mm^2 and 800 s/mm^2; DWI with b=400 and 800 s/mm^2 appeared noisy after standard reconstruction, while RMT-based denoising yielded visually clear and sharp DWI at all b-values. This example also illustrated the downstream effects of noise suppression with RMT-based denoising, which led to improvements in the fitted ADC maps, as ADC in prostate TZ appeared brighter (higher ADC values due to reduced noise floor in DWI [109]). and reduced noise propagation into the calculated high b-value DWI of b=1400 s/mm^2 compared to standard reconstruction.

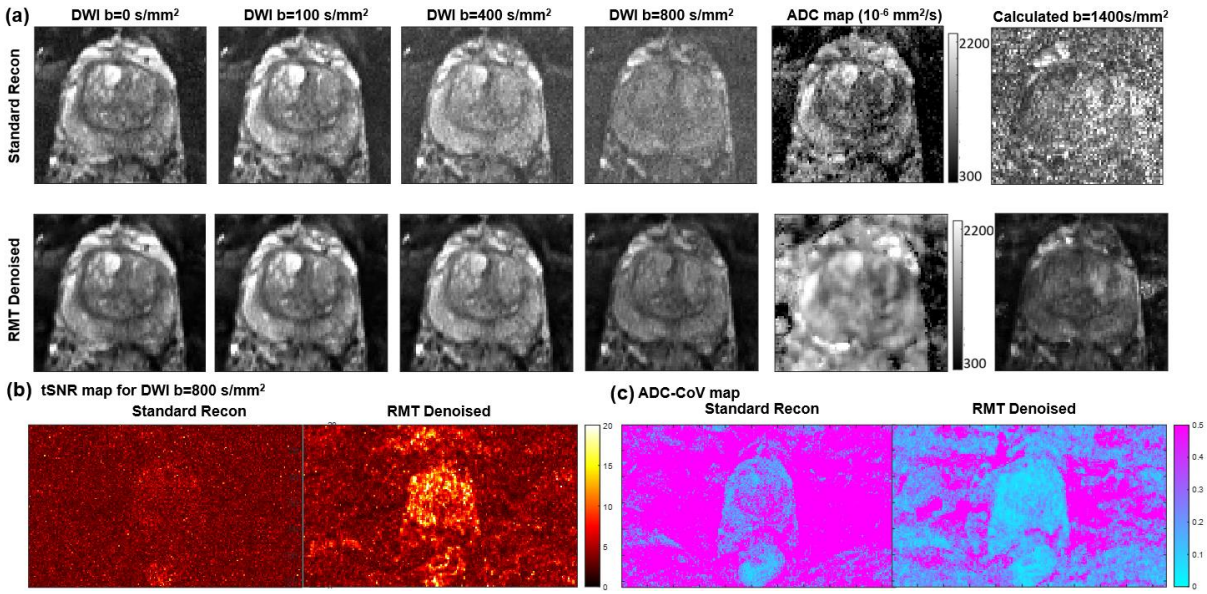

Figure 4.3. **(a)** Comparison of high-resolution (1.0x1.0 mm^2) ENCODE prostate DWI at 4 b-values, ADC maps, and calculated high b-value (1400 s/mm^2) DWI using standard reconstruction and RMT-based denoising. **(b)** The temporal signal-to-noise ratio (tSNR) maps over 7 repetitions (signal averages) for b=800 s/mm^2 using standard reconstruction and RMT-based denoising for high-resolution ENCODE DWI. **(c)** The coefficient of variation (CoV) maps of the ADC, calculated over 7 repetitions, for high-resolution ENCODE DWI using standard reconstruction and RMT-based denoising and ENCODE DWI for clinical standard and higher-resolution protocols. The regions of interest for measuring SNR are denoted as orange circles on DWI in (a). ENCODE achieved significantly higher SNR than BIPOLAR for all three prostate DWI protocols.

4.3.3 tSNR Measurement in Prostate Zonal Regions

Representative comparisons of tSNR maps for high-resolution ENCODE DWI and ENCODE-RMT DWI are shown in **Figure 4.3b**. Quantitative results of tSNR differences between high-resolution ENCODE-RMT DWI and ENCODE DWI at b=800 s/mm^2 are shown in **Figure 4.4a**. ENCODE-RMT DWI yielded 103% and 91% higher median tSNR in PZ and TZ, respectively (PZ tSNR: 7.87 vs. 3.87, P<0.001; TZ tSNR: 6.93 vs. 3.63, P<0.001), for DWI at b=800 s/mm^2 compared to ENCODE DWI.

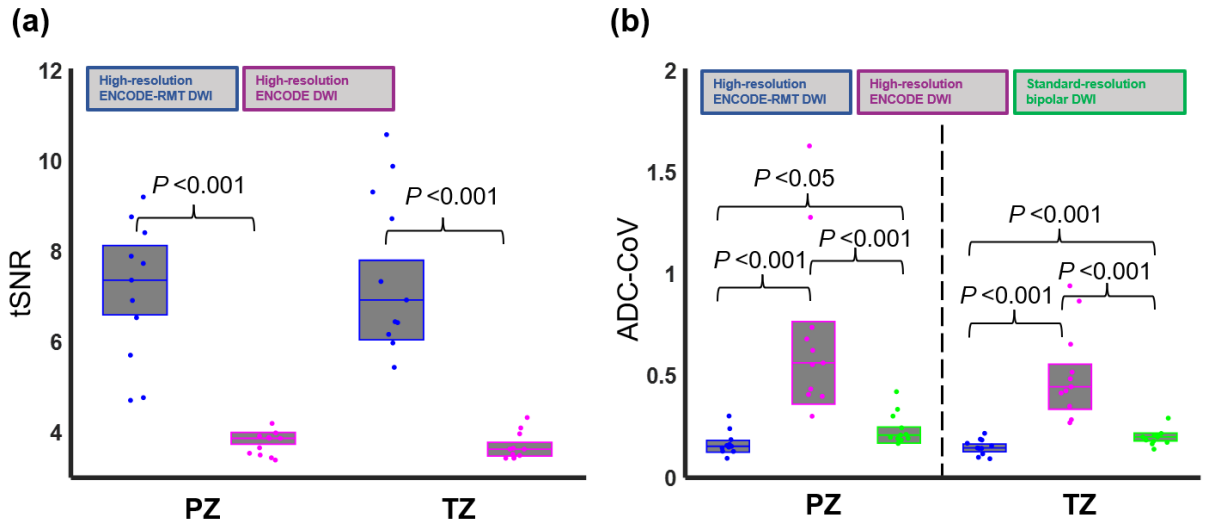

Figure 4.4. **(a)** Comparison of mean tSNR of b=800 s/mm^2 high-resolution ENCODE DWI in the prostate peripheral zone (PZ) and transition zone (PZ) using standard reconstruction and RMT-based denoising in 11 subjects. **(b)** Comparison of the mean ADC-CoV across 7 repetitions in prostate PZ and TZ for high-resolution (1.0x1.0 mm^2) ENCODE DWI using standard reconstruction and RMT-based denoising, as well as standard-resolution (1.6x2.2 mm^2) bipolar DWI with standard reconstruction, in 11 subjects.

4.3.4 CoV of ADC Measurements in Prostate Zonal Regions

Representative ADC-CoV maps for high-resolution ENCODE DWI and ENCODE-RMT DWI are shown in **Figure 4.3c**. The overall results of ADC-CoV for high-resolution ENCODE DWI and ENCODE-RMT DWI, along with standard-resolution bipolar DWI, are shown in **Figure 4.4b**. High-resolution ENCODE-RMT DWI reduced ADC-CoV with respect to ENCODE DWI by 41% and 30% in the PZ and TZ, respectively (PZ ADC-CoV: 0.15 vs. 0.56, P<0.001; TZ ADC-CoV: 0.14 vs. 0.44, P<0.001), while also achieving lower ADC-CoV than standard-resolution bipolar DWI in PZ and TZ, respectively (PZ ADC-CoV: 0.15 vs. 0.20, P<0.05; TZ ADC-CoV: 0.14 vs. 0.20, P<0.001).

4.3.5 ADC Measurements in Prostate Zonal Regions

Representative examples of DWI and ADC maps from high-resolution ENCODE DWI and ENCODE-RMT DWI, as well as standard-resolution bipolar DWI, are shown in **Figure 4.5a**. Similar to the example in **Figure 4.3a**, there was noticeable noise reduction, especially for high-resolution ENCODE-RMT DWI with b-value of 800 s/mm^2 compared to ENCODE DWI. At the same time, the ADC map appeared darker (lower values) in the prostate TZ for high-resolution ENCODE DWI. After applying RMT-based denoising, the high-resolution ENCODE-RMT DWI ADC map became more consistent with the standard-resolution bipolar DWI ADC map, compared to high-resolution ENCODE DWI.

Figure 4.5b shows the averaged DWI signal decay curves from three techniques in prostate PZ and TZ. The mean signal decay of high-resolution ENCODE-RMT DWI was similar to the signal decay of standard-resolution bipolar DWI, with marked signal reduction at b=800 s/mm^2. On the other hand, high-resolution ENCODE DWI was affected by the noise floor effect and exhibited apparent elevation of signal at at b=800 s/mm^2. This explains why the high-resolution ENCODE ADC values increased after RMT-based denoising - reducing the noise floor at high b-values will lead to higher ADC estimates through mono-exponential signal decay fitting [109].

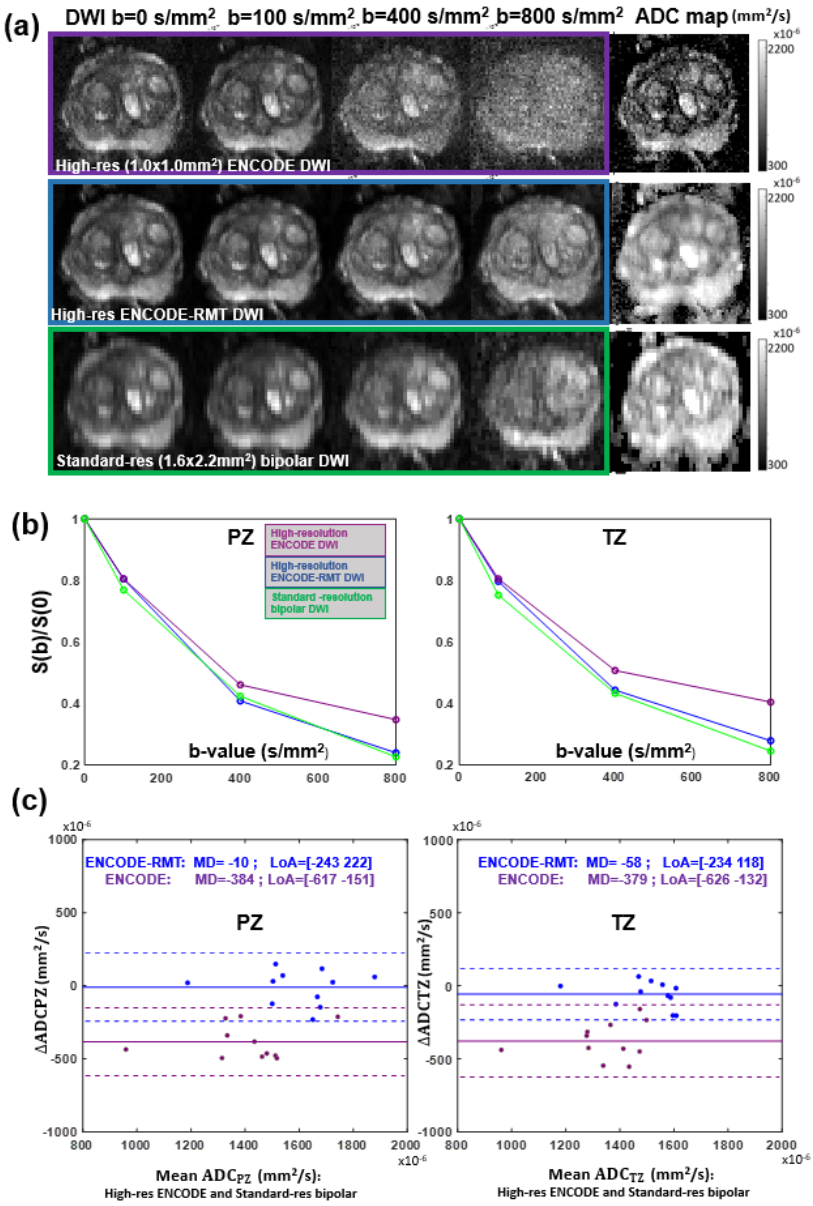

Figure 4.5. **(a)** Comparison between high-resolution ENCODE, high-resolution ENCODE-RMT, and standard-resolution bipolar DWI and ADC map. **(b)** The mean diffusion-weighted signal decay curves averaged over prostate peripheral zone (PZ) and transition zone (TZ) pixels from the three techniques in the example subject. Note that the effects of the noise floor on high-resolution ENCODE DWI were addressed using RMT-based denoising. **(c)** Bland-Altman analysis of the agreement of zonal ADC measurements across 11 subjects between high-resolution ENCODE DWI and ENCODE-RMT DWI and the reference standard-resolution bipolar DWI.

Bland-Altman analysis of the ADC measurements from different DWI methods is shown in **Figure 4.5c**. The high-resolution ENCODE-RMT ADC achieved closer agreement with standard-resolution bipolar ADC in both prostate PZ and TZ, with smaller mean differences (MD) (PZ ADC MD: -10x10^{-6} mm^2/s; TZ ADC MD: -58x10^{-6} mm^2/s) and tighter 95% limits of agreement (LoA) (PZ ADC LoA: [-243 222] x10^{-6} mm^2/s; TZ ADC LoA: [-234 117] x10^{-6} mm^2/s), compared to high-resolution ENCODE ADC, which had larger MD (PZ ADC MD: -384x10^{-6} mm^2/s; TZ ADC MD: -379x10^{-6} mm^2/s) and 95% LoA (PZ ADC LoA: [-617 -151] x10^{-6} mm^2/s; TZ ADC LoA: [-629 -131] x10^{-6} mm^2/s) vs. bipolar ADC.

Lastly, Additional representative examples of high-resolution ENCODE-RMT prostate DWI and standard-resolution bipolar DWI, along with a T2w 2D TSE MRI anatomical reference, are shown in **Figure 4.6**.

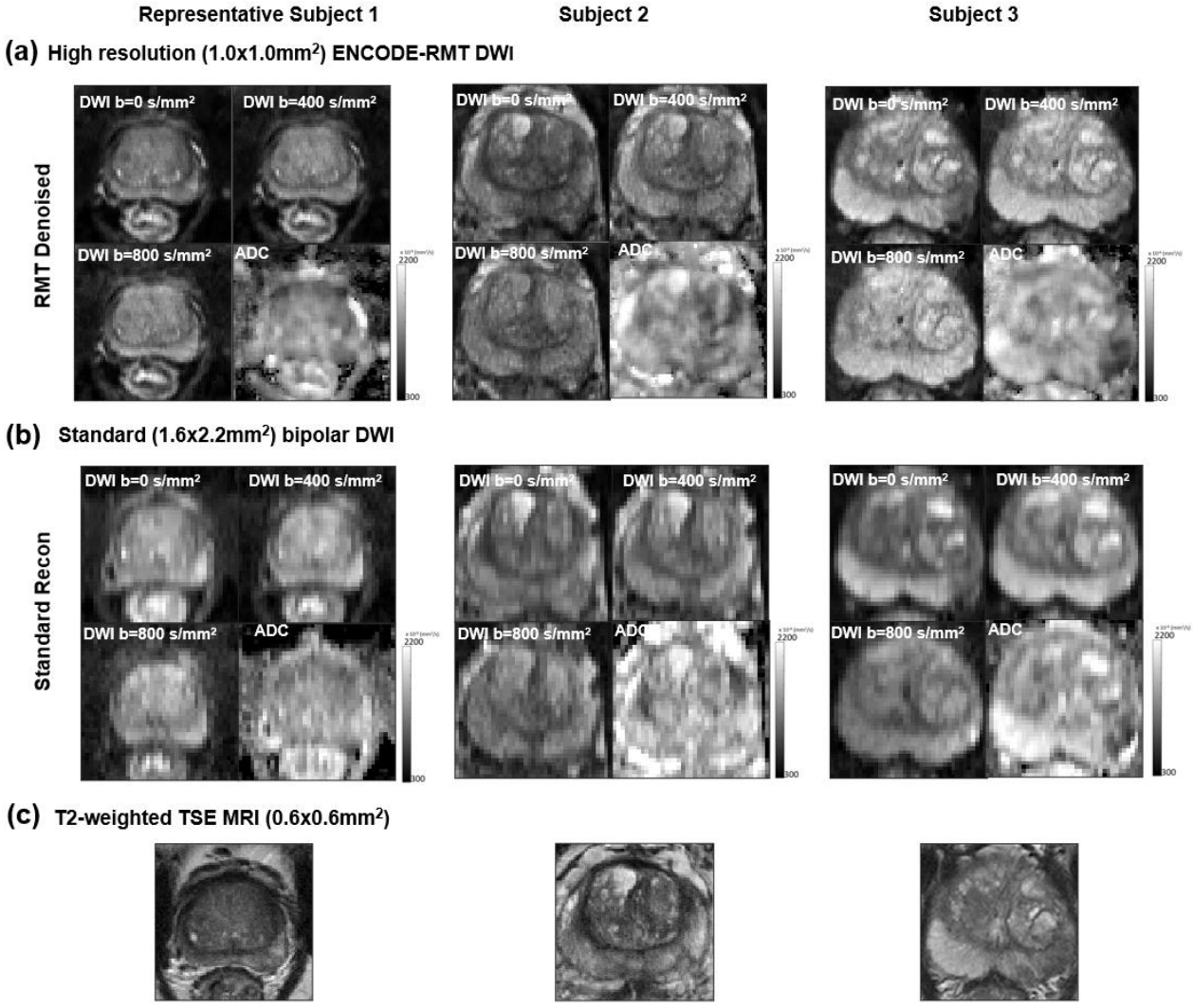

Figure 4.6 Representative examples from three subjects (subject 1: BMI=26 kg/m^2, PSA=2.2 ml, standard-bore scanner; subject 2: BMI=22 kg/m^2, PSA=6.4 ng/ml, standard-bore scanner; subject 3: BMI=25 kg/m^2, PSA=8.8 ng/ml, wide-bore scanner). **(a)** High-resolution (1.0x1.0 mm^2) ENCODE-RMT prostate DWI. **(b)** Clinical standard-resolution (1.6x2.2 mm^2) bipolar prostate DWI. **(b)** High-resolution (0.6x0.6 mm^2) 2D T_2-weighted TSE MRI anatomical reference.

4.4 Discussion

The SNR of high-resolution DWI can be improved from both acquisition (e.g. diffusion encoding and TE) and reconstruction perspectives. For the most commonly used single-shot EPI DWI sequence, once the imaging parameters such as resolution, FOV, and maximum b-value are determined, the achievable SNR mainly depends on the TE of the sequence, which in turn is determined by the diffusion encoding waveforms. For the evaluated protocol, ENCODE reduced TE by ~20 ms compared to twice-refocused bipolar DWI, which translated to 30%-40% SNR gains based on reduced T_2 signal decay [97]. This meant if bipolar diffusion encoding waveforms were employed, the baseline tSNR in TZ and PZ for DWI at b=800 s/mm^2 would be ~2.7 (vs. 3.5 using ENCODE). Assuming the relative SNR gains provided by RMT-based denoising would be similar, the RMT-denoised bipolar DWI would still have lower SNR than ENCODE-RMT DWI and may not achieve the same level of ADC precision (in terms of CoV) as the standard-resolution DWI reference. While DWI using monopolar diffusion waveforms has similarly short TE as ENCODE, monopolar DWI has the limitation of introducing eddy current-induced directionally dependent prostate distortion artifacts, which impacts the geometric fidelity of prostate DWI [97,110,111] unless dedicated post-processing algorithms are applied to correct for the misregistration of prostate tissue across DWI directions [111]. However, the application of post-processing algorithms for eddy current correction may interfere with the performance of MP-PCA denoising as non-rigid registration can distort the spatial noise statistics [112], and violate the assumptions in RMT. Thus, the specific combination of TE-minimized ENCODE waveforms with RMT-based denoising is a compelling strategy to enhance the SNR of high-resolution prostate DWI while maintaining the geometric fidelity of the prostate.

The RMT-based denoising and reconstruction pipeline developed in this study was built upon the original MP-PCA algorithm [31], and incorporated state-of-the-art technical developments addressing the limitations of Rician noise floor effects in magnitude-based MRI by using complex DWI datasets [99-101,106] and applied noise normalization to resolve the channel-dependent spatially-varying noise amplification effects introduced by parallel imaging reconstruction [101]. The use of complex data and coil-by-coil g-factor map normalization before MP-PCA theoretically maintained the i.i.d. zero-mean Gaussian noise characteristics assumed in RMT to separate noise and signal components [66,30]. Our noise residual analysis results showed that the residuals had a close agreement with a zero-mean Gaussian distribution, therefore demonstrating the effectiveness of the proposed pipeline for specifically removing noise. Since the evaluated prostate DWI datasets had anisotropic spatial resolution (in-plane: 1.0x1.0 mm^2; slice thickness: 3.6 mm), a local 2D spatial kernel including adjacent voxels, instead of a 3D spatial kernel (commonly used in high-resolution isotropic brain DWI datasets), was used along with the diffusion encoding dimension to form locally low-rank matrices for MP-PCA denoising. The quantitative tSNR analysis showed an average increase of 2-fold in PZ and TZ after denoising, which was similar to results reported in recent high-resolution brain DWI studies using RMT-based denoising [101,100,113]. Our results demonstrated that RMT-based denoising can also markedly improve SNR for high-resolution prostate DWI, despite having substantially different data acquisition conditions compared to brain DWI, such as anisotropic resolution and intrinsically lower prostate SNR using phased-array body coils.

For the ADC precision analysis, we used the CoV of ADC of the standard-resolution bipolar DWI sequence as a performance benchmark. The study design is based on the experience that the bipolar DWI sequence and associated ADC maps have demonstrated stable performance both

qualitatively and quantitatively in aiding the detection, diagnosis, and risk stratification of PCa as part of the clinical mp-MRI protocol of our institution [40]. Our results showed that high-resolution ENCODE-RMT DWI actually achieved a slightly lower ADC-CoV compared to standard-resolution bipolar DWI, which demonstrated that ENCODE-RMT achieved the required level of ADC precision for prostate imaging.

To evaluate the ADC accuracy of the high-resolution ENCODE-RMT DWI, we also used the standard-resolution clinical bipolar DWI sequence at our institution as a reference. A perfect agreement was not expected between ADC measurements using different techniques even when the noise bias effects are addressed using denoising, as there are differences in TE caused by different spatial resolution parameters and diffusion encoding. Based on previous experimental and theoretical studies reporting the ADC dependency on TE and diffusion time [97,19,114,69] and the understanding that multiple microscopic tissue compartments in prostate tissue have distinct compartmental T_2 and ADC [15,19,114,96], a $\leq$20% difference in ADC between bipolar DWI (TE=80 ms) and ENCODE DWI (TE=66 or 73 ms) estimated using a mono-exponential signal model was expected. The absolute limits of agreement for ADC (117~243 $x10^{-6}$ mm^2/s) using high-resolution ENCODE-RMT DWI were consistent with the expected difference in ADC and achieved substantially better agreement than the high-resolution ENCODE DWI with standard reconstruction.

Our high-resolution ENCODE-RMT prostate DWI technique made distinct contributions regarding both acquisition and reconstruction to extend the nascent area of high-resolution (e.g. in-plane $\leq$1.0x1.0 mm^2) prostate DWI [11,60,10]. Prior high-resolution prostate DWI studies that used phased array coils (without an endorectal coil) mostly employed a maximum diffusion weighting with a moderate b-value of 500~600 s/mm [11,60], while our study employed a

maximum b-value of 800 s/mm^2, which was consistent with the up-to-date Prostate Imaging – Reporting and Data System (PI-RADS) v2.1 recommendation that the acquired b_{max} should be 800~1000 s/mm^2 [39] to achieve sufficient sensitivity for low diffusivity prostate tissue such as PCa. The combination of smaller voxels and higher diffusion weighting (b-value) incurs a stronger SNR penalty for prostate DWI. Our technique combined ENCODE with RMT-based denoising to overcome this more challenging imaging condition and achieve better ADC precision than standard-resolution clinical DWI with no increase in scan time. An earlier study employing an endorectal coil for high-resolution prostate DWI found no apparent SNR and image quality degradation when halving the voxel size for prostate DWI [10], which was different from the qualitative and quantitative findings in our study, where b=800 s/mm^2 DWI using a phased-array body coil had low tSNR <5 without denoising. This was expected as acquisitions with a phased-array body coil have substantially lower SNR than scans using an endorectal coil. Therefore the use of an advanced denoising reconstruction method such as the proposed RMT-based method is critical to address the SNR challenge for high-resolution prostate DWI.

Recently, advanced denoising methods such as MP-PCA [98], and deep neural networks [115] , have been evaluated for enhancing the SNR of prostate DWI acquired at standard resolution (e.g. 1.6 to 2.0 mm in-plane), and showed promise for reducing the scan time of clinical DWI protocols by reducing the number of required averages for each b-value [115,98]. Our study, which specifically focused on evaluating RMT-based denoising for improving the SNR of high-resolution (in-plane: 1.0x1.0 mm^2) prostate DWI, showed that advanced denoising could also be valuable for enhancing the spatial resolution and structural details of prostate DWI while maintaining SNR and ADC quantification robustness without increasing scan time.

Limitations

Our study had limitations. First, due to the limited sampled size and the lack of biopsy-confirmed PCa diagnosis in all of the subjects, we did not perform lesion detection and diagnostic performance analysis of the proposed high-resolution ENCODE-RMT prostate DWI in comparison with standard-resolution clinical prostate DWI. The purpose and scope of this study were to evaluate the technical performance of the proposed technique in terms of SNR and ADC mapping. Our results from this technical evaluation will serve as the foundation to further explore the potential benefits of high-resolution prostate DWI for PCa diagnosis. Second, in this study we only evaluated high-resolution ENCODE DWI using a single-shot EPI sequence with rFOV acquisition. Right now, there are alternative emerging sequences, such as readout-segmented (rs) EPI DWI [58], and diffusion-prepared bSSFP DWI [11], for achieving high spatial resolution. The choice to focus on single-shot EPI DWI was based on the fact that it remains the most widely available and commonly used DWI sequence in clinical and research settings, including for the investigation of high-resolution DWI [100,101,108]. In addition, single-shot EPI has high scan efficiency (2- to 10-fold faster acquisition per image compared to rs-EPI or diffusion-prepared bSSFP [11,14,58], which facilitates RMT-based denoising methods as MP-PCA requires a large number of diffusion encodings (>30) to achieve sufficient redundancy in the multi-dimensional DWI dataset for separating signal from noise components. The evaluation of ENCODE and RMT-based denoising for alternative DWI sequences could be a direction for future research.

4.5 **Conclusion**

Combining ENCODE diffusion encoding waveforms with minimized TE and random matrix theory-based denoising improved the signal-to-noise ratio of high-resolution (in-plane 1.0x1.0 mm^2) prostate DWI, and consequently achieved accurate and precise ADC measurements in the prostate. This technical validation study paves the way for future studies to evaluate the potential benefits of high-resolution prostate DWI for the detection and diagnosis of PCa.

Chapter 5 **Prostate Microstructure in Prostate Cancer Using 3T MRI with Diffusion-Relaxation Correlation Spectrum Imaging: Validation to Whole-Mount Digital Histopathology**

5.1 **Introduction**

Multiparametric MRI is an important tool for the diagnosis of prostate cancer (PCa) [2,46]. However, multiparametric MRI using PI-RADS interpretation still misses PCa in up to 45% of men and faces challenges in distinguishing clinically significant PCa from indolent PCa [40,46]. Thus, histopathological examination of PCa remains the reference standard. Based on the microscopic appearance of PCa, a Gleason score (GS) is assigned to indicate its aggressiveness [17].

Diffusion-weighted MRI (DWI) is a critical component of multiparametric MRI and is sensitive to tissue microstructure changes in PCa [94]. However, current clinical analysis using a mono-exponential signal model to calculate apparent diffusion coefficients (ADC) has limited ability to characterize PCa aggressiveness [15], since PCa is associated with alterations in multiple microscopic tissue compartments [70]. To improve the characterization of PCa, microstructural MRI techniques are being developed, including luminal water imaging [21] , VERDICT (Vascular, Extracellular and Restricted Diffusion for Cytometry in Tumors) [20], and hybrid multidimensional MRI [22].

The recently developed Diffusion-Relaxation Correlation Spectrum Imaging (DR-CSI) method has potential for characterizing prostate microstructure with reduced model bias compared to previous techniques [32,116]. Instead of assuming a pre-determined number of components, DR-CSI quantifies a spectrum of T_2 relaxation and diffusivity (D) components that contribute to

the overall MRI signal in each voxel, and generates signal component fraction maps by integrating the spectral peaks on the voxel-wise T_2-D spectra [32,116].

The purpose of this study was to validate DR-CSI for quantifying microscopic tissue compartments in *ex vivo* prostate specimens from men with PCa using digital histopathology as reference, and to evaluate the differences between DR-CSI signal component fractions in regions of prostate cancer versus benign tissue.

5.2 **Methods**

5.2.1 Study Design

This prospective, HIPAA-compliant study was approved by our IRB and biosafety committee, with written informed consent obtained from each participant. Between June 2018 and January 2019, fresh whole prostate specimens were obtained from 9 consecutive men with PCa who had pre-surgical prostate MRI and underwent robotic-assisted radical prostatectomy with a schedule permitting *ex vivo* MRI. Following prostatectomy (within 15-35min), *ex vivo* MRI was performed on the prostate specimens using a 3T whole-body scanner (Prisma, Siemens, Erlangen, Germany) before whole mount histopathology (WMHP) processing. A total of 59 WMHP slices from all subjects (on average 7 slices per subject) were generated for analysis. Registration between *ex vivo* MRI and WMHP enabled region-based comparisons between DR-CSI and digital histopathology (**Figure 5.1**).

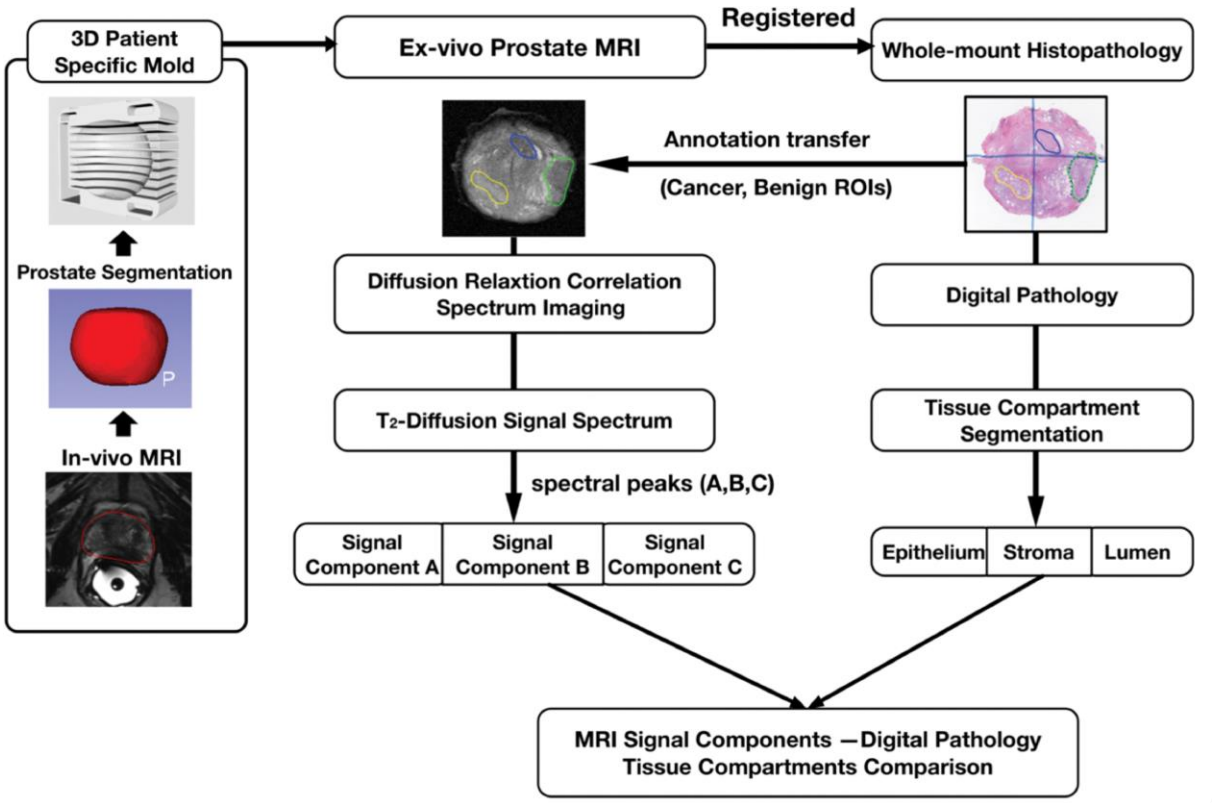

Figure 5.1. Overview of study design and analysis. 3D-printed patient-specific molds were designed using pre-surgical *in vivo* MRI prostate segmentation. Immediately after radical prostatectomy, *ex vivo* MRI was performed with the prostate specimen in the mold, including diffusion-relaxation correlation spectrum imaging (DR-CSI). After completing *ex vivo* MRI, the prostate specimen was sliced inside the mold to create whole-mount histopathology (WMHP) slides corresponding to MRI slice locations. The WMHP tissue compartment area fractions calculated by digital histopathology software were compared with DR-CSI signal component fractions.

5.2.2 Ex Vivo Prostate MRI

The prostate specimen was placed inside a 3D-printed patient-specific mold for *ex vivo* MRI using a 15-channel knee coil [88]. The molds had slits and fiducial markers to aid alignment of *ex vivo* MRI slices to the subsequently sectioned WMHP slices (**Figure 5.1**). A high-resolution T_2-weighted MRI sequence, a conventional DWI sequence, and the DR-CSI sequence were acquired.

DR-CSI was implemented using a modified 2D single-shot spin-echo diffusion-weighted echo-planar imaging sequence to acquire 16 combinations of TE and b-values (TE=60-120 ms; b-values=0-1500 s/mm^2) in 12 minutes (parameters in **Table 5.1**).

Sequences*	FOV (mm^2)	Voxel Size (mm^3)	b values (s/mm^2)	Diffusion Directions	TE (ms)	Averages	Scan Time
DR-CSI	160×80	1.0×1.0×4.5	0, 400, 800, 1500	3 Scan Trace	60, 80, 100, 120	1	12 min
DWI					60	7	6 min

Table 5. 1:
Summary of sequence and imaging parameters used in *ex vivo* prostate 3T MRI with diffusion-relaxation correlation spectrum imaging (DR-CSI) and conventional diffusion-weighted imaging (DWI) sequences. DR-CSI acquisition included 4x4 (in total 16) combinations of echo time (TE) and b-values, while conventional DWI acquired 4 b-values with a single TE. FOV: field of view. *Common parameters for all protocols included: slice thickness = 4.5 mm, 20 slices, repetition time (TR) = 5000 ms, parallel imaging factor = 2, partial Fourier factor =6/8.

5.2.3 DR-CSI Microstructure Modeling

DR-CSI modeled the MRI signal at each voxel as a summation of continuous exponential decay functions characterized by T_2 and D [32].

$$S(x,y,TE,b) = \iint w(x,y,T_2,D)\exp\left(-\frac{TE}{T_2}\right)\exp(-bD)dT_2dD = Lw \qquad (5.1)$$

where *S(x,y,TE,b)* represents the voxel-wise measured signals with each TE-b encoding, *w(x,y,T_2,D)* represents the voxel-wise T_2-D spectra to be reconstructed, and *L* represents the Laplace Transform.

To solve for $w(x,y,T_2,D)$, non-negativity (i.e., $w(x,y,T_2,D)\geq 0$) and spatial total variation (TV_{xy}), constraints were applied [32]:

$$w = \text{argmin } \|S - Lw\|_F^2 + TV_{xy}(w), \text{subject to } w \geq 0. \quad (5.2)$$

Each peak in voxel-wise T_2-D spectra represented an individual signal component. The signal component fractions (e.g. f_A, f_B, f_C, if three peaks A, B, C exist on T_2-D spectra) for a voxel or spatial region were calculated by integrating each spectral peak on the voxel-wise or region-averaged T_2-D spectra followed by normalization.

For example, to calculate f_A:

$$f_A(x,y) = \frac{\int_{\textbf{Area under peak A}} w(x,y,T_2,D)dT_2dD}{\int_{\textbf{entire } (\boldsymbol{T_2}-\textbf{D})\textbf{space}} w(x,y,T_2,D)dT_2dD} \quad (5.3)$$

5.2.4 DR-CSI Signal-to-Noise Ratio Analysis

The lower-bound of DR-CSI signal-to-noise ratio was assessed at TE=120 ms and b-value=1500 s/mm^2 for one average, using two repeated acquisitions in one prostate specimen. The signal-to-noise ratio across apical, mid-gland and basal planes were reported (mean ± standard deviation [SD]).

5.2.5 Whole-Mount Digital Histopathology Analysis

After imaging, the prostate specimen was sectioned along the mold slits. The slides were stained with hematoxylin and eosin, and digitized on an optical microscope (Aperio Technologies, Vista, California) at 0.5x0.5μm^2 resolution. A genitourinary pathologist (A.S.; 5 years of experience), blinded to the MRI, contoured all PCa foci on WMHP slides and assigned Gleason scores to them. For each PCa region of interest (ROI) in the transition zone (TZ) or peripheral zone (PZ), a

corresponding benign tissue ROI in the same zone with similar size and shape was defined, by first reflecting the PCa ROI to the contralateral side of the prostate, and then adjusting the reflected ROI to exclude tissues in other zones or PCa. Non-rigid registration was performed to map ROIs from WMHP onto corresponding *ex vivo* MRI slices [88].

Digital histopathology software (Tissue Studio 4.1, Definiens, Munich, Germany) was used by a pathology researcher to segment WMHP into epithelium, stroma, and lumen masks, and to quantify the tissue area fractions ($f_{epithelium}$, f_{stroma}, f_{lumen}) in the ROIs (**Figure 5.2**).

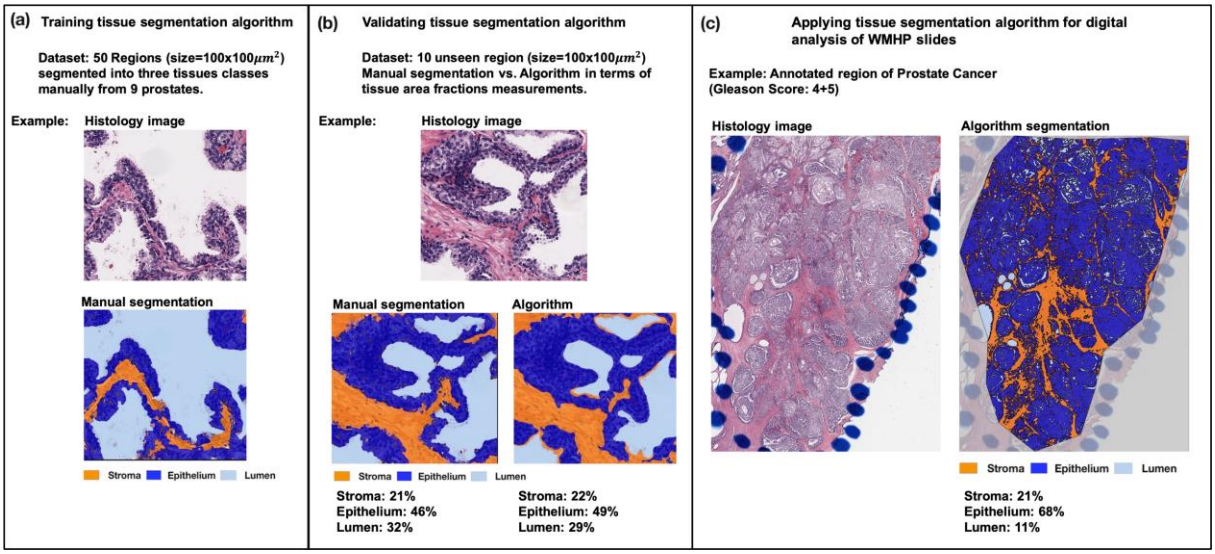

Figure 5.2. Illustration of the training, validation, and application of the tissue compartment segmentation algorithm for digital analysis of prostate whole-mount histopathology (WMHP) slides. **(a)** Example of a region manually segmented into epithelium, stroma, and lumen classes by a pathology researcher for training the tissue segmentation algorithm. **(b)** Example comparing the tissue area fraction measurements of epithelium, stroma, and lumen from manual segmentation and algorithm segmentation for validating the tissue segmentation algorithm. **(c)** Example of a prostate cancer lesion with Gleason score 4+5 processed by the trained algorithm to measure tissue area fractions of epithelium, stroma and lumen.

Using the "composer" tool, the pathology researcher independently trained classifiers using 50 regions (size: 100x100 μm^2) on WMHP selected from 9 prostates that were segmented manually

into epithelium, stroma and lumen classes. Using the "tissue detection" function, the trained classifiers segmented the annotated PCa and benign tissue ROIs into epithelium, stroma and lumen masks and calculated the corresponding area fractions ($f_{epithelium}$, $f_{stroma,}$ f_{lumen}). The reliability of the segmentation algorithm was assessed on 10 unseen regions (100x100 μm^2, 3 containing PCa), and the tissue area fractions measured by the algorithm were found to be linearly correlated ($P<0.001$) with manual segmentation with a slope of 0.92 (epithelium, stroma, and lumen combined).

5.2.6 Statistical Analysis

DR-CSI Signal Components in Prostates

Slice-averaged T_2-D spectra were calculated from each slice in 9 prostates, and the number of spectral peaks were counted. The peak locations were reported (mean ± standard deviation [SD]).

Histopathology and DR-CSI Differences between PCa and Benign tissues

The histopathology parameters ($f_{epithelium}$, $f_{stroma,}$ f_{lumen}) were compared in the PCa and benign tissue ROIs on WMHP for 40 ROIs. The DR-CSI signal component fractions (f_A, f_B, f_C) were also compared in corresponding ROIs for the TZ and PZ. Two-sided t tests were used to assess the differences between ($f_{epithelium}$, $f_{stroma,}$ f_{lumen}) and (f_A, f_B, f_C) of PCa and benign tissues, for the TZ and PZ combined together. For sub-analysis, the specific histopathology and DR-CSI parameters that showed significant differences in the combined TZ and PZ analysis were further tested using one-way analysis of variance followed by post-hoc Tukey honest test in PZ and TZ separately.

Correlation between DR-CSI Signal Components and Microscopic Tissue Compartments

The correlations between DR-CSI and histopathology parameters (e.g. f_A vs. $f_{epithelium}$) in 40 ROIs were first determined using a linear mixed-effects model that accounted for multiple ROIs per subject. The histopathology parameters were designated as fixed effects and subjects as a random effect on the intercept [117,118]. The slope was tested against zero using a two-tailed t test and P values were reported. Next, to assess the strength of the correlations, Spearman's correlation coefficients (ρ) were computed between (f_A, f_B, f_C) and ($f_{epithelium}$, f_{stroma}, f_{lumen}). The 95% confidence interval (CI) of the Spearman's correlation coefficients was computed by drawing 2000 random bootstrap samples with replacement to account for multiple ROIs per subject [118,117]. The correlation between the ADC derived from DWI and ($f_{epithelium}$, f_{stroma}, f_{lumen}) was also evaluated.

5.3 **Results**

5.3.1 Participant Characteristics

Nine prostates from nine men (mean age, 65 years ±7) were evaluated. Participant characteristics are summarized in **Table 5.2**.

Participant	Age (years)	PSA (ng/ml)	Gleason score	Volume (cc)	Weight (g)	Number of WMHP	Number of PCa foci
1	61	8.3	4+5	49	47	8	2
2	71	5.0	3+4	60	50	7	2
3	65	5.6	4+3	70	62	6	1
4	67	2.4	3+4	39	32	7	2
5	51	4.9	3+4	27	34	7	2
6	74	3.7	3+4	47	41	8	2
7	60	8.2	4+5	45	41	4	2
8	66	10	3+4	41	35	5	2
9	70	9.3	3+4	33	35	7	2
Mean ± SD	65±7	6.4±2.7	N/A	45.7±13	42±9.7	6.6±1.3	1.9±0.3

Table 5.2:

Participant characteristics. For each man participating in the study, the following are reported: age in years; prostate specific antigen (PSA) level in ng/ml; final pathology Gleason Score of the index prostate cancer (PCa) lesion; prostate volume in cc; prostate specimen weight in g, the number of whole-mount histopathology (WMHP) slides created for analysis; the number of PCa lesions detected on WMHP. SD represents standard deviations.

5.3.2 DR-CSI Signal-to-Noise Ratio:

The signal-to-noise ratio of DR-CSI at TE=120 ms and b-value= 1500 s/mm^2 for one average was 18.1± 2.0 across the prostate apex, mid-gland and base.

5.3.3 DR-CSI Signal Components

Across all slices and subjects (**Figure 5.3**), 3 distinct DR-CSI signal components (spectral peaks A, B and C) were consistently identified, with peak locations (T_2, D): A=(70±5 ms, 215±20x10^{-6} mm^2/s), B=(50±10 ms, 922±110x10^{-6} mm^2/s), and C=(145±10 ms, 1990±183x10^{-6} mm^2/s). Therefore, we divided the entire T_2-D spectral space into three areas (**Figure 5.4c**): peak A ∈ [$T_2 \leq$150 ms, D<500 x10^{-6} mm^2/s], peak B ∈ [T_2<80 ms, D≥500 x10^{-6} mm^2/s], and peak C ∈ [$T_2 \geq$ 80 ms, D≥500 x10^{-6} mm^2/s].

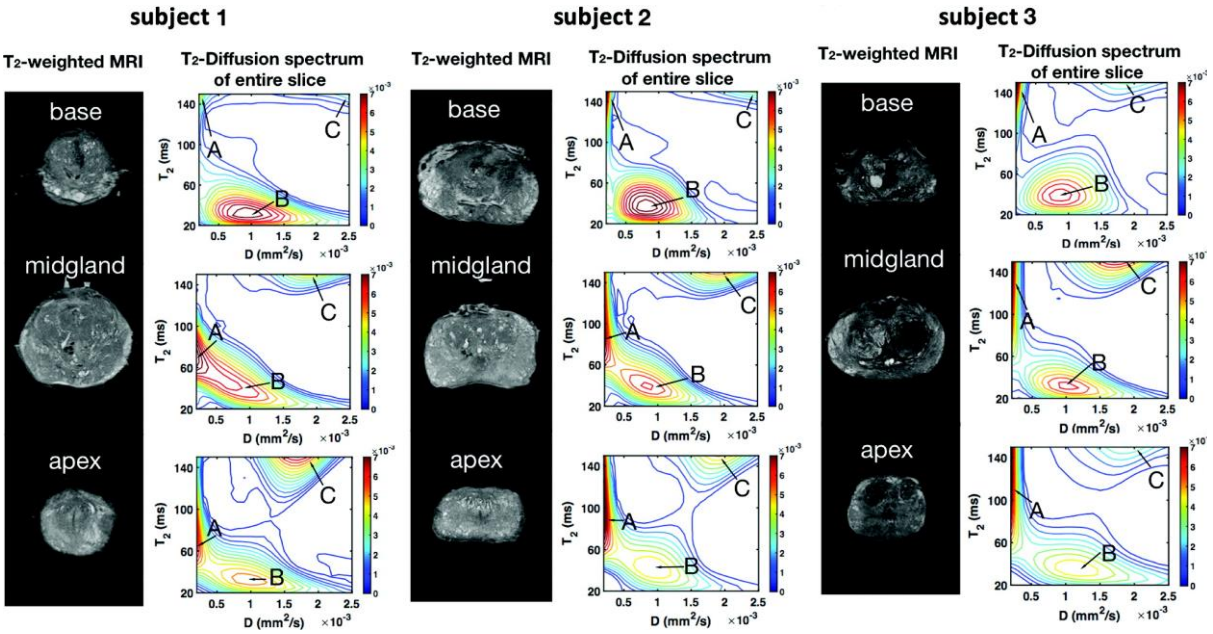

Figure 5.3. Examples of diffusion-relaxation correlation spectrum imaging spatially averaged T2 diffusion (D) signal spectra in three participants. Across the base, midgland, and apex slices in the prostate specimens, the slice-averaged T2-D spectra exhibited a similar distribution of spectral peaks, reflecting the effects of multiple prostate microstructure compartments. At least three distinct signal components (peaks A, B, and C) were identified, and the locations of these peaks are indicated (arrows). The spectra for each slice were individually normalized, such that the integral of signal in each T2-D spectrum equals 1.

5.3.4 Histopathology and DR-CSI Differences Between PCa and Benign Tissues

Representative examples evaluating differences between PCa and benign tissues in the PZ (**Fig. 5.4**) and TZ (**Fig. 5.5)** in terms of ($f_{epithelium}$, f_{stroma}, f_{lumen}) and DR-CSI (f_A, f_B, f_C) are shown.

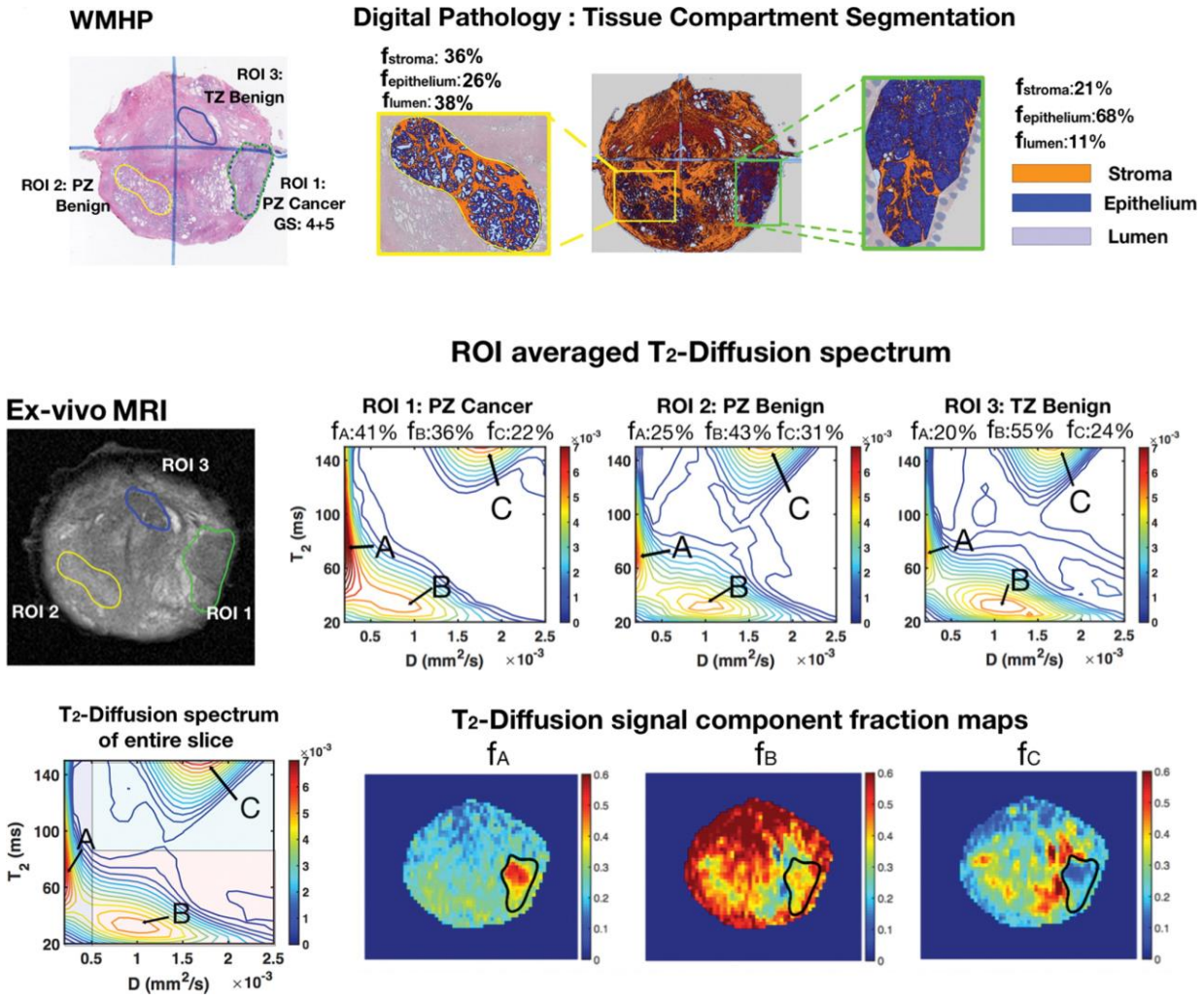

Figure 5.4. Representative example of digital histopathology and diffusion-relaxation correlation spectrum imaging (DR-CSI) analysis of the prostate microstructure in regions of prostate cancer (region of interest [ROI] 1) and benign tissues (ROIs 2 and 3). Digital histopathology software segmented the slide into multiple tissue compartments (stroma, epithelium, and lumen). Peripheral zone (PZ) cancer (ROI 1) showed an increase in epithelium (0.68 vs 0.26) and a decrease of lumen (0.11 vs 0.38) area fractions compared with benign PZ (ROI 2). ROI 3 (benign TZ) is only shown for illustrative purposes and was not included in the statistical analysis. On normalized DR-CSI T2-diffusion spectra, the prostate cancer (PCa) region showed an increase in peak A and a decrease in peak C compared with benign PZ (ROI 2), with higher f_A (0.41 vs 0.25) and lower f_C (0.22 vs 0.31). PZ cancer showed increased f_A and decreased f_C. The PZ cancer ROI is outlined in black.

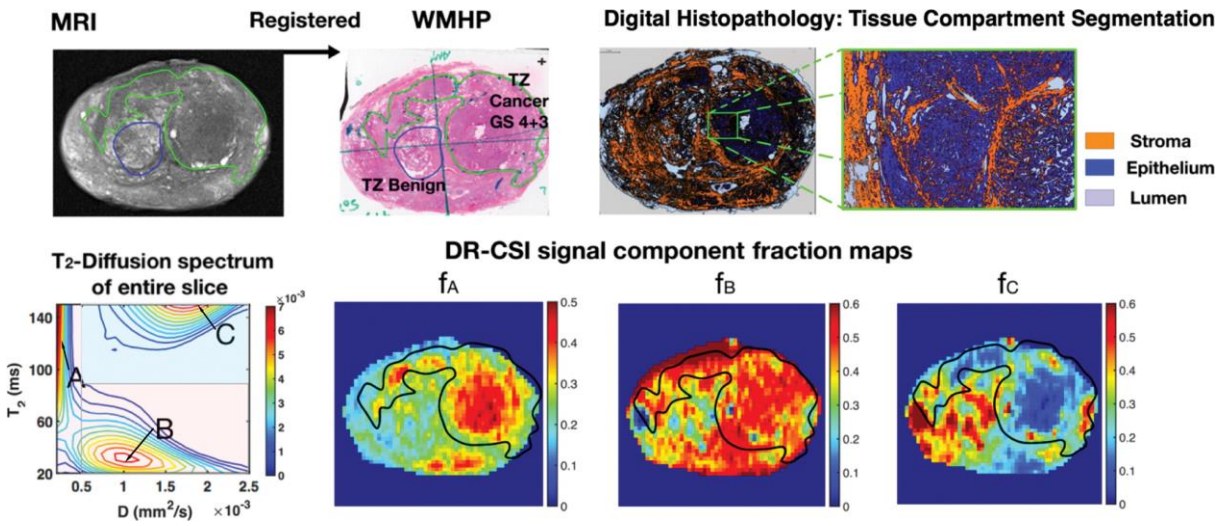

Figure 5.5. Representative example of digital histopathology and diffusion-relaxation correlation spectrum imaging (DR-CSI) analysis of prostate microstructure in transition zone (TZ) prostate cancer. Digital histopathology analysis showed an increase of epithelium and a decrease of lumen in the region of TZ prostate cancer compared with the region of benign TZ. On the DR-CSI signal component fraction maps (f_A, f_B, f_C), the TZ cancer region showed increased f_A and decreased f_C compared with benign TZ tissue. The TZ cancer region of interest is outlined in black

The histopathology reference showed PCa had higher $f_{epithelium}$ (0.44±0.13 vs 0.26±0.16; P<0.001) and lower f_{lumen} (0.14±0.08 vs 0.27±0.18; P=0.004) than benign tissues (TZ and PZ combined) (**Table 5.3**), while f_{stroma} (0.42±0.13 vs 0.47±0.25; P=0.49) did not show differences. For sub-analysis in PZ, PCa had higher $f_{epithelium}$ (0.47±0.14 vs 0.32±0.16; P=0.02) and lower f_{lumen} (0.14±0.09 vs 0.34±0.19; P=0.01) than benign tissues. In TZ, PCa had a higher $f_{epithelium}$ (0.39±0.09 vs 0.21±0.14; P=0.02) than benign tissues.

DR-CSI showed PCa had higher f_A (0.37±0.05 vs 0.27±0.06; P<0.001) and lower f_C (0.18±0.06 vs 0.31±0.13; P=0.01) than benign tissues (TZ and PZ combined) (**Table 5.3**), while f_B (0.44±0.07 vs 0.43±0.12; P=0.51) did not show differences.

For the sub-analysis of the PZ, PCa had higher f_A (0.39±0.10 vs 0.29±0.10; P<0.001) and lower f_C (0.18±0.05 vs 0.35±0.15; P=0.005) than benign tissues. In the TZ, PCa had higher f_A (0.33±0.10 vs 0.25±0.05; P=0.006) than benign tissues.

	Combined peripheral and transitional zone			Peripheral zone			Transitional zone		
	PCa (N=20)	Benign (N=20)		PCa (N=11)	Benign (N=11)		PCa (N=9)	Benign (N=9)	
DR-CSI*	Mean±SD								
f_A	0.37±0.05	0.27±0.06	***P*<0.001**	0.39±0.1	0.29±0.1	***P*<0.001**	0.33±0.1	0.25±0.05	***P*=0.006**
f_B	0.44±0.07	0.43±0.12	P=0.51	0.41±0.1	0.35±0.11	-	0.48±0.08	0.46±0.1	-
f_C	0.18±0.06	0.31±0.13	***P*=0.01**	0.18±0.05	0.35±0.15	***P*=0.005**	0.18±0.07	0.28±0.07	P=0.23
Digital histopathology (reference)									
	Mean±SD								
$f_{epithelium}$	0.44±0.13	0.26±0.16	***P*<0.001**	0.47±0.14	0.32±0.16	***P*=0.02**	0.39±0.09	0.21±0.14	**P=0.02**
f_{stroma}	0.42±0.13	0.47±0.25	P=0.49	0.38±0.13	0.34±0.18	-	0.49±0.11	0.56±0.26	-
f_{lumen}	0.14±0.08	0.27±0.18	***P*=0.004**	0.14±0.09	0.34±0.19	***P*=0.01**	0.12±0.06	0.22±0.16	P=0.36

Table 5.3.
Diffusion-relaxation correlation spectrum imaging (DR-CSI) and digital histopathology analysis of prostate cancer (PCa) and benign tissues. DR-CSI (f_A, f_B, f_C) and histopathology ($f_{epithelium}$, f_{stroma}, f_{lumen}) parameters were evaluated in 40 ROIs (20 PCa & 20 benign; 22 peripheral zone [PZ] & 18 transition zone [TZ]) from 9 prostate specimens, reported as mean ± standard deviation. Some cancers appeared on multiple WMHP slides and had more than one associated ROI. The primary analysis was to evaluate differences between PCa and benign tissues (PZ&TZ combined) in terms of (f_A, f_B, f_C) and ($f_{epithelium}$, f_{stroma}, f_{lumen}) using a two-sided t test. The DR-CSI or histopathology parameters that showed significant differences in the primary analysis were further tested in a sub-analysis PZ and TZ separately. P-values indicating statistically significant differences are indicated in bold.

*Footnote: f_A, f_B, f_C represent the DR-CSI signal component fractions quantified from the region-averaged T_2-D spectrum in evaluated ROIs. $f_{epithelium}$, f_{stroma}, f_{lumen} represent the area fractions of epithelium, stroma and lumen from ROIs. For the primary analysis, the Bonferroni method was used to correct for comparisons involving multiple variables. For the sub-analysis, post-hoc Tukey honest test was used to preserve the family-wise Type 1 error as <0.05 for multiple comparisons.

5.3.5 DR-CSI Correlation with Digital Histopathology

DR-CSI f_A, f_B, and f_C were positively correlated with $f_{epithelium}$, f_{stroma}, and f_{lumen}, respectively (all P<0.001) based on a linear mixed-effects model. The Spearman's correlation coefficients were: ρ=0.74 (95% CI: 0.62, 0.83) for f_A vs. $f_{epithelium}$; ρ=0.80 (95% CI: 0.66, 0.89) for f_B vs. f_{stroma}; ρ=0.68 (95% CI: 0.51, 0.81) for f_C vs. f_{lumen} (**Figure 5.6a**).

DWI ADC was negatively correlated with $f_{epithelium}$ (P<0.001) with ρ =-0.68(-0.78, -0.56), and positively correlated with f_{lumen} (P=0.002) with ρ =0.42 (0.23, 0.59). The correlation between ADC and f_{stroma} was not significant (P=0.77) with ρ =0.02 (-0.38, 0.30) (**Figure 5.6b**).

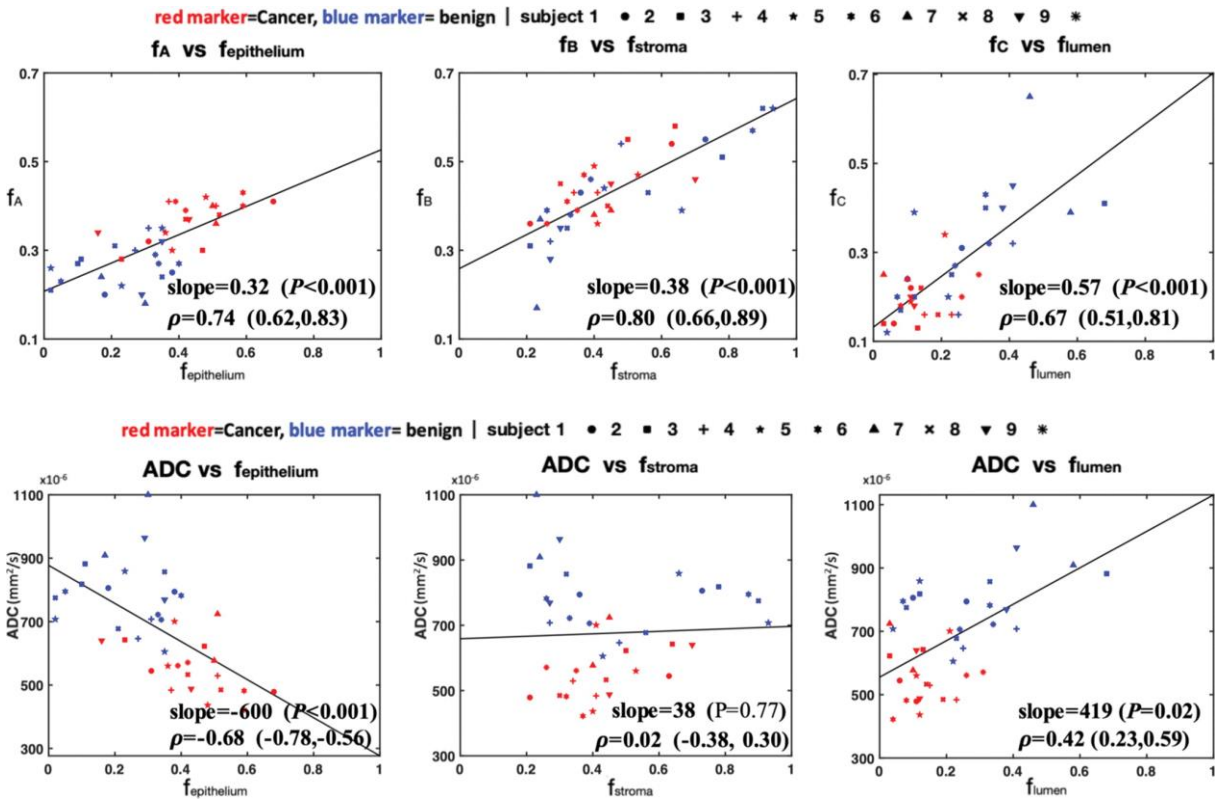

Figure 5.6. **(a)** Correlation between DR-CSI signal component fractions (f_A, f_B, f_C) and tissue compartment fractions ($f_{epithelium}$, f_{stroma}, f_{lumen}) generated using digital histopathology from the 40 regions of interest (ROIs) from 9 prostates. Red markers indicate prostate cancer (PCa) ROIs; blue markers indicate benign tissue ROIs; markers of different shapes denote ROIs from different prostates, ρ is the Spearman's correlation coefficient, with bootstrapped 95% confidence interval provided in parentheses **(b)** Correlation of apparent diffusion coefficient (ADC) and microscopic tissue compartments ($f_{epithelium}$, f_{stroma}, f_{lumen}) for the same ROIs.

5.4 **Discussion**

In this study, we found positive correlations between DR-CSI signal component fractions and WMHP area fractions of epithelium, stroma, and lumen (all $P<0.001$), with Spearman's correlation coefficients of 0.74, 0.80, and 0.67, respectively. DR-CSI showed consistent findings in PCa with respect to histopathology in terms of increased f_A ($f_{epithelium}$) and decreased f_C (f_{lumen}) in the PZ and TZ combined. In the TZ, increased f_A ($f_{epithelium}$) enabled PCa to be distinguished from benign tissues, while in the PZ, reduction in f_C (f_{lumen}) alone was sufficient. This is consistent with tissue heterogeneity in the TZ. For example, in stromal benign prostatic hyperplasia, TZ has a low proportion of lumen, while benign PZ mostly has a high proportion of lumen component [119].

Our results share consistent findings and also differences compared to other microstructural MRI techniques. Consistent with luminal water imaging, reduction in lumen (peak C in DR-CSI) was a characteristic of PCa in PZ. However, luminal water imaging has limitations in resolving epithelium and stroma due to the small T_2 difference [70,21]. DR-CSI separated these two compartments with the additional diffusion encoding. DR-CSI f_A served as a discriminator for PCa in both the PZ and TZ, similar to the VERDICT intracellular volume fraction [20,23]. While VERDICT pre-assumed a three-component signal model with fixed cell radius, no such priors were needed in DR-CSI. Unlike hybrid-multidimensional MRI, DR-CSI did not use pre-determined prostate tissue ADC values from high-field MR microscopy for its model [22,24].

DR-CSI signal components had stronger correlations with microscopic tissue compartments relative to ADC. In the analysis of MRI signals from mm-scale voxels containing multiple tissue compartments, ADC from a mono-exponential model would be a "weighted average" of the diffusivities of all compartments, and not directly reflecting the proportions of individual tissue compartments. As PCa is associated with specific changes in each tissue compartment, this likely

also leads to weaker correlation of ADC with Gleason score relative to multi-component MRI as previously reported [22,21,23,120,121].

Limitations

Our study has limitations. First, prostate DR-CSI was only acquired *ex vivo*, and has not been evaluated *in vivo*. Compared to *ex vivo* imaging, *in vivo* imaging using a body array-coil has lower signal-to-noise ratio, which can cause bias in tissue diffusivities estimates [122]. Second, the higher body temperature will lead to higher tissue compartmental diffusivities *in vivo* [123]. The use of an endorectal coil and adjustment of b-values may be necessary to maintain sufficient signal-to-noise ratio for *in vivo* prostate DR-CSI. Third, pathophysiological changes within the prostate after excision will also cause differences. For example, perfusion effects are present and a higher luminal compartment T_2 and f_C are also expected for *in-vivo* DR-CSI due to reduction in ejaculatory fluid and luminal space after excision [124]. Fourth, due to the limited sample size, we did not evaluate DR-CSI with respect to PCa aggressiveness and various types of benign prostatic hyperplasia. Fifth, the diffusion times for current acquisitions were 28-58 ms and we did not consider non-Gaussian diffusion effects for DR-CSI reconstruction [69]. Finally, although DR-CSI consistently identified three signal components corresponding to epithelium, stroma and lumen, there may be other tissue compartments in the prostate to consider in the future [16].

5.5 **Conclusion**

Correlations between DR-CSI signal components and microscopic tissue compartments and differences of DR-CSI signal components between PCa and benign tissues show that DR-CSI can provide microstructural information for PCa characterization.

Chapter 6 Sequential Backward Selection Analysis for Acceleration of Prostate Microstructure Mapping Using Diffusion-Relaxation Correlation Spectrum Imaging

6.1 Introduction

Multi-parametric MRI has become an essential tool for the clinical diagnosis and management of patients with PCa [2,46]. However, multi-parametric MRI still misses certain PCa and has difficulty distinguishing clinically significant (cs) PCa, often defined as histopathological Gleason score (GS) > 3+3 [17], from indolent PCa [46], and histopathological analysis of prostate tissue remains the reference standard for PCa diagnosis [17]. Recent quantitative histopathological analysis revealed that the relative amounts of epithelium, stroma, and lumen in prostate tissues correlated strongly with the Gleason patterns and could be potential predictors of PCa aggressiveness [70]. Therefore, to improve the ability of MRI to characterize PCa aggressiveness and classify csPCa, microstructural MRI techniques that leverage multi-component signal models are being developed to resolve the relative signal contributions in millimeter-scale MRI voxels that are associated with distinct microscopic tissue compartments (epithelium, stroma and lumen) in prostate tissues based on their T_2 relaxation time or diffusivity (D) differences [21,20,22,19,96] . Improved separation between indolent PCa and csPCa was demonstrated using microstructural MRI parameters compared to the conventional apparent diffusion coefficient (ADC) [23], implying that improved specificity to prostate tissue microstructure can benefit MRI-based characterization of PCa aggressiveness.

Recently, multi-dimensional diffusion-relaxation correlation spectral MRI techniques [26,116,32], such as Diffusion-Relaxation Correlation Spectrum Imaging (DR-CSI), have been

developed [32] and investigated for prostate microstructure mapping [96]. DR-CSI acquires MRI signals encoded at various echo times (TE) and b-values to reconstruct a spectrum of T_2-D components contributing to the overall MRI signal in each voxel, and generate signal component fraction maps by integrating each spectral peak on the voxel-wise T_2-D spectra [32,116]. A unique strength of DR-CSI is that T_2 and diffusion information are considered jointly for 2D spectral separation of signal components, and in theory no prior assumptions on the number of signal components and values of component-specific T_2 or D are needed [26]. Using patient-specific 3D-printed molds and software registration for accurate spatial alignment, the DR-CSI voxel-wise T_2-D spectra and derived signal component fraction values (f_A, f_B, f_C) from *ex vivo* prostate specimens at 3T were shown to be significantly correlated to measurements of epithelium, stroma, and lumen area fractions from digital whole-mount histopathology (WMHP) reference data in spatially matched regions of interest (ROI). There were also significant differences between DR-CSI (f_A, f_B, f_C) in benign prostate tissue and PCa [96]. These results demonstrated that DR-CSI can characterize prostate tissue properties that are consistent with microscopic histopathological features to improve microstructural characterization of PCa.

While DR-CSI provided unique microstructural information in prostate tissue, it substantially increased scan time compared to conventional quantitative MRI sequences (e.g., ADC or T_2 mapping) since it employed two-dimensional (2D) contrast encodings in both the TE and b-value dimensions to be sensitive to both T_2 and D of tissues for 2D spectral separation of signal components. This may lead to challenges for applying DR-CSI when scan time is restricted (e.g., in vivo clinical imaging), and the prolonged scan time could also increase the potential for DR-CSI reconstruction errors due to patient motion [25].

An important strategy to accelerate microstructural MRI is through subsampling the signals in the encoding space (e.g., TE and b-value in DR-CSI), and the effects of the subsampling pattern (i.e., number of encodings and specific choices of the encodings included) on reconstruction accuracy of microstructure parameters need to be evaluated carefully. This can be formulated as a protocol design problem of determining a subsampled encoding scheme that minimizes scan time (i.e., by minimizing the number of encodings, N_{encode}) while maintaining sufficient accuracy of estimated microstructure parameters for characterizing tissue pathology (e.g., distinguishing PCa from benign prostate tissue). The subsampled encoding scheme design problem has primarily been studied for quantitative MRI with one dimension of contrast encoding [125-130], and only recently for multi-dimensional quantitative and microstructural MRI, mostly via simulations and in studies considering the central nervous system (e.g., brain, spinal cord) [131-138]. More recently, the subsampling scheme design problem for prostate microstructural MRI has been explored in a pilot study including 3 healthy subjects using hybrid-multidimensional MRI based on a 3-compartment biophysical model [139]. Investigation of subsampling schemes in a larger cohort of PCa patients using spectrum-based microstructural MRI techniques such as DR-CSI is lacking.

A potential strategy to subsample the encoding space for microstructural MRI is to perform feature selection of the encoding space (such as TE-b space in DR-CSI) while aiming to preserve the quality and accuracy of the reconstructed microstructure parameters or spectrum. Previously, the Sequential Backward Selection (SBS) algorithm has shown promise to select subsampled TE-b encoding schemes that minimized a cost function based on the Cramer-Rao lower-bound (CRLB) for accelerated spinal cord microstructural imaging [135,137]. This promising SBS feature selection technique may also benefit the acceleration of prostate microstructure mapping, but has yet to be evaluated. Therefore. the purpose of this study is to evaluate the SBS feature selection

technique to accelerate prostate DR-CSI by determining subsampled TE and b-value encoding schemes that reduce scan time and accurately quantify tissue microstructure parameters in PCa in *ex vivo* prostate specimens from patients with PCa.

6.2 **Methods**

6.2.1 SBS Analysis for Subsampling DR-CSI

Figure 6.1A showed the SBS based analysis pipeline to evaluate and determine subsampled TE and b-value (TE-b) encoding schemes for DR-CSI that reduce scan time (i.e., reduce number of TE-b encodings, N_{encode}) while ensuring a specified level of accuracy (i.e., error threshold) for estimating prostate tissue microstructure parameters.

To achieve this goal, a reference and quantitative criteria are needed to compare each candidate subsampled TE-b encoding scheme to other candidates in terms of DR-CSI reconstruction accuracy. We established the reference by first acquiring a dataset using a relatively large number (N_{REF}) of TE-b encodings in multiple subjects. The range of TE and b-values variations of the reference dataset were chosen to be the same as a 4x4 TE-b encoding protocol (TE: 60-120 ms, b-values: 0-1500 s/mm^2) validated in a prior *ex vivo* prostate DR-CSI study using digital WMHP as the reference standard [96]. At the same time, the reference dataset contained denser sampling of the b-value space (4 TE x 7 b-values vs. 4 TE x 4 b-values between b=0-1500 s/mm^2) to enable larger degrees of freedom in selecting the TE-b combinations for sub-sampling DR-CSI. The reconstructed voxel-wise DR-CSI T_2-D spectra and signal component fraction values (f_A, f_B, f_C) using the scheme consisting of all acquired TE-b encodings ($S_{N_{REF}}$) were considered the references. Since the microstructural information of prostate tissue characterized by DR-CSI, e.g. multi-component T_2 and D values and signal component fractions, are based on the locations and

the area under the individual spectral peaks on the voxel-wise T_2-D spectra [26], it is natural to compute the voxel-wise errors of the T_2-D spectra for each subsampled TE-b scheme compared to the reference as a quantitative metric to evaluate the accuracy.

To consider all prostate tissue types present in the acquired datasets from multiple subjects, the voxel-wise T_2-D spectral error was summed over all the voxels from prostate tissues and normalized by the total number of voxels (N_{voxels}) to represent the overall reconstruction accuracy, which we termed the mean squared spectral error (MSE):

$$MSE(S) = \frac{1}{N_{voxels}} \sum_{r=1}^{N_{voxels}} \left\| w_S(T_2, D, r) - w_{S_{N_{REF}}}(T_2, D, r) \right\|_2 \quad (6.1)$$

where $w_S(T_2, D, r)$ denotes the T_2-D spectrum at voxel location r (r=1 to N_{voxels}) using a subsampled TE-b encoding scheme S, and $w_{S_{N_{REF}}}(T_2, D, r)$ denotes the reference T_2-D spectrum reconstructed using $S_{N_{REF}}$ with all acquired encodings.

It is worth noting that the non-parametric MSE cost function adopted in this study has differences compared to the parametric CRLB based cost function used in a prior study on DR-CSI subsampling design [135,137]. Both the MSE cost function and CRLB cost function are designed to capture the accuracy of estimated tissue microstructure properties reflected by the T_2-D spectra. While the CRLB cost function mainly considered the reconstruction accuracy of first order T_2-D spectra features such as spectral peak locations and spectral signal component fraction values [135,137], the MSE cost function considered the overall information in the T_2-D spectra, as it directly calculated the mean squared difference between the estimated and reference T_2-D spectra for each voxel. We adopted the MSE criteria as the cost function for SBS in this study mainly due to the fact that it did not require specifying reference parameter values including spectral peak location, spectral peak number, and spectral signal fractions, which were needed in

the parametric CRLB cost function [135,137]. In principle, both criteria (cost functions) can be used to measure the accuracy of DR-CSI reconstruction for SBS analysis, since mathematically MSE is associated with the minimal variance estimator [140], while CRLB is associated with the maximal likelihood estimator [141]. The comparison of these two types of estimators are beyond the scope of this study.

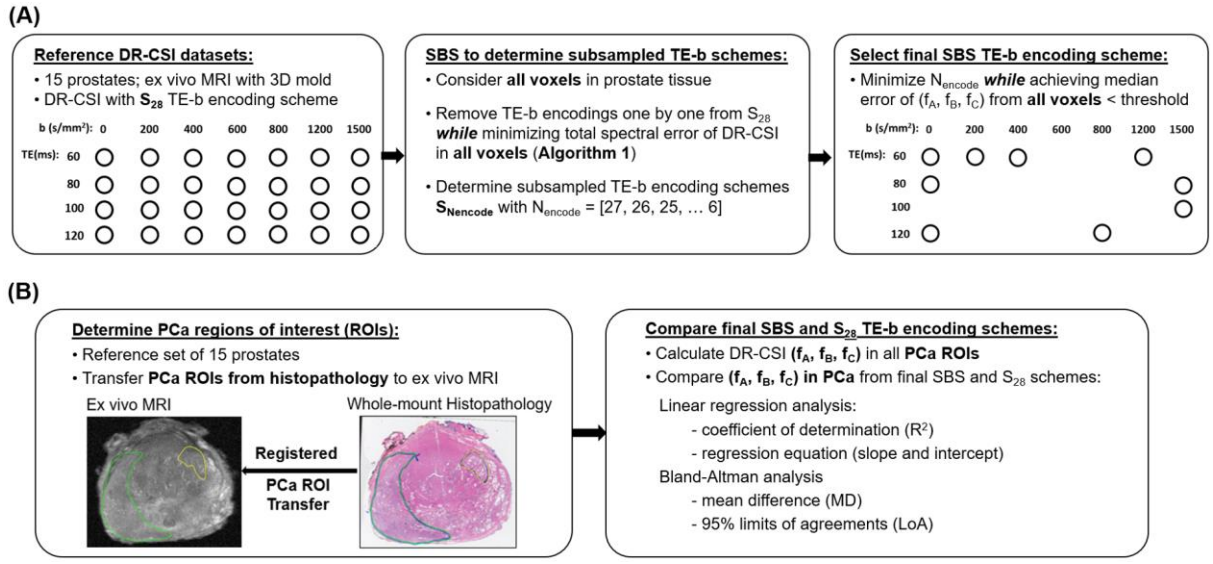

Figure 6.1. Study design and analysis. **(A)** The sequential backward selection (SBS) encoding scheme selection framework analyzed a reference dataset with 28 TE-b encodings for diffusion-relaxation correlation spectrum imaging (DR-CSI) of ex vivo prostate specimens from 15 prostate cancer (PCa) patients to choose a final subsampled encoding scheme (final SBS scheme), which included the most important TE-b encodings while maintaining a specified level of accuracy for voxel-wise estimated prostate microstructure parameters (f_A, f_B, f_C) in all voxels in prostate tissue. **(B)** The performance of the final SBS scheme in terms of its accuracy in characterizing prostate microstructure in PCa were evaluated by comparing the estimated (f_A, f_B, f_C) against results from the reference 28 TE-b encoding scheme in regions of interest (ROIs) from all PCa diagnosed by whole-mount histopathology (WMHP) in the 15 prostates. Use of patient-specific 3D-printed molds and non-rigid registration enabled transfer of pathologist annotation of PCa ROIs from WMHP into the ex vivo MRI space.

The goal of feature selection analysis, such as SBS, is to assesses the relative importance of each individual TE-b encoding in $S_{N_{REF}}$ in terms of its contribution to the final reconstructed voxel-

wise DR-CSI T_2-D spectra. Given the ranking of relative importance of each TE-b encoding in $S_{N_{REF}}$, subsampled schemes that only contained the top ranked TE-b encodings for any given N_{encode} can be determined: $S_{N_{encode}}$. To establish the importance ranking, similar to the prior work [32,135,142], we used the SBS algorithm [143] to determine and remove the TE-b encodings that caused minimal increase in MSE, one at a time from $S_{N_{REF}}$, to achieve a given $N_{encode}<N_{REF}$. The order of removal for each TE-b encoding determined by the SBS analysis was interpreted as the ranking of its relative importance within $S_{N_{REF}}$. The detailed steps of the SBS algorithm are presented in **Algorithm 1**.

Algorithm 1: Sequential backward selection algorithm

1. $e_i = (TE_i, b_i), 1 \le i \le N_{REF}; \quad S_{N_{REF}} = \{e_1, e_2, \ldots e_{N_{REF}}\}; \quad N_{min} \le N_{encode} < N_{REF}$
2. **Initialize:**
   $n \Leftarrow N_{REF}; \quad S_n \Leftarrow S_{N_{REF}}$
3. **while** $n > N_{min}$ **do:**
4. $e^* = argmin\ \boldsymbol{MSE}\ (S_n \backslash \{e_i\})$, "\" denotes removing element from a set
   $e_i \in S_n$
   where $\boldsymbol{MSE(S)} = \frac{1}{N_{voxels}} \sum_{r=1}^{N_{voxels}} \left\| w_S(T_2, D, r) - w_{S_{N_{REF}}}(T_2, D, r) \right\|_2$
5. $S_{n-1} \Leftarrow S_n \backslash \{e^*\}$
6. $N_{encode} \Leftarrow n - 1$
7. $S_{N_{encode}} \Leftarrow S_{n-1}$
8. $n \Leftarrow n - 1$
9. **end while**

6.2.2 Study Design

The overall study design is shown in **Figure 6.1**. Fifteen prostate specimens were obtained from patients with PCa who underwent robotic-assisted laparoscopic prostatectomy. After surgery, each fresh whole prostate specimen was placed in a patient-specific 3D-printed mold and *ex vivo* MRI was performed on a 3 T whole-body scanner (MAGNETOM Prisma, Siemens Healthineers, Erlangen, Germany) [88].

Subsequent to *ex vivo* MRI, the prostate specimen was returned to the surgical pathology lab, sectioned in the 3D-printed mold, and processed to create WMHP slides spatially corresponding to the *ex vivo* MRI planes for histopathological analysis of PCa [88]. A genitourinary pathologist (>10 years of experience), blinded to the MRI, contoured all PCa foci on WMHP slides and assigned GS to them. The characteristics of study participants and diagnosed PCa lesions are listed in **Table 6.1**.

The SBS framework used the reconstructed DR-CSI T_2-D spectra and voxel-wise (f_A, f_B, f_C) from a reference DR-CSI encoding scheme to choose a final subsampled scheme (final SBS scheme) with the most important TE-b encodings that minimized encoding number (N_{encode}) while maintaining a specified level of accuracy for estimation of voxel-wise (f_A, f_B, f_C) (**Figure 6.1A**). The final SBS scheme was further evaluated in terms of its accuracy in characterizing prostate microstructure parameters (f_A, f_B, f_C) in PCa ROIs compared to a reference DR-CSI encoding scheme using linear regression and Bland-Altman analysis (**Figure 6.1B**). The use of 3D-printed patient-specific prostate molds and a non-rigid thin-plate spine registration algorithm [88,144] enabled the transfer of the pathologist's PCa annotations on WMHP into the *ex vivo* MRI space for extracting (f_A, f_B, f_C) measurements in PCa ROIs.

Patient	Age (year)	Weight (kg)	Prostate Volume (cm^3)	PSA (ng/ml)	PCa	Final GS	Tumor extent (cm)	PI-RADS v2 Score
1	63	76.4	26	18.3	Index	3+4	2.9	5
					2nd	3+4	1.5	N/A
2	59	110	52	4.5	Index	3+4	3.1	4
3	56	69	29	8.5	Index	4+4	1	4
					2nd	3+3	1.2	N/A
4	44	88.6	27	3.5	Index	3+3	3.8	4
5	67	74.8	30	3.9	Index	3+4	1.2	4
6	55	80.8	33	3.9	Index	3+4	3.9	4
					2nd	3+3	0.3	N/A
7	65	83.5	29	6.4	Index	4+3	1	5
					2nd	3+4	1.4	N/A
					3rd	3+4	1.4	N/A
8	52	78.5	23	8.8	Index	3+4	2.2	5
					2nd	3+4	1.8	5
9	71	105.7	25	4.9	Index	3+4	2	4
					2nd	3+4	0.8	N/A
10	58	78	45	6.7	Index	4+3	2.2	4
					2nd	3+4	2	3
					3rd	3+4	1.6	N/A
11	60	93.4	41	9.4	Index	3+4	1.6	4
					2nd	3+3	1.2	N/A
12	72	73.3	29	6	Index	4+5	3.5	5
13	61	88.5	33	4.9	Index	4+3	4.2	5
					2nd	3+3	1.6	N/A
					3rd	3+3	1.2	N/A
14	62	98.9	52	5.3	Index	4+5	3.5	5
					2nd	3+3	1.8	N/A
15	58	86.2	35	6.5	Index	4+3	1	5
					2nd	3+4	2.1	N/A
					3rd	3+4	0.9	N/A
Mean±SD	60±7	86±12	34±9	6.8±3.7	GS=3+3: 7; GS>3+3: 23		1.9±1.0	N/A

Table 6.1 :

Participant characteristics. For each man participating in the study, the following are reported: age in years; patient weight in kg; prostate volume in cm^3; pre-surgical prostate specific antigen (PSA) level in ng/ml; final Gleason Score (GS) of each prostate cancer (PCa) lesion based on whole-mount histopathology (WMHP); tumor extent of each PCa in cm based on WMHP; PI-RADS v2 score of PCa detected on in vivo multi-parametric (mp) MRI prior to surgery. Note that PCa lesions missed by mp-MRI but detected on WMHP do not have PI-RADS v2 scores (not applicable, N/A). SD: standard deviation.

6.2.3 Ex Vivo MRI

For *ex vivo* MRI, the prostate specimen was placed within a 3D-printed mold, and the mold was placed in a sealed container filled with perflurocarbon solution (Fomblin, Solvay, New Jersey, USA) to suppress susceptibility artifacts. MRI scans of the prostate in the sealed container were performed using a 15-channel knee coil [88] and the protocol included a high-resolution T_2-weighted MRI sequence and the DR-CSI sequence [96]. DR-CSI was implemented using a modified 2D single-shot spin-echo diffusion-weighted echo-planar imaging sequence with monopolar diffusion waveform to acquire a reference encoding scheme with 28 combinations of TE (60 to 120 ms) and b-values (0-1500 s/mm^2), i.e., N_{REF}=28, with one signal average per TE-b encoding, in 21 min (details in **Table 6.2**).

6.2.4 DR-CSI Reconstruction

DR-CSI used a continuous distribution of exponential decay basis functions characterized by T_2 and D to model the MRI signal in each voxel [32]:

$$M(x,y,TE,b) = \iint w(x,y,T_2,D)\exp\left(-\frac{TE}{T_2}\right)\exp(-bD)dT_2dD = Lw \qquad (6.2)$$

where *M(x,y,TE,b)* represents the voxel-wise measured signals with each TE-b encoding, *w(x,y,T_2,D)* represents the voxel-wise T_2-D spectra to be reconstructed, and *L* represents the Laplace Transform. To reduce the ill-posedness of this inverse problem, non-negativity (i.e.,

$w(x,y,T_2,D)\geq 0$) and spatial total variation (TV_{xy}) constraints were applied to solve for $w(x,y,T_2,D)$ using convex optimization [32].

$$w = \underset{w}{\operatorname{argmin}} \ \|M - Lw\|_F^2 + TV_{xy}(w), \text{subject to } w \geq 0. \tag{6.3}$$

where $\|\cdot\|_F$ represents the Frobenius norm.

Each peak in voxel-wise T_2-D spectra represented an individual signal component. The signal component fractions (f_A, f_B, f_C) corresponding to three peaks A, B, and C on T_2-D spectra of ex vivo prostate DR-CSI for a voxel or spatial region were calculated by integrating each spectral peak on the voxel-wise or region-averaged T_2-D spectra followed by normalization [32,116]. For example, to calculate f_A:

$$f_A(x,y) = \frac{\int_{\text{Area under peak A}} w(x,y,T_2,D)dT_2dD}{\int_{\text{entire } (T_2-\text{D}) \text{ space}} w(x,y,T_2,D)dT_2dD} \tag{6.4}$$

The following definitions for peak A, B and C within the reconstructed T_2-D space (T_2 range: 20-150 ms, D range: 200-2500x10^{-6} mm^2/s) in ex vivo prostate DR-CSI were used to compute f_A, f_B, and f_C based on findings from a previous study [96]: peak A$\in$[$T_2\leq$150 ms, D<500x10^{-6} mm^2/s], peak B$\in$[T_2<80 ms, D$\geq$500x10^{-6} mm^2/s], and peak C$\in$[$T_2\geq$80 ms, D$\geq$500x10^{-6} mm^2/s].

DR-CSI parameter	Value
Echo time (TE) (ms)	60, 80, 100, 120
b value (s/mm^2)	0, 200, 400, 600, 800, 1200, 1500
Repetition time (TR) (ms)	5000
Field of view (mm^2)	160 x 80
Resolution (mm^2)	1.0 x 1.0
Slice thickness (mm)	4.5
Diffusion encoding	Monopolar; 3-scan trace
Diffusion time (ms)	28-58
Parallel imaging factor	2
Partial Fourier factor	6/8
Number of slices	16
Averages	1
Scan time* (min)	21

Table 6.2 :
Sequence and imaging parameters for diffusion-relaxation correlation spectrum imaging (DR-CSI) of *ex vivo* prostate specimens at 3 T. The reference DR-CSI acquisition includes 4x7 (in total 28) combinations of TE and b-values. *Note: The scan time reported here included the vendor implemented calibration pre-scans for eddy-current correction per individual TE-b encoding image acquired, which likely can be substantially reduced (e.g., by half) by simply only acquiring one pre-scan for entire acquisitions. Nonetheless, here we reported the total experiment time.

6.2.5 SBS Analysis of Subsampled TE-b Encoding Schemes

The DR-CSI reconstruction results using all acquired TE-b encodings, N_{REF}=28, were considered to be the reference, and all voxels in prostate tissues from 15 prostates (a total of 91,356 voxels) were used for subsequent computation of MSE and SBS analysis (**Figure 6.1A**). The SBS framework analyzed subsampled schemes (S) as N_{encode} was reduced: [N_{REF}-1, N_{REF}-2 …., N_{min}].

MSE (Equation 1) was used as the cost function to determine the subsampled encoding scheme ($S_{N_{encode}}$) that minimized MSE at each step. This formed a series of selected subsampled schemes $S_{N_{encode}}$ for each evaluated N_{encode}. In this study, N_{encode} was reduced from N_{REF}-1=27 until N_{min}=6, as at least 3+3=6 encodings were needed to perform bi-exponential D and bi-exponential T_2 fitting. The details of the SBS algorithm were presented in **Algorithm 1**.

Determining Final SBS Subsampled TE-b Encoding Scheme

For each $S_{N_{encode}}$ scheme determined by the SBS algorithm, we calculated absolute error of (f_A, f_B, f_C), defined as $\Delta f(r) = |\Delta f_A(r)| + |\Delta f_B(r)| + |\Delta f_C(r)|$, for every prostate tissue voxel r, r=1:N_{voxels}, compared to the $S_{N_{REF}}$ scheme. Histogram analysis of Δf from all prostate tissue voxels in 15 prostates was used to determine the final SBS scheme that minimized N_{encode} (and scan time) while maintaining sufficient accuracy for estimating voxel-wise (f_A, f_B, f_C). It was reported that PCa and benign prostate tissue had mean difference of 0.1 to 0.13 in f_A and f_C [96]. Therefore, a conservative threshold of median Δf<0.1 was used to select the final SBS scheme.

Evaluation of Final SBS Scheme for Estimating (f_A, f_B, f_C) in PCa

Linear correlation and Bland–Altman analysis were performed to evaluate the agreement between estimated mean (f_A, f_B, f_C) from the final SBS and reference 28 TE-b encoding schemes in 30 PCa ROIs (one ROI per PCa) (**Table 6.1**). For PCa that appeared on multiple slices, the ROI was specified on the slice with the largest cross-section area of the PCa, consistent with the histopathological analysis of tumor extent for each PCa [46]. Linear correlation analysis between two compared techniques yielded a slope and intercept. The coefficient of determination (R^2) was used to evaluate the strength of the linear correlation. Bland–Altman analysis was performed to

calculate the mean difference (MD) between two schemes, and the 95% limits of agreement (LoA) were reported as the deviation from the mean difference by 1.96 times standard deviation (SD). For all statistical comparisons, $P<0.05$ was considered significant.

6.3 **Results**

6.3.1 SBS Analysis of Subsampled TE-b Encoding Schemes

Figure 6.2A shows the results of each step of SBS and the corresponding SBS subsampled TE-b encoding schemes with minimum MSE as N_{encode} was reduced from 27 to 6 (scan duration reduced from 21 min to 4.5 min). The relative importance of each individual TE-b encoding according to its removal order in the SBS analysis is shown in **Figure 6.2B**, color-coded from white to black and numbered (least to most important) within the acquired reference 28 TE-b encoding scheme. The evolution of MSE for SBS subsampled schemes versus N_{encode} is presented in **Figure 6.2C**.

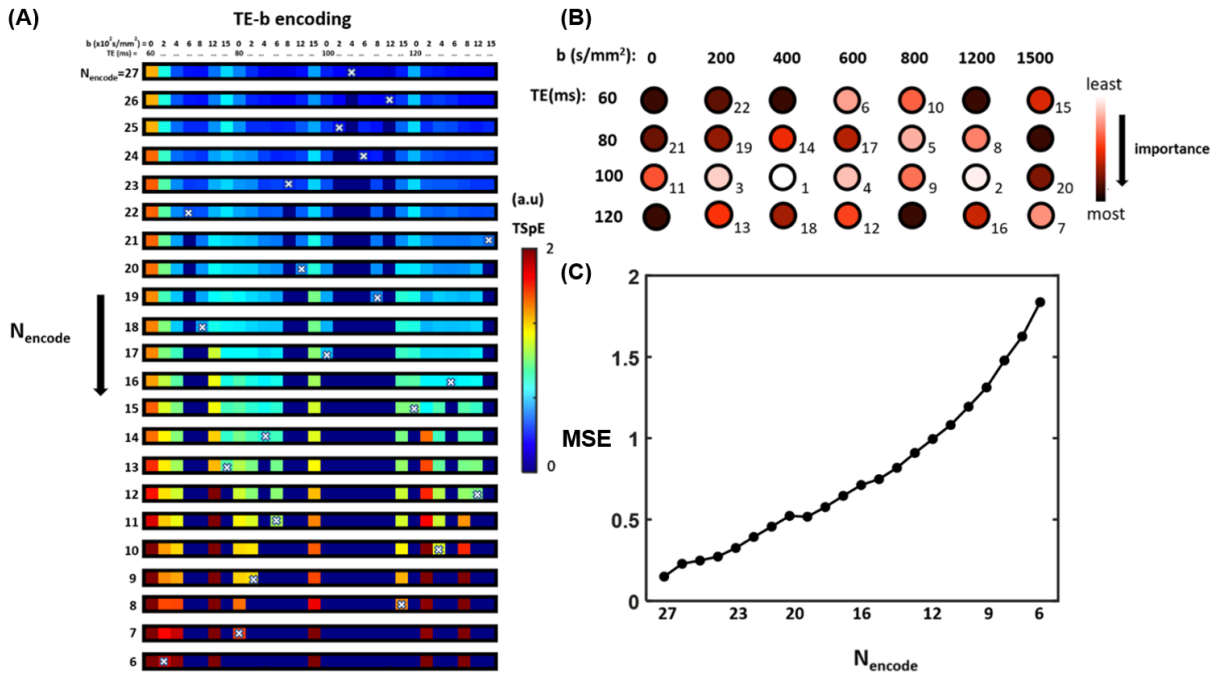

Figure 6.2. **(A)** Results of the sequential backward selection (SBS) algorithm for determination of the subsampled TE-b encoding schemes for DR-CSI, as the total number of encodings (N_{encode}) was reduced from 28 to 6. The color scale indicates the normalized mean square spectral error (MSE) (for a total of 91,356 voxels from all cases) associated with removing a certain TE-b encoding. White crosses denote the specific encoding removed at each step of SBS as its removal resulted in minimal MSE compared to other encodings. **(B)** The relative importance of each individual TE-b encoding according to its removal order in the SBS analysis, color-coded from white to black and numbered (least to most important) within the acquired reference 28 TE-b encoding scheme. **(C)** MSE for each SBS TE-b encoding scheme versus N_{encode} (from 27 to 6).WMHP into the ex vivo MRI space.

Two representative examples comparing the accuracy of reconstructed DR-CSI T_2-D spectra and voxel-wise (f_A, f_B, f_C) maps using SBS subsampled TE-b encoding schemes with N_{encode}=16, 12, 9, and 6, with respect to the reference encoding scheme S_{28} are shown in **Figures 6.3 and 6.4**.

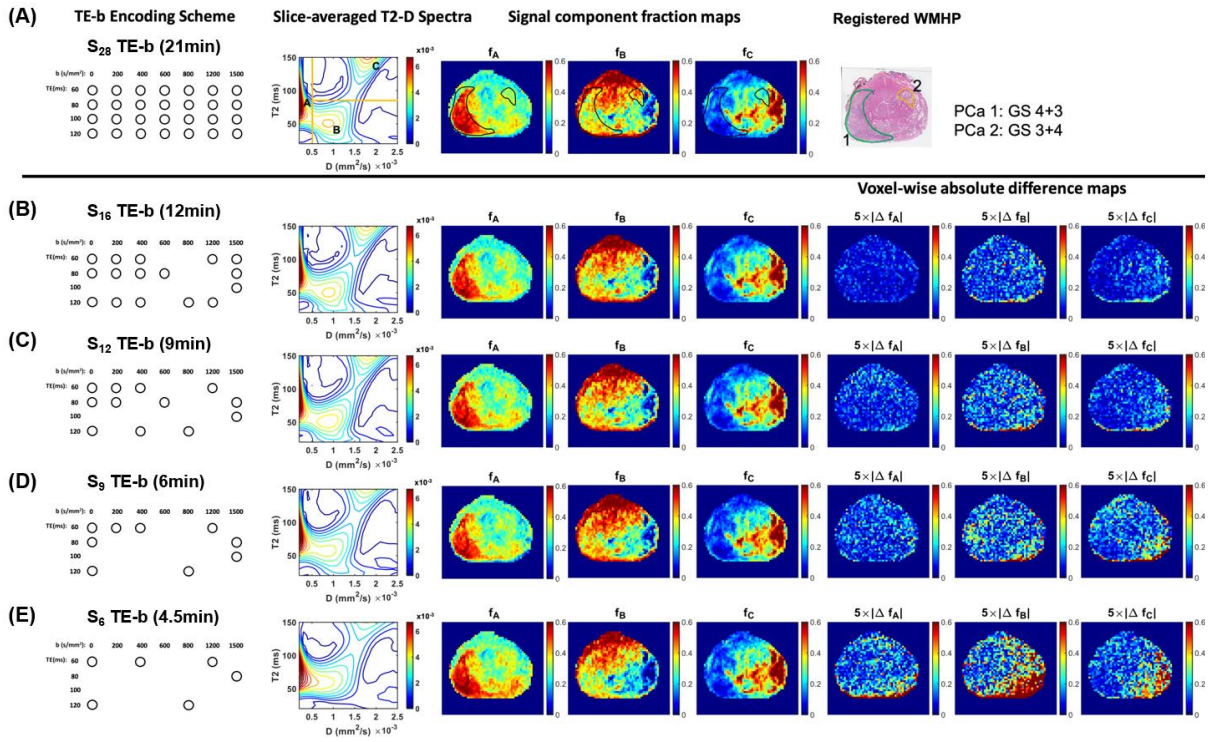

Figure 6.3. A representative example comparing the slice-averaged DR-CSI T_2-D spectra and derived voxel-wise signal component fraction maps (f_A, f_B, f_C) reconstructed from reference and SBS subsampled TE-b encoding schemes for a slice containing two prostate cancer (PCa) lesions from patient #13 in **Table 6.1**. **(A)** Reference S_{28}, **(B)** S_{16}, **(C)** S_{12}, **(D)** S_9, and **(E)** S_6 TE-b encoding schemes. Absolute difference maps of (f_A, f_B, f_C) from the SBS schemes compared to the reference scheme were computed to evaluate the voxel-wise quantification error, and displayed with 5-fold amplification.

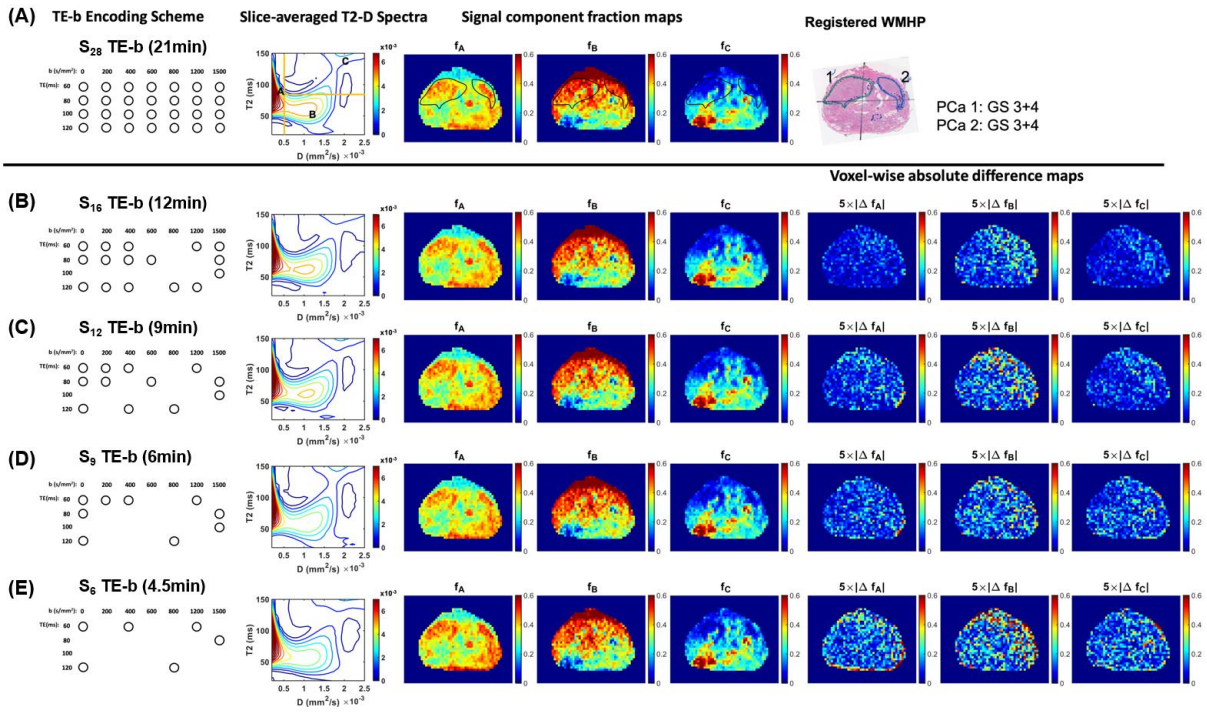

Figure 6.4. A representative example comparing the slice-averaged DR-CSI T_2-D spectra and derived voxel-wise signal component fraction maps (f_A, f_B, f_C) reconstructed from reference and SBS subsampled TE-b encoding schemes for a slice containing two prostate cancer (PCa) lesions from patient #8 in **Table 6.1**. **(A)** Reference S_{28}, **(B)** S_{16}, **(C)** S_{12}, **(D)** S_9, and **(E)** S_6 TE-b encoding schemes. Absolute difference maps of (f_A, f_B, f_C) from the SBS schemes compared to the reference scheme were computed to evaluate the voxel-wise quantification error, and displayed with 5-fold amplification.

6.3.2 Final SBS Subsampled TE-b Encoding Scheme

Results of histogram analysis of Δf to determine the final SBS subsampled TE-b encoding scheme are shown in **Figure 6.5**. S_9 was determined as the final SBS scheme, with reduced scan time of 6 min and median Δf=0.09, which was less than the target threshold of median Δf<0.1.

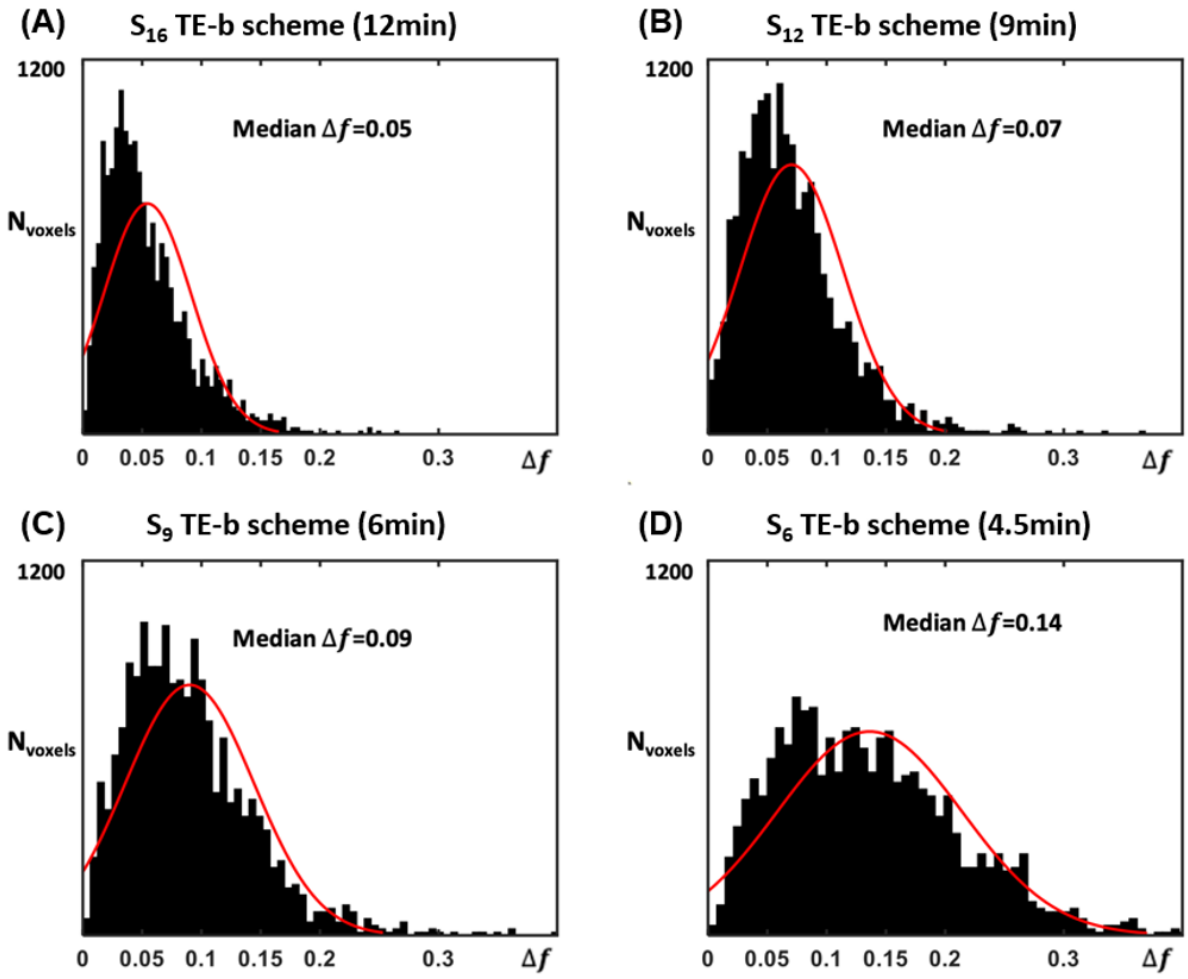

Figure 6.5. Distribution of the voxel-wise absolute error $\Delta f = |\Delta f_A| + |\Delta f_B| + |\Delta f_C|$ of DR-CSI signal component fractions (f_A, f_B, f_C) from all evaluated voxels in prostate tissue. Results from **(A)** S_{16}, **(B)** S_{12}, **(C)** S_9, and **(D)** S_6 TE-b encoding schemes are shown.

6.3.3 Evaluation of Final SBS Scheme for Estimating (f_A, f_B, f_C) in PCa

We evaluated the performance of the final SBS scheme in 30 PCa lesions (23 with GS>3+3 and 7 with GS=3+3) (characteristics are summarized in **Table 6.1**). The f_A, f_B, and f_C values from the S_9 scheme exhibited significant linear correlation with results from the reference S_{28} encoding scheme (R^2=0.96~0.98), with slopes of 0.99, 1.02, and 1.03, respectively (**Figures 6.6A, C, E**). Bland–Altman analysis results between the S_9 and reference S_{28} encoding schemes showed MD of -0.005,

0.0078, and -0.0025, with 95% LoA of [-0.034 0.024], [-0.046 0.061], and [-0.038 0.033], in estimated f_A, f_B, and $f_{C,}$ respectively (**Figures 6.6B, D, F**).

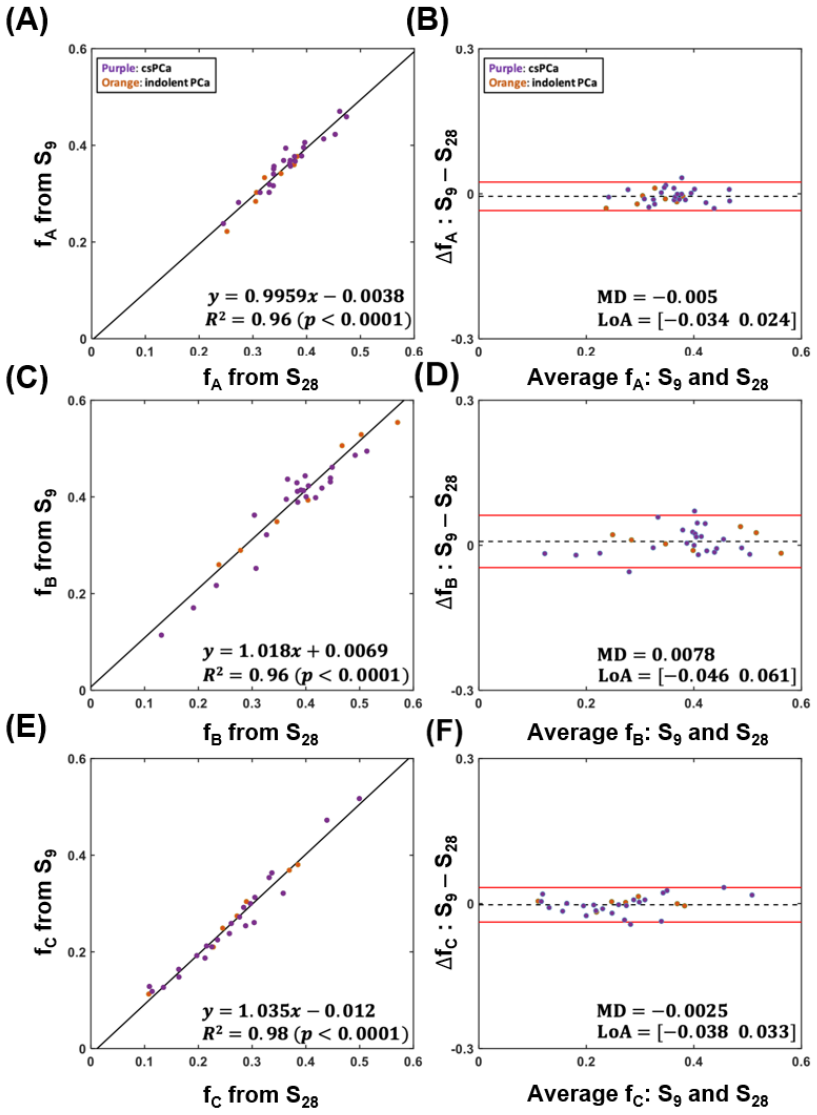

Figure 6.6. Linear regression and Bland-Altman analysis to compare the DR-CSI (f_A, f_B, f_C) from S_9 and reference S_{28} TE-b encoding schemes in 30 prostate cancer (PCa) regions of interest (ROIs). **(A)** Linear regression analysis of f_A, where the solid line represents the fitted linear model, circles denote the measurements from PCa ROIs, purple indicates clinically significant PCa (csPCa) defined as Gleason Score (GS)>3+3, and orange indicates indolent PCa with GS=3+3. **(B)** Bland-Altman analysis of f_A, where MD denotes mean difference (dashed horizontal line) and LoA denotes 95% limits of agreement (red solid lines). **(C, D)** Linear regression and Bland-Altman analysis of f_B. **(E, F)** Linear regression and Bland-Altman analysis of f_C.

6.4 Discussion

In this study, we evaluated SBS feature selection analysis for subsampled encoding scheme design to accelerate DR-CSI for prostate microstructure mapping. Based on a reference dataset acquired with 28 TE-b encodings from 15 prostate specimens, the subsampled encoding scheme with minimal MSE for a range of reduced encoding numbers from 27 to 6 were determined at each step of the SBS analysis. Using a threshold of 0.1 for the median Δf from all prostate tissue voxels, S_9 (6 min) was selected as the final subsampled scheme, achieving 70% scan time reduction compared to the reference S_{28} scheme (21 min). Linear regression and Bland-Altman analysis showed that S_9 achieved close agreement in prostate microstructure parameters (f_A, f_B, and f_C) in PCa ROIs from 15 prostate specimens compared to the reference S_{28} scheme. These results provide evidence that prostate microstructure mapping using DR-CSI can be substantially accelerated using SBS subsampled schemes while maintaining reconstruction accuracy. The subsampling schemes determined by the SBS framework can be considered for future prospective acceleration of prostate DR-CSI scans.

Subsampling of the encoding space is an important strategy for accelerating microstructural MRI. Here we approached the subsampling scheme design problem using the perspective of feature selection. We considered each TE-b encoding in the reference scheme as a feature that contributed to a different degree to the final reconstructed DR-CSI T_2-D spectra. SBS analysis with MSE as the cost function determined features (TE-b encodings) whose removal caused the least degradation in reconstruction accuracy, step by step. The remaining TE-b encodings then formed the selected SBS subsampled scheme, which included the most important features (TE-b encodings) to inform the reconstruction for a given reduced encoding number N_{encode}. Based on the SBS analysis, we found that MSE for SBS subsampled schemes increased smoothly as N_{encode}

was reduced from 28 until 6. The final S_9 scheme (70% acceleration) achieved close agreement with the reference S_{28} scheme in estimating (f_A, f_B, f_C) in PCa ROIs. These results showed that the SBS method can determine subsampled encoding schemes with balanced trade-offs between estimation accuracy and scan time acceleration, implying the feature selection analysis perspective adopted in this study translated well to the subsampled scheme design problem for prostate DR-CSI. While the acceleration factor of 70% and accuracy achieved by the SBS method is promising, different optimization methods previously developed for other feature selection applications, such as particle swarm optimization and forest optimization algorithms could also be investigated in the future that may achieve different performance for accelerating DR-CSI [145].

The final S_9 scheme included 9 TE-b encodings and can be interpreted as the minimal required number of samples in TE-b space to reliably resolve signals from prostate tissue compartments using DR-CSI. This minimal data sampling requirement in principle is closely related to the spectral complexity of the T_2-D spectra, which in turn reflected the complexity of underlying prostate tissue microstructure [26,27]. For example, in *ex vivo* prostate DR-CSI [96], 3 distinct spectral peaks consistently appeared on T_2-D spectra and corresponded to 3 major microscopic tissue compartments in prostate tissue: epithelium, stroma and lumen [70,96]. Therefore, N_{encode}=9 can be interpreted as the minimal encoding needed to fully resolve these 3 spectral peaks. Interestingly, the 9 TE-b encodings that were selected consisted of 4 primarily diffusion-weighted encodings along the b-value axis with minimal TE of 60 ms, 3 primarily T_2-weighted encodings along the TE axis with b-value=0, and 3 encodings with mixed degrees of diffusion and T_2 weighting with TE-b of (80 ms, 1500 s/mm^2), (100 ms, 1500 s/mm^2), and (120 ms, 800 s/mm^2). From the theoretical point of view for a 2D spectral separation problem, the primarily diffusion or T_2-weighted encodings provided information about the projected one-dimensional distribution of

D and T_2 values of tissue compartments, respectively. There is some degree of overlap between tissue compartments when only considering D or T_2, e.g., both epithelium and stroma have a substantially shorter T_2 than lumen and are hard to distinguish using T_2 information alone [21]. The inclusion of TE-b encodings with mixed diffusion and T_2-weighting provided supplemental information to resolve the overlap and achieved successful separation of 3 distinct signals corresponding to tissue compartments, based on joint 2D spectral analysis of T_2-D components. Another important factor determining the minimal data sampling requirement is the reconstruction method used for quantifying voxel-wise DR-CSI T_2-D spectra. In this study, non-negativity constraints and spatial total variation constraints were used to reduce the ill-posedness of the inverse problem for DR-CSI reconstruction and already provided "built-in" reduction in the required number of TE-b encodings compared to reconstruction without the imposed spectral-spatial constrains [25,32].

Recently, an artificial neural network (ANN) based method has been explored for subsampled scheme design for accelerated hybrid-multidimensional MRI for prostate microstructure mapping [139]. Compared to the ANN study, our study acquired a reference dataset that included more TE-b encodings (28 vs. 16) in more prostates (prostates from 15 PCa patients vs. 3 healthy subjects), thus providing more data samples for the non-parametric retrospective subsampling scheme evaluation, the results of which in principle would largely depend on the quality and representativeness of the reference dataset. In addition, the SBS algorithm also provided a ranking of the importance of each TE-b according to the order of its removal to form SBS subsampled encoding schemes. This ranking information can guide the design of acquisition priorities and ordering of TE-b encodings when the available scan time varies. Also, the SBS algorithm does not contain a large number of hyper-parameters that need to be adjusted, as required in certain ANN

based methods [146]. Lastly, our study focused on subsampling scheme design for spectrum-based characterization of prostate microstructure using DR-CSI, while the previous ANN study used a biophysical 3-compartment signal model [22].

Limitations

Our study has limitations. First, prostate DR-CSI was only acquired in *ex vivo* prostate specimens, and the framework has not been evaluated *in vivo*. However, the non-parametric nature of the SBS framework using the MSE cost function provides flexibility to adapt to *in vivo* applications once a reference dataset is acquired. Second, although our acquired dataset of 15 prostates with 28 TE-b encodings already comprised one of the largest datasets for non-parametric analysis of subsampled encoding schemes in microstructural MRI, a larger sample size with even more TE-b encodings may further improve the generalizability of the determined SBS subsampled encoding schemes. Third, the prostate specimens were obtained from PCa patients who underwent radical prostatectomy and may have more aggressive PCa compared to the broader population of patients with PCa. Nonetheless, all prostate tissue voxels, including benign tissues and a total of 30 PCa spanning a range of disease aggressiveness from indolent PCa (GS: 3+3) to csPCa (GS $\geq$3+4), were included in the dataset and analyzed by the SBS framework. Fourth, the diffusion times for current DR-CSI acquisitions were 28-58 ms and we did not consider non-Gaussian diffusion for DR-CSI [69]. However, once diffusion time is incorporated into the DR-CSI model, it can be treated as another encoding dimension to consider for the SBS subsampled scheme analysis.

6.5 **Conclusions**

Using SBS to subsample the TE and b-value encoding space, we achieved 70% reduction in scan time by reducing TE-b encodings from 28 to 9 for *ex vivo* prostate DR-CSI while maintaining accurate prostate microstructure parameter mapping in PCa, compared to a reference encoding scheme.

Chapter 7 **Summary and Discussion**

7.1 **Summary**

This thesis developed and evaluated quantitative prostate diffusion MRI and multi-dimensional diffusion-relaxation correlation microstructural MRI techniques for characterization of prostate cancer. Here we summarize the key findings of two main themes: 1. Improving image quality of prostate diffusion MRI, including reducing geometric distortion, enhancing the signal-to-noise ratio (SNR), and improving spatial resolution; 2. Improving the ability of MRI to infer microscopic features of prostate tissue for characterization of prostate cancer microstructure.

7.2 **Theme 1: Improving Image Quality of Prostate Diffusion MRI**

In **chapter 3**, we evaluated the eddy current-nulled convex optimized diffusion encoding (ENCODE) framework for designing diffusion encoding waveforms for prostate DWI acquisition protocols that minimize TE to maintain SNR while reducing eddy current-induced geometric distortion compared to conventional MONO and BIPOLAR diffusion encoding techniques. We found that ENCODE reduced eddy current-induced geometric distortion in the prostate compared to MONO, while achieving higher SNR in prostate PZ and TZ than BIPOLAR by minimizing TE. The largest advantages in reducing TE and maintaining SNR are for prostate DWI protocols with longer EPI duration, i.e., associated with higher spatial resolution. We further combined reduced FOV (rFOV) acquisition using outer-volume suppression RF pulses with ENCODE diffusion encoding waveforms to address susceptibility-induced and eddy current-induced geometric distortion, respectively. In patients with suspicion of PCa, quantitative geometric distortion analysis using Dice similarity coefficient of prostate contours with respect to T2W TSE MRI prostate reference and qualitative geometric fidelity analysis from two expert radiologists found

that the rFOV-ENCODE technique achieved better geometric fidelity of the prostate compared to the standard full-FOV BIPOLAR DWI technique.

In **chapter 4**, we developed and evaluated a combined TE-minimized ENCODE diffusion encoding acquisition with a random matrix theory (RMT)-based denoising reconstruction technique to improve the SNR and robustness of high-resolution (in-plane: 1.0x1.0 mm^2) prostate DWI and apparent diffusion coefficient (ADC) mapping. To validate that the RMT denoising pipeline mainly removed thermal noise and minimized removal of tissue signals, we analyzed the difference between denoised and original DWI signals and found that the denoising residuals had close agreement with a zero-mean Gaussian distribution assumed by RMT. In patients, we found ENCODE-RMT high-resolution DWI achieved a 2-fold SNR enhancement compared to ENCODE high-resolution DWI in prostate PZ and TZ. In addition, the accuracy and precision of ADC mapping using ENCODE-RMT high-resolution (in-plane: 1.0x1.0 mm^2) DWI matched the benchmark performance of a standard-resolution (in-plane: 1.6x2.2 mm^2) BIPOLAR DWI protocol, while providing a 3.5-fold improvement in spatial resolution.

7.3 Theme 2: Improving the Ability of Prostate MRI to Infer Microscopic Features of Prostate Cancer

In **chapter 5**, we investigated and validated the diffusion-relaxation correlation spectrum imaging (DR-CSI) technique at 3 T for characterizing microscopic tissue compartments (epithelium, stroma and lumen) in prostate tissue and PCa. In *ex vivo* prostate specimens, we found DR-CSI consistently resolved three sub-voxel spectral signal components (spectral peaks A, B and C) in prostates. In addition, we found PCa had significantly higher signal component fraction f_A and lower signal component fraction f_C compared to benign tissue regions. At the same time, whole-

mount digital histopathology analysis showed PCa had higher epithelial area fraction and lower lumen area fraction than benign tissue regions. Using a system combining 3D-printed patient-specific prostate molds and *ex vivo* MRI, we further assessed the relationship between DR-CSI parameters and histopathological measurements of prostate tissue microstructure. We found that DR-CSI spectral signal component fractions f_A, f_B and f_C had significant positive correlations with area fractions of epithelium, stroma and lumen quantified using digital histopathology in matched spatial regions including PCa and benign tissues.

In **chapter 6**, we explored and evaluated sequential backward selection (SBS) analysis for the acceleration of DR-CSI through subsampling of the diffusion-relaxation contrast encoding space while maintaining the accuracy of prostate microstructure mapping in PCa. The reference *ex vivo* prostate DR-CSI datasets including 28 combinations of TE and b-value encodings were subsampled by SBS step-by-step to reduce the encoding number and scan time while minimizing the loss in reconstruction accuracy assessed by overall mean squared error of T_2-diffusivity spectra. We found the *ex vivo* DR-CSI protocol can be accelerated by around 70% using SBS algorithms to reduce the number of TE-b encodings from 28 to 9, while achieving close agreement in the estimated spectral signal component fractions f_A, f_B and f_C for characterizing prostate microstructure in PCa.

7.4 Potential for Improving MRI-based PCa Diagnosis

7.4.1 Improving MRI-based PCa Detection

The rFOV-ENCODE DWI and high-resolution ENCODE-RMT DWI techniques developed in **Theme 1** have potential to improve the performance of MRI-based PCa detection through two mechanisms.

First, diffusion MRI is a key component of prostate mp-MRI and was shown to be the most sensitive modality for PCa detection [3]. However, geometric distortion artifacts from susceptibility or eddy current-induced effects are not uncommon due to the presence of rectal gas or MRI gradient hardware imperfections [79,7]. These artifacts can overlap with the signals from PCa and obscure its detection on DWI, e.g., due to severe signal pile up [7]. The rFOV-ENCODE DWI technique may improve the detection of PCa in these challenging imaging situations by limiting the degree of image distortion in the presence of strong magnetic field inhomogeneities and gradient eddy currents. Although alternative approaches such as bowel preparation using micro-enema [57] were also shown to be effective in reducing the frequency and severity of diffusion MRI distortion artifacts [57], the rFOV-ENCODE method is non-invasive as it reduces geometric distortion through a modified DWI sequence design and may further reduce distortion in subjects who had an imperfect bowel preparation.

Second, the detectability of PCa also depends on the size of the tumor and the imaging resolution of the MRI sequence [10]. For diagnosis and detection of PZ tumors, DWI is the dominant sequence according to PI-RADS v2 guidelines [39]. However, current prostate DWI sequences have in-plane spatial resolution limited to 1.6x1.6 to 2.2x2.2 mm^2 [8]. Therefore, the visualization of smaller PCa tumors below the voxel size is very challenging. Studies evaluating the performance of mp-MRI for detection of PCa using WMHP as reference have found that up to 45% of men had missed PCa [40], and more than 50% of the missed tumors had smaller size with tumor diameter of <7 mm or were sparse tumors that intermixed substantially with adjacent normal tissues [91,13]. The high-resolution (in-plane: 1.0x1.0 mm^2) ENCODE-RMT DWI technique has ~3.5 times higher spatial resolution than standard clinical DWI protocol while maintaining similar ADC accuracy and precision. Theoretically, PCa tumors with sizes smaller

than the standard DWI voxel size could be more conspicuous on the high-resolution ENCODE-RMT DWI and ADC maps, leading to potential improvements in overall PCa detection performance. Another potential application of high-resolution prostate DWI is to improve the definition of PCa margins on DWI, as higher spatial resolution in principle will reduce partial volume averaging effects between tumor cells and adjacent normal tissue at the PCa boundary [9,10]. Since the current standard approach using T2W MRI for estimating PCa margins often resulted in substantially underestimated PCa volume compared to WMHP [147], a high-resolution DWI technique could be valuable for improving MRI-based treatment planning and guidance, e.g., by providing more accurate treatment margin prediction for focal therapy of PCa [148]. Future studies need to explore the potential benefits of translating rFOV-ENCODE DWI and high-resolution ENCODE-RMT DWI for improving PCa detection in a large cohort of PCa patients.

7.4.2 Improving MRI-based PCa Risk Stratification

A key goal of PCa management is to determine the aggressiveness or grade of PCa, so undertreatment of clinically significant PCa and overtreatment of indolent PCa can be avoided [35]. The PI-RADS system is the current standard prostate MRI interpretation system for diagnosis and risk stratification of PCa [39]. Recent studies have reported low yield for detecting clinically significant PCa based on PI-RADS score category 3 lesions on MRI [149]. At the same time, there are ongoing discussion and emerging guidelines suggesting the use of PI-RADS score 3 as a cut-off for recommending patients to forgo biopsies [150], which may minimize the amount of unnecessary invasive biopsies in men.

However, due to the qualitative and subjective nature of the PI-RADS system for categorizing lesion findings on prostate MRI [39], the PI-RADS scores were found to have considerable variability and lack of reproducibility among radiologists, especially regarding the definitions of

PI-RADS 3 lesions [151]. The non-quantitative nature of PI-RADS categorization limits the robustness of using PI-RADS scores for risk stratification of PCa into indolent or clinically significant disease [152].

For the reference histopathological diagnosis of PCa, prostate tissue composition and microstructure features such as the presence and extent of epithelium, stroma and lumen were key determinants for characterization of PCa aggressiveness [153]. Recent digital histopathology research also showed that quantitative tissue microstructure measurements, such as area fractions of tissue compartments, can predict Gleason Scores and have potential to provide more objective and quantitative characterization of PCa aggressiveness [70].

In the *ex vivo* investigations in **Theme 2**, DR-CSI spectral signal components were found to be correlated to histopathological measurements of prostate tissue composition and microstructure (or microscopic tissue compartments) such as epithelium, stroma and lumen. These results showed that DR-CSI analysis of prostate MRI signals can potentially predict microscopic tissue features of PCa that were traditionally inaccessible using conventional MRI sequences and parameters such as T_2 or ADC [15]. Therefore, DR-CSI based prediction of prostate tissue composition and microstructure features have potential to serve as a quantitative and non-invasive means to predict aggressiveness of PCa lesions by providing information representative of histopathology. Unlike the qualitative and subjective nature of PI-RADS scores, the tissue composition and microstructure parameters convey biophysical information and reflect fractions of microscopic tissue compartments within PCa [154]. Thus, prostate microstructure parameters predicted by DR-CSI (e.g., epithelial, stromal and luminal fractions) could offer a more robust means for quantitative risk stratification of PCa for supporting biopsy and treatment decisions, as compared to the current prostate MRI methods and the PI-RADS system.

Clearly, more development and validation are warranted to translate the proof-of-principle findings of *ex vivo* prostate DR-CSI for characterizing prostate cancer microstructure into *in vivo* clinical applications. These include developing faster acquisition strategies through novel sequence designs while maintaining *in vivo* prostate DR-CSI SNR, and comparison of *in vivo* DR-CSI results with reference histopathology. The further developments of prostate microstructural MRI techniques, such as DR-CSI, may lead to next generation prostate MRI techniques that produce non-invasive and quantitative estimates of prostate microstructure features for improving PCa risk stratification and predicting PCa aggressiveness.

7.5 Future Directions

7.5.1 More Comprehensive Evaluation of rFOV-ENCODE Prostate DWI

In **chapter 3**, we evaluated the geometric fidelity of rFOV-ENCODE prostate DWI in 36 patients with clinical suspicion of PCa. However, the sample size of that study is still relatively small, and the geometric distortion of prostate contours were mainly evaluated in the mid-gland level, which may not reflect the full extent of geometric distortion across different prostate planes. More patients should be studied and a more comprehensive geometric distortion evaluation of rFOV-ENCODE against standard prostate DWI along the slice direction from apex to basal planes should be carried out. Another aspect that warrants further evaluation is the quantitative measurement of ADC in PCa using ENCODE compared to standard DWI sequences such as MONO or BIPOLAR. Unlike conventional MONO waveforms having a well-defined diffusion time dictated by the separation of two identical gradient trapezoids [5], the ENCODE waveforms contained several gradient trapezoid lobes with unequal durations and shape as the result of convex optimization and may not have a well-defined single diffusion time. Since theoretically the diffusion length scales

and specific water compartment sizes the DWI experiment measures depend on the diffusion time of the DWI sequence [155,69], ENCODE may probe a range of different water compartment sizes and affect the measured ADC values in heterogeneous water environments such as in PCa. Future studies may evaluate the measurement of ADC or other diffusion metrics using ENCODE in PCa of different grades in a larger cohort of patients.

7.5.2 Improving Through-Slice Spatial Resolution of Prostate DWI

In **chapter 4**, we developed ENCODE-RMT DWI with ~3.5 times higher in-plane resolution of 1.0x1.0 mm^2 compared to standard prostate DWI. However, spatial resolution of DWI measurement is also heavily influenced by the through-slice dimension, and the current protocol has low through-plane resolution of 3.6 mm. This may still lead to inaccurate PCa depiction on DWI due to partial volume averaging effects along slice dimension. To reduce slice thickness, alternative sequence designs and reconstruction methods may be explored in the future, e.g., by including the application of simultaneous multi-slice excitation [156] and combining with through-slice dimension super-resolution reconstruction by exploiting the coil sensitivity variations along the slice dimension [156]. Such a high in-plane and high through-plane resolution prostate DWI sequence may have potential to enable finer depiction of PCa in all three spatial dimensions, but is also expected to suffer more from SNR penalties [14]. The development and evaluation of more advanced denoising algorithms, such as RMT-based methods, to handle this more extreme SNR condition while managing scan time could be another important future research direction.

7.5.3 Developing Alternative Efficient Acquisitions for Diffusion-Relaxation Correlation MRI

In **chapter 5** and **chapter 6**, we implemented the DR-CSI technique using a spin-echo diffusion weighted single-shot echo planar imaging sequence to acquire difference combinations of TE and b-value encodings. The excitation and acquisition of different TE-b encodings using such a sequence were executed in a sequential manner, leading to scan time increase in proportion to the number of acquired TE-b encodings. Besides under-sampling DR-CSI signals by skipping certain TE-b encodings as investigated in **chapter 6**, alternative efficient sequences may be developed, e.g., by acquiring the series of DR-CSI images with increasing TE (e.g. from 60-120 ms) but identical b-values in a single repetition time by inserting multiple 180-degree refocusing pulses to enable acquisition of multiple readouts in one repetition time [157]. Future work may explore the application and scan time benefits of these efficient diffusion-relaxation acquisition sequences. The synergy between alternative efficient acquisition with feature selection analysis such as SBS may be another fruitful direction for future research.

7.5.4 Improving SNR for In Vivo Prostate Diffusion-Relaxation Correlation MRI

In **chapter 3** and **chapter 4**, we demonstrated the advantages of ENCODE waveform design and RMT-based denoising to improve the SNR of *in vivo* prostate diffusion MRI. In **chapter 5** and **chapter 6**, we demonstrated that in the *ex vivo* 3T MRI setting, DR-CSI can help to characterize microscopic features of PCa by disentangling the signal contributions from multiple microscopic tissue compartments. The synergy of ENCODE waveform design, RMT-based denoising and DR-CSI have yet to be investigated, which may benefit *in vivo* prostate microstructure mapping using DR-CSI since the successful reconstruction of T_2-D spectra for resolving sub-voxel tissue compartments relies on sufficient *in vivo* SNR [96,25]. First, ENCODE or CODE waveforms can

unlock a shorter minimal TE for each targeted b-value [28,64], while maintaining the same dynamic ranges for the TE and b-values encodings, therefore enhancing the SNR of all acquired DR-CSI images. Second, as DR-CSI datasets can include many TE and b-value encodings, it can take advantage of RMT-base denoising to suppress thermal noise while minimizing removal of tissue signal information by exploiting the redundancy of noise statistics across multiple dimensions of space and diffusion-relaxation contrast encodings. Future work can investigate the translational benefits of ENCODE and RMT-based denoising to enable robust and faster *in vivo* prostate DR-CSI for non-invasive mapping of prostate cancer microstructure.

REFERENCES

1. Siegel RL, Miller KD, Wagle NS, Jemal A (2023) Cancer statistics, 2023. CA Cancer J Clin 73 (1):17-48.

2. Barrett T, Haider MA (2016) The Emerging Role of MRI in Prostate Cancer Active Surveillance and Ongoing Challenges. American Journal of Roentgenology 208 (1):131-139.

3. Lawrence EM, Gnanapragasam VJ, Priest AN, Sala E (2012) The emerging role of diffusion-weighted MRI in prostate cancer management. Nat Rev Urol 9 (2):94-101.

4. Boesen L, Chabanova E, Løgager V, Balslev I, Thomsen HS (2015) Apparent diffusion coefficient ratio correlates significantly with prostate cancer gleason score at final pathology. J Magn Reson Imaging 42 (2):446-453.

5. Stejskal EO, Tanner JE (2004) Spin Diffusion Measurements: Spin Echoes in the Presence of a Time‐Dependent Field Gradient. The Journal of Chemical Physics 42 (1):288-292.

6. Reese TG, Heid O, Weisskoff RM, Wedeen VJ (2003) Reduction of eddy-current-induced distortion in diffusion MRI using a twice-refocused spin echo. Magn Reson Med 49 (1):177-182.

7. Stocker D, Manoliu A, Becker AS, Barth BK, Nanz D, Klarhöfer M, Donati OF (2018) Image Quality and Geometric Distortion of Modern Diffusion-Weighted Imaging Sequences in Magnetic Resonance Imaging of the Prostate. Invest Radiol 53 (4):200-206.

8. Jambor I (2017) Optimization of prostate MRI acquisition and post-processing protocol: a pictorial review with access to acquisition protocols. Acta Radiol Open 6 (12):2058460117745574.

9. Fütterer JJ (2016) High-Resolution Diffusion-weighted Imaging Increases Prostate Cancer Visibility? EBioMedicine 7:12.

10. Medved M, Soylu-Boy FN, Karademir I, Sethi I, Yousuf A, Karczmar GS, Oto A (2014) High-resolution diffusion-weighted imaging of the prostate. AJR Am J Roentgenol 203 (1):85-90.

11. Nguyen C, Sharif-Afshar AR, Fan Z, Xie Y, Wilson S, Bi X, Payor L, Saouaf R, Kim H, Li D (2016) 3D high-resolution diffusion-weighted MRI at 3T: Preliminary application in prostate cancer patients undergoing active surveillance protocol for low-risk prostate cancer. Magn Reson Med 75 (2):616-626.

12. Sharif-Afshar AR, Nguyen C, Feng TS, Payor L, Fan Z, Saouaf R, Li D, Kim HL (2016) Prospective Pilot Trial to Evaluate a High Resolution Diffusion-Weighted MRI in Prostate Cancer Patients. EBioMedicine 7:80-84.

13. Langer DL, Kwast THvd, Evans AJ, Sun L, Yaffe MJ, Trachtenberg J, Haider MA (2008) Intermixed Normal Tissue within Prostate Cancer: Effect on MR Imaging Measurements of Apparent Diffusion Coefficient and T2—Sparse versus Dense Cancers. Radiology 249 (3):900-908.

14. Wu W, Miller KL (2017) Image formation in diffusion MRI: A review of recent technical developments. J Magn Reson Imaging 46 (3):646-662.

15. Bourne R, Panagiotaki E (2016) Limitations and Prospects for Diffusion-Weighted MRI of the Prostate. Diagnostics (Basel) 6 (2).

16. Henry GH, Malewska A, Joseph DB, Malladi VS, Lee J, Torrealba J, Mauck RJ, Gahan JC, Raj GV, Roehrborn CG (2018) A cellular anatomy of the normal adult human prostate and prostatic urethra. Cell reports 25 (12):3530-3542. e3535.

17. Eble JN SG, Epstein J, Sesterhenn I (2004) Pathology and Genetics of Tumours of the Urinary System and Male Genital Organs. World Health Organization Classification of Tumours Lyon, France: IARC Press.

18. Chamie K, Sonn GA, Finley DS, Tan N, Margolis DJ, Raman SS, Natarajan S, Huang J, Reiter RE (2014) The role of magnetic resonance imaging in delineating clinically significant prostate cancer. Urology 83 (2):369-375.

19. Lemberskiy G, Fieremans E, Veraart J, Deng FM, Rosenkrantz AB, Novikov DS (2018) Characterization of prostate microstructure using water diffusion and NMR relaxation. Front Phys 6.

20. Panagiotaki E, Chan RW, Dikaios N, Ahmed HU, O'Callaghan J, Freeman A, Atkinson D, Punwani S, Hawkes DJ, Alexander DC (2015) Microstructural Characterization of Normal and Malignant Human Prostate Tissue With Vascular, Extracellular, and Restricted Diffusion for Cytometry in Tumours Magnetic Resonance Imaging. Investigative Radiology 50 (4).

21. Sabouri S, Chang SD, Savdie R, Zhang J, Jones EC, Goldenberg SL, Black PC, Kozlowski P (2017) Luminal Water Imaging: A New MR Imaging T2 Mapping Technique for Prostate Cancer Diagnosis. Radiology 284 (2):451-459.

22. Chatterjee A, Bourne RM, Wang S, Devaraj A, Gallan AJ, Antic T, Karczmar GS, Oto A (2018) Diagnosis of Prostate Cancer with Noninvasive Estimation of Prostate Tissue Composition by Using Hybrid Multidimensional MR Imaging: A Feasibility Study. Radiology 287 (3):864-873.

23. Johnston EW, Bonet-Carne E, Ferizi U, Yvernault B, Pye H, Patel D, Clemente J, Piga W, Heavey S, Sidhu HS, Giganti F, O'Callaghan J, Appayya MB, Grey A, Saborowska A, Ourselin S, Hawkes D, Moore CM, Emberton M, Ahmed HU, Whitaker H, Rodriguez-Justo M, Freeman

A, Atkinson D, Alexander D, Panagiotaki E, Punwani S (2019) VERDICT MRI for Prostate Cancer: Intracellular Volume Fraction versus Apparent Diffusion Coefficient. Radiology 291 (2):391-397.

24. Bourne RM, Kurniawan N, Cowin G, Stait-Gardner T, Sved P, Watson G, Price WS (2012) Microscopic diffusivity compartmentation in formalin-fixed prostate tissue. Magnetic resonance in medicine 68 (2):614-620.

25. Slator PJ, Palombo M, Miller KL, Westin C-F, Laun F, Kim D, Haldar JP, Benjamini D, Lemberskiy G, de Almeida Martins JP, Hutter J (2021) Combined diffusion-relaxometry microstructure imaging: Current status and future prospects. Magnetic resonance in medicine 86 (6):2987-3011.

26. Benjamini D, Basser PJ (2020) Multidimensional correlation MRI. NMR in Biomedicine 33 (12):e4226.

27. Kim D, Wisnowski JL, Nguyen CT, Haldar JP (2020) Multidimensional correlation spectroscopic imaging of exponential decays: From theoretical principles to in vivo human applications. NMR in Biomedicine 33 (12):e4244.

28. Aliotta E, Moulin K, Ennis DB (2018) Eddy current-nulled convex optimized diffusion encoding (EN-CODE) for distortion-free diffusion tensor imaging with short echo times. Magn Reson Med 79 (2):663-672.

29. Wilm BJ, Svensson J, Henning A, Pruessmann KP, Boesiger P, Kollias SS (2007) Reduced field-of-view MRI using outer volume suppression for spinal cord diffusion imaging. Magn Reson Med 57 (3):625-630.

30. Gavish M, Donoho DL (2017) Optimal Shrinkage of Singular Values. IEEE Transactions on Information Theory 63 (4):2137-2152.

31. Veraart J, Novikov DS, Christiaens D, Ades-Aron B, Sijbers J, Fieremans E (2016) Denoising of diffusion MRI using random matrix theory. Neuroimage 142:394-406.

32. Kim D, Doyle EK, Wisnowski JL, Kim JH, Haldar JP (2017) Diffusion-relaxation correlation spectroscopic imaging: A multidimensional approach for probing microstructure. Magnetic Resonance in Medicine 78 (6):2236-2249.

33. Siegel RL, Miller KD, Fuchs HE, Jemal A (2022) Cancer statistics, 2022. CA Cancer J Clin 72 (1):7-33.

34. Gillessen S, Attard G, Beer TM, Beltran H, Bjartell A, Bossi A, Briganti A, Bristow RG, Chi KN, Clarke N (2020) Management of patients with advanced prostate cancer: report of the advanced prostate cancer consensus conference 2019. European urology 77 (4):508-547.

35. Catalona WJ (1994) Management of cancer of the prostate. New England Journal of Medicine 331 (15):996-1004.

36. Thompson IM, Ankerst DP (2007) Prostate-specific antigen in the early detection of prostate cancer. Cmaj 176 (13):1853-1858.

37. Ilic D, Djulbegovic M, Jung JH, Hwang EC, Zhou Q, Cleves A, Agoritsas T, Dahm P (2018) Prostate cancer screening with prostate-specific antigen (PSA) test: a systematic review and meta-analysis. Bmj 362:k3519.

38. Etzioni R, Penson DF, Legler JM, Di Tommaso D, Boer R, Gann PH, Feuer EJ (2002) Overdiagnosis due to prostate-specific antigen screening: lessons from US prostate cancer incidence trends. Journal of the National Cancer Institute 94 (13):981-990.

39. Purysko AS, Baroni RH, Giganti F, Costa D, Renard-Penna R, Kim CK, Raman SS (2021) PI-RADS Version 2.1: A Critical Review, From the AJR Special Series on Radiology Reporting and Data Systems. AJR Am J Roentgenol 216 (1):20-32.

40. Johnson DC, Raman SS, Mirak SA, Kwan L, Bajgiran AM, Hsu W, Maehara CK, Ahuja P, Faiena I, Pooli A, Salmasi A, Sisk A, Felker ER, Lu DSK, Reiter RE (2019) Detection of Individual Prostate Cancer Foci via Multiparametric Magnetic Resonance Imaging. European Urology 75 (5):712-720.

41. Schoots IG, Padhani AR (2020) Delivering Clinical impacts of the MRI diagnostic pathway in prostate cancer diagnosis. Abdominal Radiology 45 (12):4012-4022.

42. Marks L, Young S, Natarajan S (2013) MRI–ultrasound fusion for guidance of targeted prostate biopsy. Current opinion in urology 23 (1):43.

43. Sathianathen NJ, Omer A, Harriss E, Davies L, Kasivisvanathan V, Punwani S, Moore CM, Kastner C, Barrett T, Van Den Bergh RC (2020) Negative predictive value of multiparametric magnetic resonance imaging in the detection of clinically significant prostate cancer in the prostate imaging reporting and data system era: a systematic review and meta-analysis. European Urology 78 (3):402-414.

44. Eldred-Evans D, Tam H, Sokhi H, Padhani AR, Winkler M, Ahmed HU (2020) Rethinking prostate cancer screening: could MRI be an alternative screening test? Nature Reviews Urology 17 (9):526-539.

45. Lee CH, Vellayappan B, Tan CH (2022) Comparison of diagnostic performance and inter-reader agreement between PI-RADS v2. 1 and PI-RADS v2: systematic review and meta-analysis. The British Journal of Radiology 95 (1131):20210509.

46. Le JD, Tan N, Shkolyar E, Lu DY, Kwan L, Marks LS, Huang J, Margolis DJA, Raman SS, Reiter RE (2015) Multifocality and Prostate Cancer Detection by Multiparametric Magnetic Resonance Imaging: Correlation with Whole-mount Histopathology. European Urology 67 (3):569-576.

47. Mazaheri Y, Vargas HA, Nyman G, Akin O, Hricak H (2013) Image artifacts on prostate diffusion-weighted magnetic resonance imaging: trade-offs at 1.5 Tesla and 3.0 Tesla. Acad Radiol 20 (8):1041-1047.

48. Orlhac F, Lecler A, Savatovski J, Goya-Outi J, Nioche C, Charbonneau F, Ayache N, Frouin F, Duron L, Buvat I (2021) How can we combat multicenter variability in MR radiomics? Validation of a correction procedure. European radiology 31:2272-2280.

49. Nketiah G, Selnæs KM, Sandsmark E, Teruel JR, Krüger‐Stokke B, Bertilsson H, Bathen TF, Elschot M (2018) Geometric distortion correction in prostate diffusion‐weighted MRI and its effect on quantitative apparent diffusion coefficient analysis. Magnetic Resonance in Medicine 79 (5):2524-2532.

50. Descotes JL (2019) Diagnosis of prostate cancer. Asian J Urol 6 (2):129-136.

51. Wright JL, Salinas CA, Lin DW, Kolb S, Koopmeiners J, Feng Z, Stanford JL (2009) Prostate cancer specific mortality and Gleason 7 disease differences in prostate cancer outcomes between cases with Gleason 4 + 3 and Gleason 3 + 4 tumors in a population based cohort. J Urol 182 (6):2702-2707.

52. Koch M, Norris DG (2000) An assessment of eddy current sensitivity and correction in single-shot diffusion-weighted imaging. Phys Med Biol 45 (12):3821-3832.

53. Bernstein MA, King KF, Zhou XJ (2004) Handbook of MRI pulse sequences. Elsevier,

54. Kyriazi S, Blackledge M, Collins DJ, Desouza NM (2010) Optimising diffusion-weighted imaging in the abdomen and pelvis: comparison of image quality between monopolar and bipolar single-shot spin-echo echo-planar sequences. Eur Radiol 20 (10):2422-2431.

55. Lee G, Oto A, Giurcanu M (2022) Prostate MRI: Is Endorectal Coil Necessary?-A Review. Life (Basel) 12 (4).

56. Giganti F, Kirkham A, Kasivisvanathan V, Papoutsaki M-V, Punwani S, Emberton M, Moore CM, Allen C (2021) Understanding PI-QUAL for prostate MRI quality: a practical primer for radiologists. Insights into Imaging 12 (1):1-19.

57. Plodeck V, Radosa CG, Hübner HM, Baldus C, Borkowetz A, Thomas C, Kühn JP, Laniado M, Hoffmann RT, Platzek I (2020) Rectal gas-induced susceptibility artefacts on prostate diffusion-weighted MRI with epi read-out at 3.0 T: does a preparatory micro-enema improve image quality? Abdom Radiol (NY) 45 (12):4244-4251.

58. Holdsworth SJ, Skare S, Newbould RD, Guzmann R, Blevins NH, Bammer R (2008) Readout-segmented EPI for rapid high resolution diffusion imaging at 3 T. Eur J Radiol 65 (1):36-46.

59. Attenberger UI, Rathmann N, Sertdemir M, Riffel P, Weidner A, Kannengiesser S, Morelli JN, Schoenberg SO, Hausmann D (2016) Small Field-of-view single-shot EPI-DWI of the prostate: Evaluation of spatially-tailored two-dimensional radiofrequency excitation pulses. Z Med Phys 26 (2):168-176.

60. Reischauer C, Wilm BJ, Froehlich JM, Gutzeit A, Prikler L, Gablinger R, Boesiger P, Wentz KU (2011) High-resolution diffusion tensor imaging of prostate cancer using a reduced FOV technique. Eur J Radiol 80 (2):e34-41.

61. Usman M, Kakkar L, Matakos A, Kirkham A, Arridge S, Atkinson D (2020) Joint B0 and image estimation integrated with model based reconstruction for field map update and distortion correction in prostate diffusion MRI. Magnetic resonance imaging 65:90-99.

62. Breuer FA, Kannengiesser SA, Blaimer M, Seiberlich N, Jakob PM, Griswold MA (2009) General formulation for quantitative G-factor calculation in GRAPPA reconstructions. Magn Reson Med 62 (3):739-746.

63. Ullrich T, Kohli MD, Ohliger MA, Magudia K, Arora SS, Barrett T, Bittencourt LK, Margolis DJ, Schimmöller L, Turkbey B, Westphalen AC (2020) Quality Comparison of 3 Tesla multiparametric MRI of the prostate using a flexible surface receiver coil versus conventional surface coil plus endorectal coil setup. Abdom Radiol (NY) 45 (12):4260-4270.
64. Aliotta E, Wu HH, Ennis DB (2017) Convex optimized diffusion encoding (CODE) gradient waveforms for minimum echo time and bulk motion-compensated diffusion-weighted MRI. Magn Reson Med 77 (2):717-729.
65. Walsh DO, Gmitro AF, Marcellin MW (2000) Adaptive reconstruction of phased array MR imagery. Magn Reson Med 43 (5):682-690.
66. Marčenko VA PL (1967) Distribution of eigenvalues for some sets of random matrices. Mathematics of the USSR-Sbornik.
67. Zelhof B, Pickles M, Liney G, Gibbs P, Rodrigues G, Kraus S, Turnbull L (2009) Correlation of diffusion-weighted magnetic resonance data with cellularity in prostate cancer. BJU Int 103 (7):883-888.
68. Goh V (2023) Tumor Physiology and Clinically Significant Prostate Cancer Detection. Radiology 306 (1):200-201.
69. Lemberskiy G, Rosenkrantz AB, Veraart J, Taneja SS, Novikov DS, Fieremans E (2017) Time-Dependent Diffusion in Prostate Cancer. Investigative Radiology 52 (7):405-411.
70. Chatterjee A, Watson G, Myint E, Sved P, McEntee M, Bourne R (2015) Changes in Epithelium, Stroma, and Lumen Space Correlate More Strongly with Gleason Pattern and Are Stronger Predictors of Prostate ADC Changes than Cellularity Metrics. Radiology 277 (3):751-762.

71. Palombo M, Valindria V, Singh S, Chiou E, Giganti F, Pye H, Whitaker HC, Atkinson D, Punwani S, Alexander DC (2023) Joint estimation of relaxation and diffusion tissue parameters for prostate cancer with relaxation-VERDICT MRI. Sci Rep 13 (1):2999.
72. Kjaer L, Thomsen C, Iversen P, Henriksen O (1987) In vivo estimation of relaxation processes in benign hyperplasia and carcinoma of the prostate gland by magnetic resonance imaging. Magn Reson Imaging 5 (1):23-30.
73. Storås TH, Gjesdal KI, Gadmar ØB, Geitung JT, Kløw NE (2008) Prostate magnetic resonance imaging: multiexponential T2 decay in prostate tissue. Journal of Magnetic Resonance Imaging: An Official Journal of the International Society for Magnetic Resonance in Medicine 28 (5):1166-1172.
74. Lee JH, Labadie C, Springer Jr CS, Harbison GS (1993) Two-dimensional inverse Laplace transform NMR: altered relaxation times allow detection of exchange correlation. Journal of the American Chemical Society 115 (17):7761-7764.
75. Galvosas P, Callaghan PT (2010) Multi-dimensional inverse Laplace spectroscopy in the NMR of porous media. Comptes Rendus Physique 11 (2):172-180.
76. Kuhlman KL (2013) Review of inverse Laplace transform algorithms for Laplace-space numerical approaches. Numerical Algorithms 63:339-355.
77. Celik H, Bouhrara M, Reiter DA, Fishbein KW, Spencer RG (2013) Stabilization of the inverse Laplace transform of multiexponential decay through introduction of a second dimension. J Magn Reson 236:134-139.
78. Tavakoli AA, Hielscher T, Badura P, Görtz M, Kuder TA, Gnirs R, Schwab C, Hohenfellner M, Schlemmer H-P, Bonekamp D (2023) Contribution of Dynamic Contrast-enhanced and

Diffusion MRI to PI-RADS for Detecting Clinically Significant Prostate Cancer. Radiology 306 (1):186-199.

79. Bodammer N, Kaufmann J, Kanowski M, Tempelmann C (2004) Eddy current correction in diffusion-weighted imaging using pairs of images acquired with opposite diffusion gradient polarity. Magn Reson Med 51 (1):188-193.

80. Lewis S, Kamath A, Chatterji M, Patel A, Shyknevsky I, Dyvorne HA, Kuehn B, Taouli B (2015) Diffusion-weighted imaging of the liver in patients with chronic liver disease: comparison of monopolar and bipolar diffusion gradients for image quality and lesion detection. AJR Am J Roentgenol 204 (1):59-68.

81. deSouza NM, Winfield JM, Waterton JC, Weller A, Papoutsaki MV, Doran SJ, Collins DJ, Fournier L, Sullivan D, Chenevert T, Jackson A, Boss M, Trattnig S, Liu Y (2018) Implementing diffusion-weighted MRI for body imaging in prospective multicentre trials: current considerations and future perspectives. Eur Radiol 28 (3):1118-1131.

82. Chilla GS, Tan CH, Xu C, Poh CL (2015) Diffusion weighted magnetic resonance imaging and its recent trend-a survey. Quant Imaging Med Surg 5 (3):407-422.

83. Isebaert S, Van den Bergh L, Haustermans K, Joniau S, Lerut E, De Wever L, De Keyzer F, Budiharto T, Slagmolen P, Van Poppel H, Oyen R (2013) Multiparametric MRI for prostate cancer localization in correlation to whole-mount histopathology. J Magn Reson Imaging 37 (6):1392-1401.

84. Tan N, Lin WC, Khoshnoodi P, Asvadi NH, Yoshida J, Margolis DJ, Lu DS, Wu H, Sung KH, Lu DY, Huang J, Raman SS (2017) In-Bore 3-T MR-guided Transrectal Targeted Prostate Biopsy: Prostate Imaging Reporting and Data System Version 2-based Diagnostic Performance for Detection of Prostate Cancer. Radiology 283 (1):130-139.

85. Storey P, Frigo FJ, Hinks RS, Mock BJ, Collick BD, Baker N, Marmurek J, Graham SJ (2007) Partial k-space reconstruction in single-shot diffusion-weighted echo-planar imaging. Magn Reson Med 57 (3):614-619.

86. Dregely I, Margolis DA, Sung K, Zhou Z, Rangwala N, Raman SS, Wu HH (2016) Rapid quantitative T(2) mapping of the prostate using three-dimensional dual echo steady state MRI at 3T. Magn Reson Med 76 (6):1720-1729.

87. Keenan KE, Ainslie M, Barker AJ, Boss MA, Cecil KM, Charles C, Chenevert TL, Clarke L, Evelhoch JL, Finn P (2018) Quantitative magnetic resonance imaging phantoms: a review and the need for a system phantom. Magnetic resonance in medicine 79 (1):48-61.

88. Wu HH, Priester A, Khoshnoodi P, Zhang Z, Shakeri S, Afshari Mirak S, Asvadi NH, Ahuja P, Sung K, Natarajan S, Sisk A, Reiter R, Raman S, Enzmann D (2019) A system using patient-specific 3D-printed molds to spatially align in vivo MRI with ex vivo MRI and whole-mount histopathology for prostate cancer research. Journal of Magnetic Resonance Imaging 49 (1):270-279.

89. Hallgren KA (2012) Computing Inter-Rater Reliability for Observational Data: An Overview and Tutorial. Tutor Quant Methods Psychol 8 (1):23-34.

90. Weinreb JC, Barentsz JO, Choyke PL, Cornud F, Haider MA, Macura KJ, Margolis D, Schnall MD, Shtern F, Tempany CM (2016) PI-RADS prostate imaging–reporting and data system: 2015, version 2. European urology 69 (1):16-40.

91. Tan N, Margolis DJ, Lu DY, King KG, Huang J, Reiter RE, Raman SS (2015) Characteristics of Detected and Missed Prostate Cancer Foci on 3-T Multiparametric MRI Using an Endorectal Coil Correlated With Whole-Mount Thin-Section Histopathology. AJR Am J Roentgenol 205 (1):W87-92.

92. Rosenkrantz AB, Chandarana H, Pfeuffer J, Triolo MJ, Shaikh MB, Mossa DJ, Geppert C (2015) Zoomed echo-planar imaging using parallel transmission: impact on image quality of diffusion-weighted imaging of the prostate at 3T. Abdom Imaging 40 (1):120-126.

93. Ben-Amitay S, Jones DK, Assaf Y (2012) Motion correction and registration of high b-value diffusion weighted images. Magn Reson Med 67 (6):1694-1702.

94. Woodfield CA, Tung GA, Grand DJ, Pezzullo JA, Machan JT, Renzulli JF, 2nd (2010) Diffusion-weighted MRI of peripheral zone prostate cancer: comparison of tumor apparent diffusion coefficient with Gleason score and percentage of tumor on core biopsy. AJR Am J Roentgenol 194 (4):W316-322.

95. Zhang Z, Magyar C, Priester A, Shakeri S, Mirak SA, Bajgiran AM, Sisk AE, Sung K, Reiter RE, Enzmann DR Characterization of prostate microstructure using diffusion-relaxation correlation spectrum imaging and comparison to digital histopathology. In: Proc 27th Annual Meeting ISMRM, Montreal, 2019.

96. Zhang Z, Wu HH, Priester A, Magyar C, Afshari Mirak S, Shakeri S, Mohammadian Bajgiran A, Hosseiny M, Azadikhah A, Sung K, Reiter RE, Sisk AE, Raman S, Enzmann DR (2020) Prostate Microstructure in Prostate Cancer Using 3-T MRI with Diffusion-Relaxation Correlation Spectrum Imaging: Validation with Whole-Mount Digital Histopathology. Radiology 296 (2):348-355.

97. Zhang Z, Moulin K, Aliotta E, Shakeri S, Afshari Mirak S, Hosseiny M, Raman S, Ennis DB, Wu HH (2020) Prostate diffusion MRI with minimal echo time using eddy current nulled convex optimized diffusion encoding. J Magn Reson Imaging 51 (5):1526-1539.

98. Gregory Lemberskiy YM, Herbert Alberto Vargas, Ricardo Otazo, Els Fieremans, and Dmitry S Novikov (2020) Reducing scan time of routine prostate diffusion-weighted imaging using random matrix theory reconstruction. Processings of the 28th Annual Meeting of ISMRM.
99. Lemberskiy G BS, Veraart J, Shepherd TM, Fieremans E, Novikov DS (2019) Achieving sub-mm clinical diffusion MRI resolution by removing noise during reconstruction using random matrix theory. Processings of the 27th Annual Meeting of ISMRM.
100. Cordero-Grande L, Christiaens D, Hutter J, Price AN, Hajnal JV (2019) Complex diffusion-weighted image estimation via matrix recovery under general noise models. NeuroImage 200:391-404.
101. Moeller S, Pisharady PK, Ramanna S, Lenglet C, Wu X, Dowdle L, Yacoub E, Uğurbil K, Akçakaya M (2021) NOise reduction with DIstribution Corrected (NORDIC) PCA in dMRI with complex-valued parameter-free locally low-rank processing. NeuroImage 226:117539.
102. Gudbjartsson H, Patz S (1995) The Rician distribution of noisy MRI data. Magn Reson Med 34 (6):910-914.
103. Pruessmann KP, Weiger M, Börnert P, Boesiger P (2001) Advances in sensitivity encoding with arbitrary k-space trajectories. Magn Reson Med 46 (4):638-651.
104. Dietrich O, Raya JG, Reeder SB, Ingrisch M, Reiser MF, Schoenberg SO (2008) Influence of multichannel combination, parallel imaging and other reconstruction techniques on MRI noise characteristics. Magn Reson Imaging 26 (6):754-762.
105. Hutter J, Christiaens DJ, Schneider T, Cordero-Grande L, Slator PJ, Deprez M, Price AN, Tournier JD, Rutherford M, Hajnal JV (2018) Slice-level diffusion encoding for motion and distortion correction. Med Image Anal 48:214-229.

106. Powell E, Schneider T, Battiston M, Grussu F, Toosy A, Clayden JD, Wheeler-Kingshott C (2022) SENSE EPI reconstruction with 2D phase error correction and channel-wise noise removal. Magn Reson Med 88 (5):2157-2166.
107. Xu Y, Haacke EM (2001) Partial Fourier imaging in multi-dimensions: a means to save a full factor of two in time. J Magn Reson Imaging 14 (5):628-635.
108. Haldar JP, Liu Y, Liao C, Fan Q, Setsompop K (2020) Fast submillimeter diffusion MRI using gSlider-SMS and SNR-enhancing joint reconstruction. Magn Reson Med 84 (2):762-776.
109. Baltzer P, Mann RM, Iima M, Sigmund EE, Clauser P, Gilbert FJ, Martincich L, Partridge SC, Patterson A, Pinker K, Thibault F, Camps-Herrero J, Le Bihan D (2020) Diffusion-weighted imaging of the breast-a consensus and mission statement from the EUSOBI International Breast Diffusion-Weighted Imaging working group. Eur Radiol 30 (3):1436-1450.
110. Zhang Q, Coolen BF, Versluis MJ, Strijkers GJ, Nederveen AJ (2017) Diffusion-prepared stimulated-echo turbo spin echo (DPsti-TSE): An eddy current-insensitive sequence for three-dimensional high-resolution and undistorted diffusion-weighted imaging. NMR Biomed 30 (7).
111. Irfanoglu MO, Sarlls J, Nayak A, Pierpaoli C (2019) Evaluating corrections for Eddy-currents and other EPI distortions in diffusion MRI: methodology and a dataset for benchmarking. Magn Reson Med 81 (4):2774-2787.
112. Ades-Aron B, Veraart J, Kochunov P, McGuire S, Sherman P, Kellner E, Novikov DS, Fieremans E (2018) Evaluation of the accuracy and precision of the diffusion parameter EStImation with Gibbs and NoisE removal pipeline. NeuroImage 183:532-543.
113. Ramos-Llordén G, Vegas-Sánchez-Ferrero G, Liao C, Westin CF, Setsompop K, Rathi Y (2021) SNR-enhanced diffusion MRI with structure-preserving low-rank denoising in reproducing kernel Hilbert spaces. Magn Reson Med 86 (3):1614-1632.

114. Bourne R, Liang S, Panagiotaki E, Bongers A, Sved P, Watson G (2017) Measurement and modeling of diffusion time dependence of apparent diffusion coefficient and fractional anisotropy in prostate tissue ex vivo. NMR Biomed 30 (10).

115. Kaye EA, Aherne EA, Duzgol C, Häggström I, Kobler E, Mazaheri Y, Fung MM, Zhang Z, Otazo R, Vargas HA, Akin O (2020) Accelerating Prostate Diffusion-weighted MRI Using a Guided Denoising Convolutional Neural Network: Retrospective Feasibility Study. Radiology: Artificial Intelligence 2 (5):e200007.

116. Benjamini D, Basser PJ (2017) Magnetic resonance microdynamic imaging reveals distinct tissue microenvironments. NeuroImage 163:183-196.

117. Wagstaff DA, Elek E, Kulis S, Marsiglia F (2009) Using a nonparametric bootstrap to obtain a confidence interval for Pearson'sr with cluster randomized data: a case study. The journal of primary prevention 30:497-512.

118. Kobus T, van der Laak JA, Maas MC, Hambrock T, Bruggink CC, Hulsbergen-van de Kaa CA, Scheenen TW, Heerschap A (2016) Contribution of histopathologic tissue composition to quantitative MR spectroscopy and diffusion-weighted imaging of the prostate. Radiology 278 (3):801-811.

119. Kitzing YX, Prando A, Varol C, Karczmar GS, Maclean F, Oto A (2016) Benign conditions that mimic prostate carcinoma: MR imaging features with histopathologic correlation. Radiographics 36 (1):162-175.

120. Langer DL, van der Kwast TH, Evans AJ, Plotkin A, Trachtenberg J, Wilson BC, Haider MA (2010) Prostate tissue composition and MR measurements: investigating the relationships between ADC, T2, K trans, ve, and corresponding histologic features. Radiology 255 (2):485-494.

121. Hectors SJ, Semaan S, Song C, Lewis S, Haines GK, Tewari A, Rastinehad AR, Taouli B (2018) Advanced Diffusion-weighted Imaging Modeling for Prostate Cancer Characterization: Correlation with Quantitative Histopathologic Tumor Tissue Composition-A Hypothesis-generating Study. Radiology 286 (3):918-928.

122. Uribe CF, Jones EC, Chang SD, Goldenberg SL, Reinsberg SA, Kozlowski P (2015) In vivo 3 T and ex vivo 7 T diffusion tensor imaging of prostate cancer: Correlation with histology. Magnetic resonance imaging 33 (5):577-583.

123. Delannoy J, Chen CN, Turner R, Levin R, Le Bihan D (1991) Noninvasive temperature imaging using diffusion MRI. Magnetic resonance in medicine 19 (2):333-339.

124. Sabouri S, Fazli L, Chang SD, Savdie R, Jones EC, Goldenberg SL, Black PC, Kozlowski P (2017) MR measurement of luminal water in prostate gland: Quantitative correlation between MRI and histology. Journal of Magnetic Resonance Imaging 46 (3):861-869.

125. Alexander DC (2008) A general framework for experiment design in diffusion MRI and its application in measuring direct tissue-microstructure features. Magnetic Resonance in Medicine 60 (2):439-448.

126. Lemke A, Stieltjes B, Schad LR, Laun FB (2011) Toward an optimal distribution of b values for intravoxel incoherent motion imaging. Magnetic Resonance Imaging 29 (6):766-776.

127. Pineda AR, Reeder SB, Wen Z, Pelc NJ (2005) Cramér–Rao bounds for three-point decomposition of water and fat. Magnetic Resonance in Medicine 54 (3):625-635.

128. Jones JA, Hodgkinson P, Barker AL, Hore PJ (1996) Optimal Sampling Strategies for the Measurement of Spin–Spin Relaxation Times. Journal of Magnetic Resonance, Series B 113 (1):25-34.

129. Zibetti MVW, Sharafi A, Regatte RR (2022) Optimization of spin-lock times in T1ρ mapping of knee cartilage: Cramér-Rao bounds versus matched sampling-fitting. Magnetic Resonance in Medicine 87 (3):1418-1434.

130. Woods JG, Chappell MA, Okell TW (2019) A general framework for optimizing arterial spin labeling MRI experiments. Magnetic Resonance in Medicine 81 (4):2474-2488.

131. Song Y-Q, Xiao L (2020) Optimization of multidimensional MR data acquisition for relaxation and diffusion. NMR in Biomedicine 33 (12):e4238.

132. Bo Z, Haldar JP, Congyu L, Dan M, Yun J, Griswold MA, Setsompop K, Wald LL (2019) Optimal Experiment Design for Magnetic Resonance Fingerprinting: Cramér-Rao Bound Meets Spin Dynamics. IEEE Trans Med Imaging 38 (3):844-861.

133. Bai R, Cloninger A, Czaja W, Basser PJ (2015) Efficient 2D MRI relaxometry using compressed sensing. Journal of Magnetic Resonance 255:88-99.

134. Benjamini D, Basser PJ (2018) Towards clinically feasible relaxation-diffusion correlation MRI using MADCO. Microporous Mesoporous Mater 269:93-96.

135. JP KDaH (2017) Faster diffusion-relaxation correlation spectroscopic imaging (DR-CSI) using optimized experiment design. Proc Int Soc Magn Reson Med, pp 176, 2017.

136. Zhang Y, Wells SA, Hernando D (2019) Stimulated echo based mapping (STEM) of T1, T2, and apparent diffusion coefficient: validation and protocol optimization. Magnetic Resonance in Medicine 81 (1):167-181.

137. Kim D, Wisnowski JL, Haldar JP Improved efficiency for microstructure imaging using high-dimensional MR correlation spectroscopic imaging. In: 2017 51st Asilomar Conference on Signals, Systems, and Computers, 29 Oct.-1 Nov. 2017 2017. pp 1264-1268.

138. Lampinen B, Szczepankiewicz F, Mårtensson J, van Westen D, Hansson O, Westin C-F, Nilsson M (2020) Towards unconstrained compartment modeling in white matter using diffusion-relaxation MRI with tensor-valued diffusion encoding. Magnetic Resonance in Medicine 84 (3):1605-1623.

139. Grussu F, Blumberg SB, Battiston M, Kakkar LS, Lin H, Ianuş A, Schneider T, Singh S, Bourne R, Punwani S, Atkinson D, Gandini Wheeler-Kingshott CAM, Panagiotaki E, Mertzanidou T, Alexander DC (2021) Feasibility of Data-Driven, Model-Free Quantitative MRI Protocol Design: Application to Brain and Prostate Diffusion-Relaxation Imaging. Frontiers in Physics 9.

140. Liu Y (2014) Mean Square Error of Survey Estimates. In: Michalos AC (ed) Encyclopedia of Quality of Life and Well-Being Research, doi:10.1007/978-94-007-0753-5_1754. Springer Netherlands, Dordrecht, pp 3892-3893.

141. Eldar YC (2006) Uniformly improving the Cramér-Rao bound and maximum-likelihood estimation. IEEE Transactions on Signal Processing 54 (8):2943-2956.

142. Haldar JP, Kim D (2019) OEDIPUS: An Experiment Design Framework for Sparsity-Constrained MRI. IEEE Trans Med Imaging 38 (7):1545-1558.

143. Reeves SJ, Zhao Z (1999) Sequential algorithms for observation selection. IEEE Transactions on Signal Processing 47 (1):123-132.

144. Priester A, Wu H, Khoshnoodi P, Schneider D, Zhang Z, Asvadi NH, Sisk A, Raman S, Reiter R, Grundfest W, Marks LS, Natarajan S (2019) Registration Accuracy of Patient-Specific, Three-Dimensional-Printed Prostate Molds for Correlating Pathology With Magnetic Resonance Imaging. IEEE Trans Biomed Eng 66 (1):14-22.

145. Burer S, Letchford AN (2012) Non-convex mixed-integer nonlinear programming: A survey. Surveys in Operations Research and Management Science 17:97-106.

146. Agrawal T (2021) Hyperparameter optimization in machine learning: make your machine learning and deep learning models more efficient. Springer,

147. Priester A, Natarajan S, Khoshnoodi P, Margolis DJ, Raman SS, Reiter RE, Huang J, Grundfest W, Marks LS (2017) Magnetic Resonance Imaging Underestimation of Prostate Cancer Geometry: Use of Patient Specific Molds to Correlate Images with Whole Mount Pathology. J Urol 197 (2):320-326.

148. Aslim EJ, Law YXT, Fook-Chong SMC, Ho HSS, Yuen JSP, Lau WKO, Lee LS, Cheng CWS, Ngo NT, Law YM, Tay KJ (2021) Defining prostate cancer size and treatment margin for focal therapy: does intralesional heterogeneity impact the performance of multiparametric MRI? BJU Int 128 (2):178-186.

149. Messina E, Pecoraro M, Laschena L, Bicchetti M, Proietti F, Ciardi A, Leonardo C, Sciarra A, Girometti R, Catalano C, Panebianco V (2023) Low cancer yield in PI-RADS 3 upgraded to 4 by dynamic contrast-enhanced MRI: is it time to reconsider scoring categorization? European Radiology doi:10.1007/s00330-023-09605-0.

150. Abdul Raheem R, Razzaq A, Beraud V, Menzies-Wilson R, Odeh R, Ibiok I, Mulawkar P, Andrews H, Anjum I, Hosny K, Leslie T (2023) Can a prostate biopsy be safely deferred on PI-RADS 1,2 or 3 lesions seen on pre-biopsy mp-MRI? Arab J Urol 21 (1):10-17.

151. Rosenkrantz AB, Ginocchio LA, Cornfeld D, Froemming AT, Gupta RT, Turkbey B, Westphalen AC, Babb JS, Margolis DJ (2016) Interobserver reproducibility of the PI-RADS version 2 lexicon: a multicenter study of six experienced prostate radiologists. Radiology 280 (3):793-804.

152. Park KJ, Choi SH, Lee JS, Kim JK, Kim MH, Jeong IG (2020) Risk Stratification of Prostate Cancer According to PI-RADS® Version 2 Categories: Meta-Analysis for Prospective Studies. J Urol 204 (6):1141-1149.

153. Humphrey PA (2017) Histopathology of Prostate Cancer. Cold Spring Harb Perspect Med 7 (10).

154. Lawson P, Sholl AB, Brown JQ, Fasy BT, Wenk C (2019) Persistent homology for the quantitative evaluation of architectural features in prostate cancer histology. Sci Rep 9 (1):1139.

155. Reynaud O (2017) Time-dependent diffusion MRI in cancer: tissue modeling and applications. Frontiers in Physics 5:58.

156. Setsompop K, Fan Q, Stockmann J, Bilgic B, Huang S, Cauley SF, Nummenmaa A, Wang F, Rathi Y, Witzel T (2018) High-resolution in vivo diffusion imaging of the human brain with generalized slice dithered enhanced resolution: Simultaneous multislice (g S lider-SMS). Magnetic resonance in medicine 79 (1):141-151.

157. Ji Y, Hoge WS, Gagoski B, Westin CF, Rathi Y, Ning L (2022) Accelerating joint relaxation-diffusion MRI by integrating time division multiplexing and simultaneous multi-slice (TDM-SMS) strategies. Magnetic Resonance in Medicine 87 (6):2697-2709.